

# Advanced technologies for spatio-temporal control of neural circuits using optogenetics

A thesis presented in fulfillment of the requirements  
for the degree of

Doctor of Philosophy

by

Filippo Pisano

Department of Physics  
University of Strathclyde

2016

This thesis is the result of the author's original research. It has been composed by the author and has not been previously submitted for examination which has led to the award of a degree. The copyright of this thesis belongs to the author under the terms of the United Kingdom Copyright Acts as qualified by University of Strathclyde Regulation 3.50. Due acknowledgement must always be made of the use of any material contained in, or derived from, this thesis.

Signed:

Date:

## Abstract

The progress of neuroscientific research is linked to the development of technologies able to interface with the complexity of neural circuitry. Remarkable advances in this direction have been achieved in the past decades and it is now possible to optically control the neural activity of genetically targeted cells with techniques known as optogenetic stimulation. The combination of optogenetic stimulation methods with electrophysiological recordings and advanced optical imaging is leading to promising approaches aiming at obtaining information on spiking activity, morphology and genetic identity of the many constituents of neural networks. This PhD research project focussed on the development of an experimental tool to exploit this possibility combining micro-electrode array (MEA) electrophysiological recordings with a custom two-photon microscope and optogenetic stimulation system based on a  $\mu$ LED array. This thesis reports on the construction, validation and application of this tool, that was employed in retinal recordings to link the precisely-timed spike signals detected by the MEA with the anatomical and genetic identity of the spiking neurons. The combination of large-scale MEA recordings with spatio-temporal  $\mu$ LED optogenetic stimulation led to a novel method to link anatomy to functional and genetic identity in genetically-targeted retinal ganglion cells (RGCs) with a large scale approach. This method is a versatile approach that can be applied to characterise the many molecular types of RGCs. The integration of two-photon imaging and MEA recordings proved to be more arduous, yet applicable. Retinal ganglion cells were imaged in two-photon mode while mounted on the MEA and electrophysiological identification of spiking units was demonstrated notwithstanding large laser-induced artifacts. Optimisation of the system will allow to fully exploit the advantages offered by non-linear excitation.

# Contents

List of Acronyms . . . . .	vii
<b>Introduction</b>	<b>1</b>
<b>1 Background</b>	<b>3</b>
1.1 A brief introduction on neurons . . . . .	3
1.1.1 Membrane potentials and neural signals . . . . .	4
1.2 Electrophysiological recordings . . . . .	6
1.2.1 Micro-Electrode Arrays . . . . .	7
1.3 Neural structure of the vertebrate retina . . . . .	8
1.3.1 Anatomy of the vertebrate eye . . . . .	9
1.3.2 Anatomy of the vertebrate retina . . . . .	9
1.3.3 Retinal cell types . . . . .	12
1.4 Optogenetics . . . . .	16
1.4.1 Microbial opsin proteins and channelrhodopsin . . . . .	17
1.4.2 Genetic expression . . . . .	18
1.4.3 Light delivery for optogenetic stimulation . . . . .	19
1.5 Two-photon microscopy . . . . .	20
1.5.1 Foundations . . . . .	21
1.5.2 Two-photon microscopy: practical implementation . . . . .	24
1.5.3 Two-photon microscopy in neuroscience . . . . .	27
<b>2 A setup for two-photon microscopy, optogenetics and MEA recordings</b>	<b>31</b>
2.1 Overview of the system . . . . .	31
2.2 Optogenetic stimulation system based on a $\mu$ LED array . . . . .	31
2.2.1 Projection system . . . . .	32
2.2.2 Power modulation and pattern control . . . . .	34
2.3 Two-photon microscope . . . . .	35
2.3.1 Microscope architecture . . . . .	35

2.3.2	Software control and image acquisition . . . . .	43
2.4	Characterisation of the two-photon microscope . . . . .	46
2.4.1	Excitation of fluorescence . . . . .	46
2.4.2	Optical resolution . . . . .	46
2.4.2.1	×20, 0.5 NA objective . . . . .	47
2.4.2.2	×100, 1.3 NA oil-immersion objective . . . . .	48
2.4.3	Validation of imaging protocols . . . . .	51
2.5	Imaging . . . . .	53
2.6	Discussion and conclusions . . . . .	56
<b>3</b>	<b>Combining two-photon excitation and MEA recordings</b>	<b>59</b>
3.1	Laser scanning interaction with MEA . . . . .	59
3.1.1	MEA composition . . . . .	59
3.1.2	Optical resolution through MEA . . . . .	61
3.1.3	Laser interaction with ITO . . . . .	64
3.1.4	Laser interaction with platinum black and defects in the passivation layer . . . . .	66
3.1.5	Power requirements for two photon excitation . . . . .	67
3.2	MEA recordings of RGC . . . . .	67
3.2.1	Electrophysiological recordings system . . . . .	68
3.2.2	Retinal preparations . . . . .	69
3.2.3	Electrophysiological identification of neurons . . . . .	69
3.2.4	Artifacts from laser scanning and neuron finding . . . . .	70
3.3	MEA recordings, imaging and optogenetics . . . . .	74
3.3.1	PV-Cre mouse . . . . .	74
3.3.2	Two-photon Imaging through the MEA . . . . .	76
3.3.3	Two-Photon optogenetics with MEA recordings . . . . .	77
3.4	Discussion and conclusions . . . . .	82
3.4.1	Laser interaction with the MEA . . . . .	82
3.4.2	Electrophysiology and laser-induced artifacts . . . . .	83
3.4.3	Two-photon optogenetic experiments . . . . .	83
<b>4</b>	<b>Matching of anatomy and function</b>	<b>85</b>
4.1	Introduction . . . . .	85
4.2	Materials and methods . . . . .	86
4.2.1	Animals . . . . .	86
4.2.2	Retinal preparations . . . . .	87
4.2.3	Electrophysiological recordings . . . . .	87
4.2.4	Imaging . . . . .	87

4.3	Visual stimulation . . . . .	88
4.3.1	Visual receptive fields characterisation . . . . .	89
4.3.2	Direction selectivity characterisation . . . . .	90
4.4	Optogenetic stimulation . . . . .	91
4.4.1	Optogenetically induced spatial receptive fields . . . . .	94
4.4.2	Optogenetic identification of RGCs . . . . .	94
4.5	Matching morphology, function and genetic identity . . . . .	98
4.5.1	Matching morphology and function . . . . .	100
4.5.2	Matching genetic identity and function . . . . .	100
4.6	Discussion and conclusions . . . . .	103
<b>5</b>	<b>Discussion and conclusions</b>	<b>107</b>
5.1	Two-photon microscope . . . . .	108
5.2	Integration of the two-photon microscope with the electrophysiology system . . . . .	108
5.3	Optogenetic stimulation with the $\mu$ LED system . . . . .	110
5.4	Future experiments . . . . .	111
	<b>Acknowledgements and contributions</b>	<b>113</b>
	<b>Bibliography</b>	<b>115</b>
<b>A</b>	<b>Plug system for MEA retinal recordings</b>	<b>127</b>

# List of Acronyms

AAV	Adeno Associated Virus
AU	Arbitrary Unit
CCD	Charge Coupled Device
ChR	Channelrhodopsin
CMOS	Complementary Metal–Oxide Semiconductor
CNS	Central Nervous System
CRT	Cathod Ray Tube
DAQ	Data Acquisition
DLP	Digital Light Projector
DSI	Direction Selectivity Index
EI	Electrical Image
FOV	Field of View
FWHM	Ful Width at Half Maximum
GCL	Ganglion Cell Layer
GDD	Group Delay Dispersion
GECI	Genetically Endoded Calcium Indicators
GUI	Graphical User Interface
GVD	Group Velocity Dispersion
HR	Halorhodopsin
ILM	Inner Limiting Membrane

INL	Inner Nuclear Layer
IP	Inner Product
IPL	Inner Plexiform Layer
ITO	Indium Tin Oxyde
LED	Light Emitting diode
LGN	Lateral Geniculate Nucleus
MEA	Micro Electrode Array
NIR	Near Infra Red
OCT	Optical Coherence Tomography
OLM	Outer Limiting Membrane
ONL	Outer Nuclear Layer
OPL	Outer Plexiform Layer
OptoSTA	Optogenetically induced Spike Triggered Average
PCA	Principal Component Analysis
PCB	Printed Circuit Board
PECVD	Plasma Enhanced Chemical Vapour Deposition
PMT	Photo Multiplier Tube
PSF	Point Spread Function
RGC	Retinal Ganglion Cell
ROI	Region of Interest
SLM	Spatial Light Modulator
STA	Spike Triggered Average
STED	Stimulated Emission Depletion
TPE	Two Photon Excitation
TPLSM	Two Photon Laser Scanning Microscopy
TTL	Transistor Transistor logic
USAF	United States Air Force

# Introduction

Understanding how the human brain processes information is one of the grand challenges of contemporary science. An extensive comprehension of fundamental and pathological neural mechanisms has the potential to uncover revolutionary approaches in the development of neuro-prosthetic technologies, from the treatment of neuro-degenerative diseases (e.g. Alzheimer's disease), to the correction of motor and learning deficiencies.

Such an endeavour is exciting and daunting in equal measure. Traditional methods for neural recordings are largely devoted to record from one neuron at the time, but neural circuit function is likely to arise from complex interactions amongst the many (up to millions) constituents of a neural circuit [1]. To progress, neuroscientific research needs to interact with these levels of complexity with novel, scalable and minimally invasive technologies able to simultaneously interface with a large number of neurons. The requirement for novel technological approaches to brain research has been the driving force of this PhD research: the focus was on the development of an experimental tool able to record and control the patterns of spatio-temporal activity within intact neural networks, *in vitro*, by exploiting neuro-photonics approaches.

The investigations have been oriented towards an approachable part of the vertebrate Central Nervous System (CNS) from which it is relatively easy to record: the retina. The retina is a layered structure which can be thought of as an input output circuit: a visual stimulus is detected by an input layer, the *photoreceptors* cells, processed by *bipolar* and *amacrine* cells circuits and encoded by (*Retinal Ganglion Cells*) RGCs before being transmitted to the brain. Recordings of RGCs activity can lead to significant insights on the neural mechanism behind vision, a fundamental process which might gate to deeper and elusive processes.

An effective method for the characterization of retinal response to visual stimuli at single cell resolution employs planar Micro Electrode Arrays (MEA) to simultaneously record from hundreds of RGCs while presenting a visual stimulus to the photoreceptors [2]. This approach, which led to remarkable results [3], relies on high temporal resolution, sensitivity to single action potentials and scalability over large populations which, in combination with efficient spike sorting algorithms, allow the registration of the unique spiking signatures of functionally characterized RGCs. Unfortunately, MEA recordings of retinal activity yield no direct information about the anatomical or

genetic identity of the recorded RGCs. In fact, even closely spaced electrodes (30  $\mu\text{m}$ ) fail to unambiguously attribute action potentials to an anatomical cell. Moreover, planar MEA recordings are confined to the the Ganglion Cell Layer. A desirable tool for the characterization of retinal circuitry would provide for high-spatial resolution, genetic selectivity and non-invasive penetration to the Inner Nuclear Layer (INL), where amacrine and bipolar cells, which conduct interesting computational operations [4], are hosted.

Over the past decades, advances in the fields of optics, photonics, genetics and neural engineering produced mature technologies which show promising potential to integrate existing methods towards innovative paths in brain research [5]. In particular, two techniques have risen to prominence in the field of neuroscience: two-photon excitation of fluorescence and optogenetic stimulation. Two-photon excitation of fluorescence allows anatomical and functional imaging at depth in intact tissue with minimal photodamage [6]. Optogenetic stimulation allows genetic targeting of neural sub-populations and for neural activity to be activated (or inhibited) with millisecond temporal precision [7]. The research endeavour presented in this thesis aimed to integrate an existing high-density transparent MEA with a custom-made optical system combining a two-photon microscope and a  $\mu\text{LED}$  optogenetic stimulation setup. This system has been designed to combine the advantages offered by MEA recordings, two-photon imaging and optogenetic stimulation in order to provide a tool with high-temporal resolution, high-spatial resolution, genetic selectivity and minimal invasiveness.

This thesis articulates on the construction, validation and application of this tool in five chapters. Chapter 1, “*Background*”, briefly reviews the material behind this interdisciplinary research, covering the basis of retinal structure, optogenetic stimulation, MEA recordings and two-photon excitation of fluorescence. Chapter 2, “*A setup for two-photon microscopy, optogenetics, and MEA recordings*”, describes the construction and validation of the  $\mu\text{LED}$  optogenetic stimulation system and a custom two-photon microscope tailored to integrated with the MEA. Chapter 3, “*Combining Two-Photon Laser Scanning microscopy with MEA recordings*”, deals with the challenges presented by the integration of laser scanning and electrophysiological recordings, demonstrates two-photon imaging through the MEA and explores two-photon optogenetic stimulation experiments. Chapter 4, “*Large scale matching of anatomy and function of retinal ganglion cells*”, demonstrates a novel method which exploits spatio-temporal optogenetic stimulation and large scale MEA recordings to link function with anatomical and genetic identity in RGC sub-populations. The experiments reported in chapter 4 have been performed in collaboration with colleagues at the University of California Santa Cruz. Finally, chapter 5 “*Discussion and conclusions*”, summarizes the outcomes and suggests future directions of research.

# Chapter 1

## Background

The development of advanced technologies, which could meet the challenges of contemporary neural science, is a multidisciplinary research endeavour. In order to set the scene for research in this area, this background chapter aims to collate topics from the various fields that interface with this work. The chapter is organized in five introductory sections. The first three are dedicated to neural cells, electrophysiological recordings and the retina. An exhaustive coverage of these broad topics is beyond the scope of this introduction and the reader is therefore referred to excellent textbooks and reviews on the principles of neural science and retinal organisation [8, 9, 10, 11] to which these first three sections are extensively referenced. The last two sections cover optogenetic stimulation techniques and two-photon microscopy.

### 1.1 A brief introduction on neurons

The mammalian nervous system is composed of two main classes of cells: the glia, or glial cells, and the neurons, or nerve cells. Glial cells greatly outnumber neurons (by a factor of 10 to 50 in humans). The role of glial cells in electrical signalling is not clear, but the different glial cells types (microglia, oligodendrocytes, schwann cells and astrocytes) are known to perform vital roles such as providing structure to the brain, removing debris after neuronal injury or death and helping forming the blood-brain barrier that prevents toxic substances from entering the brain.

Nerve cells or neurons are electrically excitable cells, which process and transmit information by exchanging rapid electro-chemical signals. Despite significant variability among the many neural cell types, nerve cells share a general architecture: a typical neuron appears to be comprised of four morphologically identified regions, shown in figure 1.1. The cell body, or soma, contains the nucleus, where the cell's genes are stored, and the endoplasmatic reticulum, where the cell's proteins are synthesized. Soma dimensions vary from some  $\mu\text{m}$  to tens of  $\mu\text{m}$ . Several short processes, the *dendrites*, branch out of the soma and form the *dendritic tree* that receives most of the incoming

signals. A single, long extension with constant diameter carries nerve signal away from the soma to other neurons, muscles or glands and is known as the *axon*. A point of communication between two neurons is a *synapse*, where a *pre-synaptic* cell transmits information received by a *post-synaptic cell*. Most pre-synaptic terminals, located at the end of the axons, end on post-synaptic dendrites.

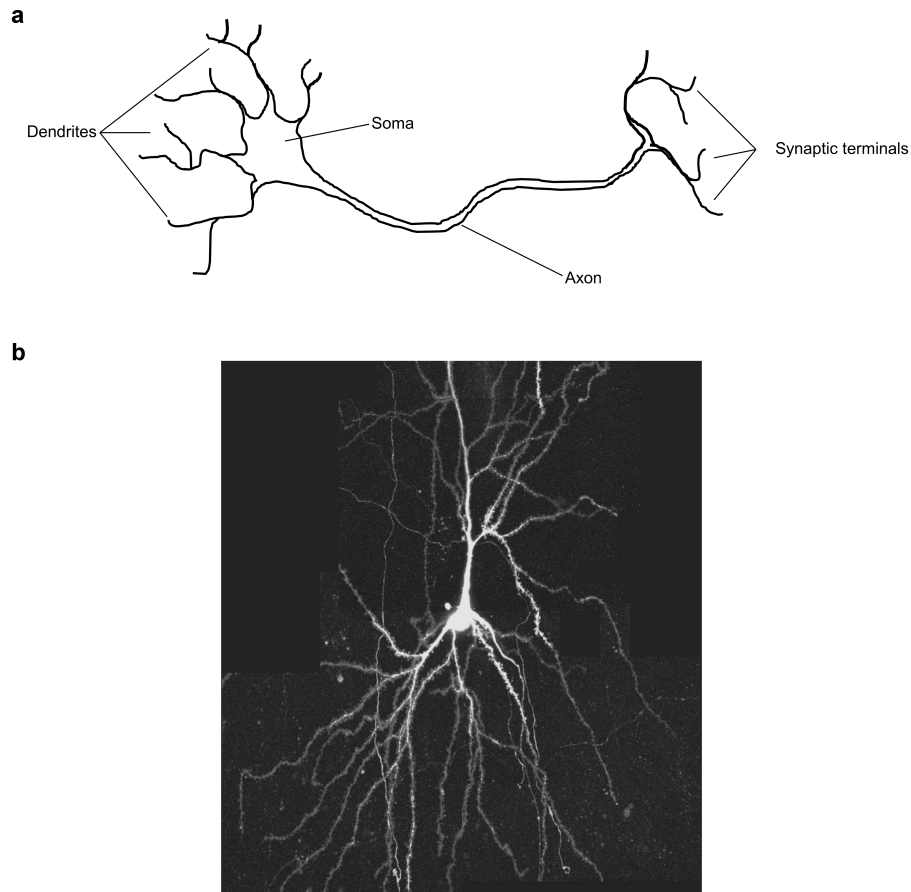


Figure 1.1: (a) Diagram of a typical neuron with the morphologically defined regions outlined: cells soma, dendrites, axon and synaptic terminals (b) Microscope image of a stained neuron obtained with two-photon illumination, reproduced from [12].

### 1.1.1 Membrane potentials and neural signals

As any living cell, neurons have a surface membrane that separates the conductive intracellular environment, the cytoplasm, from the conductive extracellular one. The cellular membrane is a lipid bilayer, composed by two hydrophilic heads containing a hydrophobic core, which is generally impermeable to polar molecules. However, the flow of ions across the membrane has a central role in neural signalling and is selectively regulated by specialized protein molecules, such as ion pumps and ion channels, which span the cell membrane. In resting conditions, neurons maintain a resting membrane potential of about  $-65$  mV across the cell membrane (extracellular fluid potential is here defined at ground potential). This potential arises from unequal distribution of electrically

charged ions on either side of the membrane (e.g.  $Na^+$  or  $K^+$ ) and negatively charged proteins and aminoacids inside the cytoplasm. This unequal distribution is maintained by a protein molecule which pumps  $Na^+$  ions out the cell and moves  $K^+$  ions into the cell. Since the membrane hosts  $K^+$  ion channels, which are open in resting conditions,  $K^+$  ions tend to leak out the cell. If  $Na^+$  ions are pumped into the extracellular medium and  $K^+$  ions are allowed to leave, an excess of negative charge remains in the intracellular fluid.

As previously mentioned, neurons are excitable cells: their membrane potential can be quickly altered by an external stimulus. This property is the cornerstone of neural signalling. A local alteration of the distribution of charge can passively propagate to neighbouring regions of the membrane, carrying information on the occurrence and magnitude of the initial stimulation. In sensory neurons these signals are known as receptive potentials and, by propagating along the axon, can induce the release of chemical substances at the pre-synaptic terminals. These substances, the neurotransmitters, bind with site-specific receptors of the post-synaptic terminal, for example a dendrite in a motor neuron: this chemical reaction generates electrical energy which alters the membrane voltage generating a synaptic potential. The amount of neurotransmitter released is determined by the magnitude of the membrane depolarization, which is graded on the stimulus intensity and duration.

However, this passive propagation of the signal means that the change in membrane potential diminishes in amplitude while travelling along the axon. This mechanism is effective over short distances (a few  $\mu m$ ) but is not suitable for sending information over hundreds of  $\mu m$  or mm. Communication over larger distances is achieved by propagating a relatively large and rapid shift of transmembrane voltage along the axon: action potential. The action potential, often referred to as spike, is a signal which occurs following a sudden influx of  $Na^+$  ions. If the membrane depolarises, for example following a receptor potential, voltage-gated  $Na^+$  ion channels open and  $Na^+$  ions flow into the cells following the electrochemical gradient. If the depolarization reaches an activation threshold, an electrical signal of about 100 mV (measured between inside and outside of the cell) is generated and propagated along the axon. Typically, axon potentials flow from the soma to the synaptic knobs. This is ensured by the ms-long refractory period that voltage-gated ion channels need to recover to the original configuration after being opened.

The action potential amplitude gets regenerated periodically along the axon in a positive feedback fashion that maintains an almost constant voltage drop, unlike receptor and synaptic potentials. Action potentials are highly stereotyped all-or-nothing signals: while no signal is generated below the activation threshold, unlike receptor and synaptic potentials, the same signal is generated by any stimuli above the threshold. The message to be communicated is encoded in the number and the rate at which action potentials are released. When reaching the synaptic knobs, an action potential triggers the release of chemical neurotransmitters. The amount of neurotransmitter release is determined by the number and frequency of the action potentials.

The release of neurotransmitter, which serve as an output signal from the pre-synaptic terminals, is achieved through voltage-gated  $Ca^{2+}$  channels which are set open by the action potential and allow for an influx of  $Ca^{2+}$  ions under the drive of the electrochemical potential (in normal conditions,  $Ca^{2+}$  ions are much more abundant in the extracellular fluid). The incoming  $Ca^{2+}$  ions, besides contributing to depolarization as  $Na^+$  ions do, convey information on the membrane potential change to the intracellular mechanism responsible for neurotransmitter release. Measuring the concentration of  $Ca^{2+}$  ions against time in the extracellular fluid can therefore yield information on the spiking activity of nerve cells: section 1.5 will cover this concept in the context of  $Ca^{2+}$  imaging with multiphoton microscopy.

The different phases of axon potential are outlined in figure 1.2: a rising phase in which the membrane gets depolarized, a peak phase of maximum depolarization, a falling phase where the membrane potential steers back to the resting condition and two final phases, where after an undershoot the membrane potential resting condition is recovered over a refractory period where the cell cannot generate a subsequent action potential.

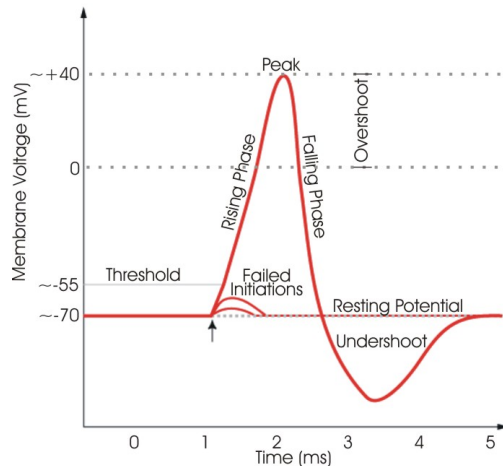


Figure 1.2: Schematic of an action potential as measured using the intracellular recording method. Starting from a resting potential of -70 mV, if the activation threshold is reached, the transmembrane potential rises to a positive voltage and quickly (ms) falls to a negative phase that settles back to the initial state after a negative rebound.

Measuring action potentials activity is key to understand the functioning of neural networks. The experimental techniques used to record action potentials and, in general, the electrical properties and behaviour of nerve cells pertain to the field of electrophysiology, as detailed in the next section.

## 1.2 Electrophysiological recordings

The goal of electrophysiological recordings is to characterise the behaviour of ion channels, nerve cells or networks of nerve cells by monitoring the membrane potential and its changes. For example,

the ionic mechanism underlying the action potential has been discovered with a technique called voltage clamp [13]. The voltage clamp consists of two electrodes connected to a source of current. By placing an electrode inside the cell and one in the extracellular fluid, it is possible to pass current through the membrane and keep the membrane potential locked at a certain value. Ion channels keep opening and closing but any change in membrane potential dictated by ion currents is prevented by the voltage clamp. The effect that membrane potential changes have on membrane conductance for individual ion species can be measured by the amount of current required to maintain the membrane potential at set voltages.

In order to investigate the functional properties of individual ion channels, voltage-clamp techniques have been refined in patch-clamp techniques. In patch-clamp recordings, a glass micropipette is pressed against the cell membrane. The micropipette, usually filled with a conductive solution similar to the extracellular fluid, has a  $\sim 1 \mu\text{m}$  wide opening at the tip and can be tightly sealed to the membrane with a small amount of suction. The tight seal is advantageous because it conveys all the membrane current towards the electrode, like a high shunt resistor. A similar technique utilises micro needle electrodes with a conductive tip, e.g. tungsten, instead of a glass micro-pipette: thanks to higher impedance (but still lower than the tight seal impedance) such electrodes can provide stable recordings and a better signal-to-noise. Patch-clamp recordings have been and are widely used in neuro-scientific research and can be combined with staining protocols, where the recorded cell is injected with a fluorescent dye for anatomical imaging.

While intracellular recording are the best choice for recording synaptic activity, it is possible to record action potentials by positioning an electrode in the vicinity of a cell. Extracellular recordings with micro-electrodes have been extensively used to study neurons of the central nervous system. While having the advantage of being more viable in vivo (where it is difficult to maintain a stable intracellular connection), extracellular recordings are less suited to detect synaptic activity. Moreover, since no tight seal conveys the membrane current along the electrode, extracellular electrodes have to work at low impedance and typically record voltages in the hundreds of  $\mu\text{V}$ . However, micro-electrodes for extracellular recordings can be engineered in large scale arrays, which can record from hundreds of neurons simultaneously, achieving scalability unattainable with patch-clamp techniques. This work employs a planar high-density micro-electrode array (MEAs) to record activity from retinal ganglion cells.

### 1.2.1 Micro-Electrode Arrays

As anticipated in the introduction, this work aims to combine large-scale, high-density electrophysiological recordings of the retinal ganglion cell activity with optogenetic stimulation and multiphoton imaging. The employed MEAs count 61 or 519 electrodes arranged in an isosceles triangular lattice to cover a hexagonal region. Three arrays have been used:

- a 519 electrode array with 30  $\mu\text{m}$  electrode spacing covering an hexagonal region of  $\sim 0.43 \text{ mm}^2$  (450  $\mu\text{m}$  a side);
- a 61 electrode array with 30  $\mu\text{m}$  electrode spacing covering an hexagonal region of  $\sim 0.03 \text{ mm}^2$  (120  $\mu\text{m}$  a side);
- a 61 electrode array with 60  $\mu\text{m}$  electrode spacing covering an hexagonal region of  $\sim 0.12 \text{ mm}^2$  (240  $\mu\text{m}$  a side).

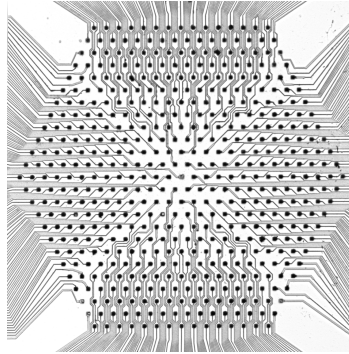


Figure 1.3: Brightfield image of a 519 MEA. The black dots are the electrodes, fabricated at a 30 pitch, after platinisation. The grey lines are conductive Indium Tin Oxide (ITO) tracks which connect each electrode to the readout electronics. The area covered by the array is  $\sim 0.43 \text{ mm}^2$ .

MEAs have been fabricated [14, 15, 16] in the transparent conductor indium tin oxide (ITO) coated over a glass substrate (1.1 mm thick). ITO conductive wires are patterned by using a reactive ion etching technique and then protected with a silicon nitride passivation layer. Electrodes and bond pads are then exposed with a selective reactive ion etching process that does not etch the ITO. The impedance of the electrodes contact area (5  $\mu\text{m}$  in diameter) is reduced to hundreds of  $\text{k}\Omega$  by electroplating platinum at high current densities that produces a fractal-like structure and increases the sensitive area of the electrode. These MEAs have been successfully utilised in the characterisation of retinal circuitry [2, 3].

### 1.3 Neural structure of the vertebrate retina

The retina is a part of the central nervous system whose investigation is an approachable way to give insight to deeper regions of the brain. In fact, as detailed in the following paragraphs, the retina can be thought as a transducing circuit where different cell types perform different functions in the global task of detecting and processing a visual scene. Moreover, input and output operations are performed in well defined, planar cellular layers that can be conveniently interfaced [2].

The investigation of retinal functioning has been pursued by hundreds of researchers over decades: this section will introduce the reader to the fundamental concepts of retinal circuitry, which are

pivotal in this research. A comprehensive coverage of the retina can be found in updated reviews [4], excellent reference books [10] and dedicated websites [11].

### 1.3.1 Anatomy of the vertebrate eye

The eyes of all vertebrates are based on a common plan that resembles the design of a pinhole camera. The incoming light passes through the pupil, an aperture in the front of the eye and forms an inverted image on the retina; the amount of light which is allowed to pass is controlled by a coloured circular muscle that controls the size of the pupil, the iris. In order to produce a sharp image, light is focused on the retina by the cornea, a transparent external surface that covers the pupil and the iris, and the crystalline lens, a transparent body sitting behind the iris and suspended by ligaments. Under the action of ciliary muscles, the lens changes its size in order to accommodate images of closer or further objects on the retina. The whole eye structure, the eyeball, is contained by a fibrous tissue called the sclera (the white part of the eye). The rigidity of the eyeball is due to intraocular pressure produced by a fluid secreted by cells in the ciliary body. The retina lies at the back of the interior part of the eye, separated from the lens by a gelatinous body, the vitreous humour. The retina is a sheet of neural tissue, part of the central nervous system, which is connected to the brain via a bundle of nerve fibers called optic nerve. The optic nerve travels into the brain to project retinal signals into the Lateral Geniculate Nucleus (LGN) and then the visual cortex. Despite being a fundamental part of the vision process, what happens after the optic nerve has left the eye is not covered in this introduction and instead the reader is directed to reference [9].

The choroid lies between the retina and the sclera and is a pigmented tissue which supports a meshwork of blood vessels responsible for the choroidal blood supply to the outer retina. The inner retina is served by a second circulation system, the retinal one, which is composed by arteries and veins that enter the eye along the optic nerve before branching in a dense network of capillaries. It is worth noting that the metabolic demands of the retina are the highest of any tissue in the body, when the mass of tissue involved is considered. The eyeball is positioned inside the orbital cavity by ligaments and extra ocular muscles, which allow the orientation of the direction of gaze and the focus of the image on the most sensitive part of the retina, the fovea.

### 1.3.2 Anatomy of the vertebrate retina

The retina is a circular disc, approximately 0.4 mm thick, which lies at the back of the eye and extends towards the lens. In humans, the retina covers approximately 30 to 40 mm in diameter [10, 11]. Portions of the retina are distinguished by their position within the facial system. In the horizontal direction, retinas are divided into nasal sections (close to the nose) and opposing temporal sections (lateral side of the eye). In the vertical direction, the upper part is known as

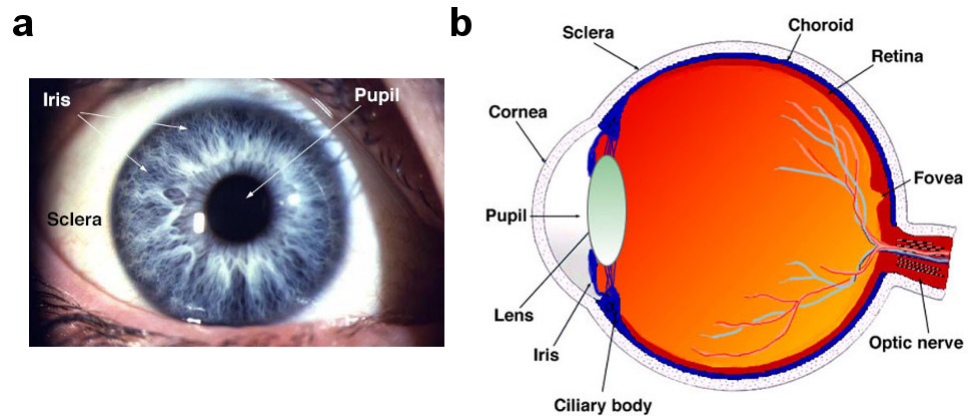


Figure 1.4: (a) Front view of the human eye with the iris, te pupil and the sclera indicated by arrows. (b) Noted diagram of the sagittal section of the adult human eye. H.Kolb [11] CC-BY-NC-ND.

dorsal retina while the lower part is the ventral retina. An image of the retina can be obtained with an ophthalmoscope, an optical instrument which illuminates the back of the eye and images the retina in reflection. An ophthalmoscope image of the retina, a fundus image, is a useful diagnostic tool which clearly highlights distinctive retinal features, such as the optic nerve and the branches of retinal vasculature. As shown in a human fundus image, figure 1.5, retinal arteries and veins emerge from the optic nerve and branch to nourish the inner retinal layers. The blood-vessel free area, which can be seen in a fundus image, as figure 1.5, is the fovea: the region where cones photoreceptors are packed at maximum density to confer sharp visual acuity.

From a neural point of view, the vertebrate retina is a highly layered structure which, by broad classification, is composed of five classes of neurons: photoreceptors, bipolar, horizontal, amacrine and ganglion cells. Cells of each class occupy specific layers within the thickness of the retina. In vertebrate retinas, these classes are organized in three layers of cell bodies and two layers of synapses, as shown in figure 1.6. Starting from outer segment of the retina, at the back of the eye, the Outer Nuclear Layer (ONL) contains rod and cones cell bodies, which connect to bipolar and horizontal cells in the Outer Plexiform Layer (OPL). Bipolar and horizontal cells bodies are hosted in the Inner Nuclear Layer (INL) together with amacrine cells. Ganglion cell bodies receive synaptic input from bipolar, horizontal and amacrine cells in the Inner Plexiform Layer (IPL) and send axons towards the optic disc in the fiber layer. A diagram of retinal structure is outlined in figure 1.6. Incoming light travels through the thickness of the retina and gets detected by photoreceptors, whose signals to bipolar and horizontal cells is dictated by changes in the visual science. Ganglion cells receive an input from the network of bipolar, horizontal and amacrine cell and encode for complementary representations of the visual scene that are transmitted to the visual cortex.

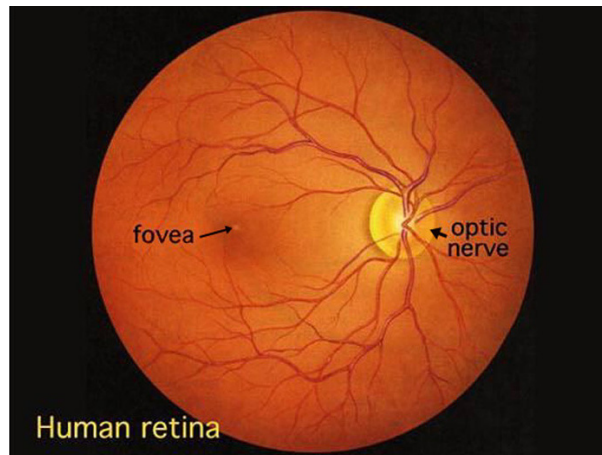


Figure 1.5: Fundus image of a human retina: the fovea, the optic nerve and the retinal vasculature are clearly distinguishable. H.Kolb [11] CC-BY-NC-ND.

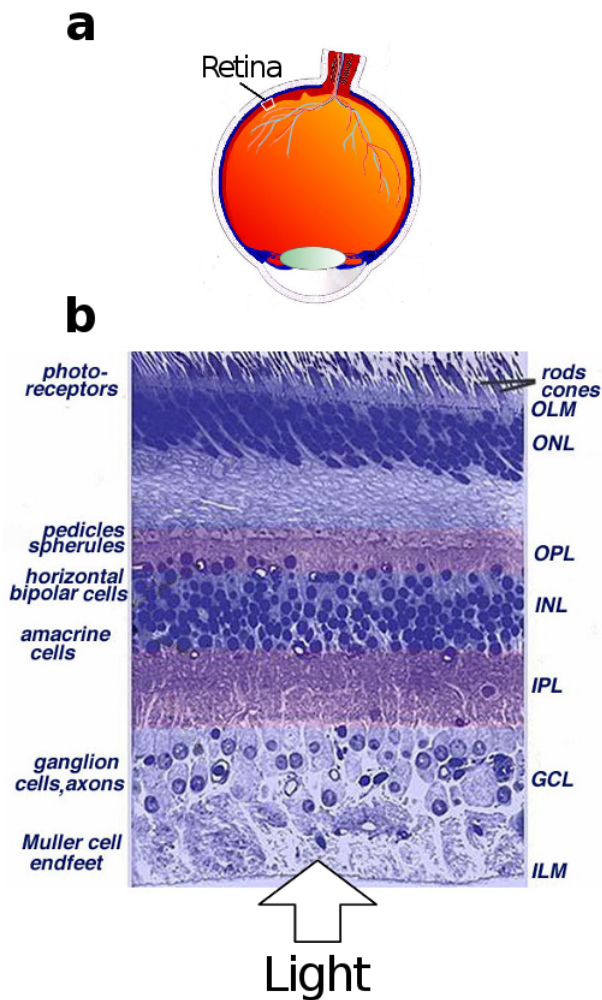


Figure 1.6: (a) Sagittal section of the human eye showing the position of the retina. Modified from H.Kolb [11] CC-BY-NC-ND. (b) Light micrograph of a vertical section through the central human retina. The image highlights the layered structure in which the different retinal cell classes are organized. The labels on the left side indicate the location of cells types; the labels on the right side indicate layers nomenclature acronyms. The arrow at the bottom indicates the direction followed by the incoming light. Modified from H.Kolb [11] CC-BY-NC-ND.

### 1.3.3 Retinal cell types

The retinal circuitry contributes significantly to the formation of an image from a visual scene: its function is a matter of vibrant research and although a lot is known, there is still much left to discover. This introductory section will outline the major pathways involved in the detection and processing of a visual scene within the retinal circuitry. Again, the reader is referred to [4, 8, 10, 17] for an extensive coverage.

#### Photoreceptors

Photoreceptors cells lie at the back of the retina and are morphologically organized in an outer segment, an inner segment, a nucleus and a synaptic terminal. Light is detected by a visual pigment in the outer membrane, where the incoming photons are funnelled in a wave-guide fashion by the high-density inner segment. Among vertebrates, photoreceptors exist in two classes named after the characteristic shape of the outer segment: rods, which work in dim conditions, and cones, which are less sensitive than rods and work in bright conditions. Most mammalian retinas are rod dominated and confine cones in specialised areas of the retina as, for example, the foveal region in primates and raptors. Mammals typically possess a single rod type, which contain the visual pigment rhodopsin, and multiple cone types which are differentiated by the opsin protein they contain. Different opsin proteins confer different spectral sensitivity to the hosting cone, providing the basis of colour vision. Primates have three cones types which respond primarily to blue (S-cone), green (M-cone) and red (L-cone) wavelengths; in most mammals the red cone is absent.

The signal generated by rods and cones consists in the variation of the amount of neurotransmitter (glutamate) released to bipolar cells. In the dark, photoreceptor cells are depolarised and release neurotransmitter; when exposed to light the cells are hyperpolarised and the neurotransmitter release rate drops. This response to incoming light is transmitted to the inner retina by means of connections to horizontal cells and bipolar cells. It is worth noting that photoreceptors also connect to each other [10] and receive feedback from amacrine cells, as mentioned later.

#### Horizontal cells

Horizontal cells provide inhibitory feedback to rods and cones. They sample the output from the photoreceptors over a relatively wide region of illumination, and, through feedback, tune the output signal in order to keep the retina within its operating range. For example, horizontal cells prevent bright objects on a dark background from saturating the photoreceptor response in certain locations. Morphologically, horizontal cells exist in two types in most mammals and a single type in some rodents. Both types, termed HI and HII, have a small dendritic arbour around the cell body; in addition HI cells have a long axon at the end of which a telodendritic arbour branches

out. HI and HII cells also connect with other cells of the same type via gap-junctions providing for different inhibition mechanisms.

## Bipolar cells

Bipolar cells receive input from the photoreceptors in the OPL, have their cell body in the INL and connect with ganglion cells in the IPL. By releasing neurotransmitters at their synaptic output, bipolar cells transmit and process the signal of the photoreceptors. It is possible to distinguish rod bipolar cells (a single cell type which connect to rods only) and cone bipolar cells (multiple cell types which connect with cones). The types of bipolar cells observed in the mouse retina sum up to 11 cone bipolar plus 1 rod bipolar [18]; figure 1.7 summarises their morphology. These bipolar cell types, which differ structurally and molecularly, decompose the signal generated by photoreceptors and transmit it to the inner retina by creating parallel information channels. While the rod bipolar is devoted to rod pathways, the multiple types of cone bipolars connect with all the cone synapses within their reach. Cone bipolar cells can be classified according on the number of cones they connect to (e.g. midget or diffuse bipolar), the cone type they connect to and the response to the visual stimulus: while ON bipolars tend to respond to an increase of light on their receptive field, OFF bipolar tend to respond following a cessation of light stimulus. Figure 1.7 summarises the types of bipolar cells in the mouse, elucidating how OFF-bipolar cells have synapses in the outer part of the INL and ON bipolar have synapses in the inner part of the INL.

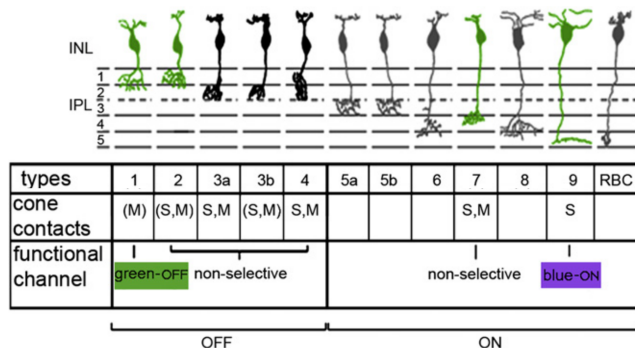


Figure 1.7: A table of the various bipolar cell types and their connectivity. Different cone bipolar cell types may or may not select the cone type from which their receive. The figure shows how OFF bipolar, left group, and ON bipolar, right group, tend to stratify their synapses in different sub-layers. Adapted by [4] from [19] and [18].

## Amacrine cells

Amacrine cells lie in the lower portion of the inner nuclear layer and are diversified over approximately 30 cell types with very different structural features. Amacrine cells exchange input and output signals with other amacrine and bipolar cells and are presynaptic to ganglion cells. Although the

specific role played by the different types of amacrine cells is not yet known, overarching principles have been suggested. In first instance, amacrine cells might induce context dependent responses in the ganglion cells, e.g. object motion detection; in second instance, amacrine cells might perform vertical integration by connecting ON and OFF strata in the IPL. As a general rule, amacrine cell type functions are believed to be narrowly task-specific. Amacrine cells transmit signal by releasing neurotransmitters. Finally, it is worth noting that the total number of amacrine cells is greater than the number of horizontal or ganglion cells. While an example of a narrow field amacrine cell in the mouse retina is displayed in figure 1.9, figure 1.8 displays the various amacrine cell types found in the rabbit retina, where the investigation of this cell class has been conducted most systematically [4].

## Retinal Ganglion cells

Retinal Ganglion Cells (RGCs) are the final output of the vertebrate retina, which receive and combine inputs from bipolar and amacrine cells before projecting to the brain. The different aspects of the visual scene, decomposed by the retinal circuitry, are encoded in the firing rate at which RGCs release action potentials. Retinal ganglion cells are, in fact, spiking neurons. Retinal Ganglion Cells types have been classified based on morphological criteria: a detailed study in the mouse has identified 22 RGC types, as shown in figure 1.10 [20].

Attributing a function to the known morphological types of RGCs is a challenging task addressed by an active line of research. Recent work concluded that differentiation based on functional light responses combined with the basic anatomy could identify more than 30 different RGCs functional types in mice [21].

In order to set the scene for the last chapter of this thesis, which will report on a proposed method to connect anatomy and function in genetically targeted subpopulations of RGC in the mouse, it is worthwhile outlining major functional families of retinal ganglion cells types such as ON- and OFF-ganglion cells and direction selective cells. ON-RGCs increase the firing rate when a spot of light impinges on the centre of their receptive field, the spatial area which contains the photoreceptors that directly activate the cell via bipolar pathways. Conversely, OFF-RGCs increase their firing rate when a spot of light impinges outside their central receptive field (the so-called surround area). A third family exist, the ON-OFF RGCs which increase the firing rate following the onset and offset of light on their central receptive field. The polarity properties of ganglion cells derive from the bipolar cells they connect to: while the dendrites of ON-ganglion cells co-stratify with ON-bipolar cells in the inner strata of the IPL, the dendrites from OFF-bipolar cells co-stratify with OFF-bipolar cells in the outer strata of the IPL; ON-OFF cell co-stratify with both ON- and OFF-bipolar cells. Some ganglion cell types are sensitive to the direction of motion of an object with respect to the background and are collectively termed Direction Selective ganglion cells, abbreviated as

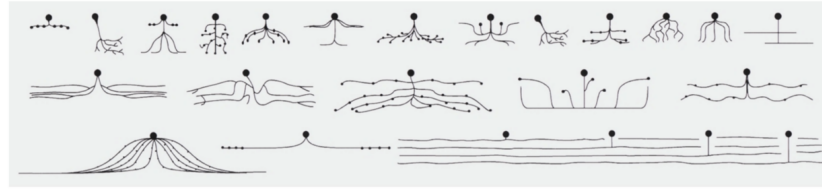


Figure 1.8: The several amacrine cell types found in the rabbit retina. Wide field amacrine cells are not shown. Adapted from [17].

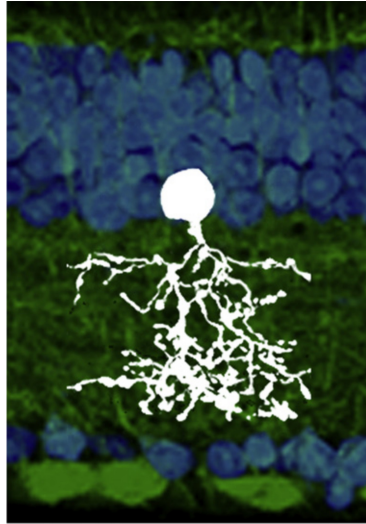


Figure 1.9: Detail of a narrow field amacrine cell in the mouse retina, extending from the INL to the IPL. Adapted from [4].

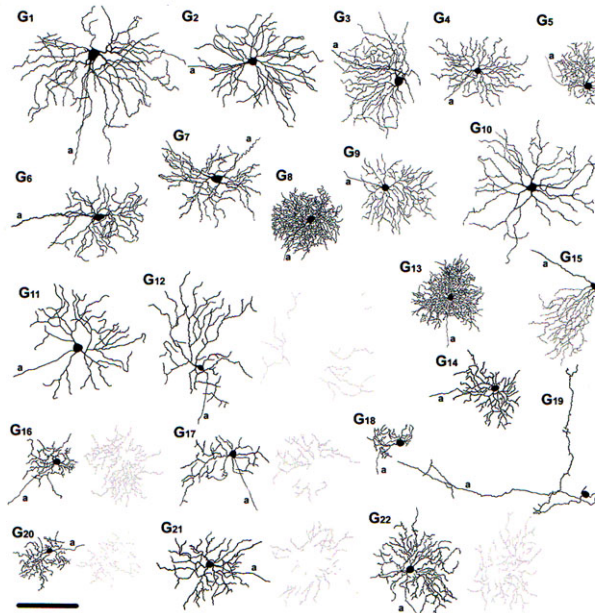


Figure 1.10: Summary diagram showing representative ganglion cells in the mouse. Each ganglion cell subtype is labeled as G1–G22. In case of ganglion cell which bistratified dendritic tree (e.g. G22), proximally and distally stratifying dendrites are shown in black and grey, respectively. The letter *a* indicates the axon. Scale bar is 100  $\mu\text{m}$ . Original figure from [20].

DSDS cells discriminate between different angles of motion and can have different polarity [21, 22].

## 1.4 Optogenetics

*Optogenetics* refers to the combination of optical and genetic methods used to excite or inhibit well-defined events, such as neuron signalling, in living cells, healthy tissue or behaving animals. This technology, whose foundations have been reviewed following its establishment in the neuroscientific community [7], has been instrumental in many discoveries [23].

The technique relies on transfecting living neurons with microbial opsin genes, which give rise to membrane-bound light-activated ion-channels and pumps. Upon illumination, the ion-channel (or pump) opens and allows an inflow or outflow of certain ion species which, as previously seen, alters the transmembrane potential. If the membrane gets depolarized, the voltage is closer to the activation threshold and an action potential is more likely to be generated; conversely, neural signalling is inhibited when the membrane is hyperpolarized. Figure 1.11 exemplifies the concept for two common opsin proteins: one activatory, Channelrhodopsin, and one inhibitory, Halorhodopsin. The first demonstration of precisely-timed (ms) optogenetic control of spiking activity in mammalian neurons has been achieved with a single-component microbial opsin [24].

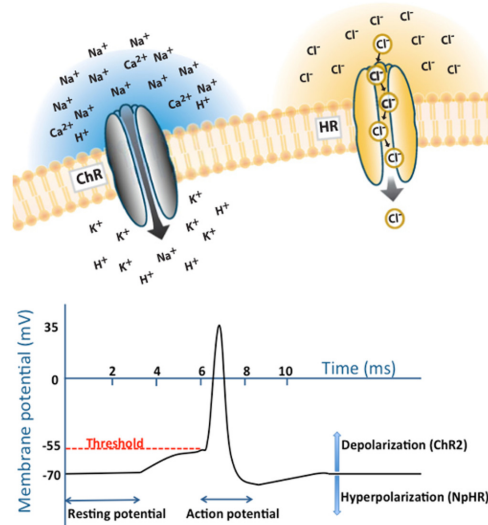


Figure 1.11: Functioning of common optogenetic constructs for stimulation (ChannelRhodopsin, ChR) and inhibition (Halorhodopsin, HR) of neural activity. *Top*, diagram of ChR and HR opsin proteins embedded with the cell membrane, adapted from [7]. *Bottom*, effect of depolarization and hyperpolarization on transmembrane potential.

Optogenetic experimentation is founded on four main components, which will be covered in the following: microbial opsins, methods to deliver sufficient opsin gene expression to targeted cellular elements, methods to deliver light stimulation and compatible readout technique to record the manipulated neural activity. Previously covered large scale electrophysiological recordings provide

high spatio-temporal resolution and, in combination with optogenetic stimulation techniques, can provide high-throughput data from single neurons in genetically targeted sub-populations as reported in chapter 4.

### 1.4.1 Microbial opsin proteins and channelrhodopsin

The first observation of microbial opsin proteins functioning as single-component light-activated ion pumps in microbial organism, bacteriorhodopsin [25], opened an active field of research which, over the following decades, characterized the genetic, structural and functional features of other major classes of ion-conducting microbial proteins of the same family, e.g. halorhodopsins [26, 27] and channelrhodopsins [28].

After the initial inception of single-component microbial opsin genes in mammalian neurons, the three major classes of microbial opsin proteins have been successfully employed as optogenetic tools. This introductory section will focus on Channelrhodopsin, being the only optogenetic probe employed in the reported experiments; other constructs and the development of innovative probes are covered in dedicated reviews [7, 23].

Channelrhodopsin is a microbial opsin gene, which encodes for a single-component light-activated cation-channel [28]. Upon blue-light illumination, a cation pore is opened which, in neurons, predominantly results in a cation flow down the electrochemical gradient (from the extracellular to intracellular fluid) that causes depolarization. In channelrhodopsin, the ion conducting activity does not depend on the photocycle and the ion flux is rather dependent on the kinetics of channel closure. A common variant utilised in early experiments, ChR2 [29], is characterized by a relatively quick off kinetics of ( $\sim 10$  ms) and low channel conductance [30]. Subsequent developments of opsin probes modified the native algal codons with mammalian codons producing hChR2 (humanized Channelrhodopsin) in order to achieve higher expression levels [31]. A widely used variant of channelrhodopsin, referred as hChR2(H134R) and generated by introducing a point mutation, exhibits twice as high photocurrents at the expense of slower channel closure kinetics ( $\sim 18$  ms) [32]. While higher photocurrents are desirable, the slower kinetics might be a limit for application in fast spiking neurons.

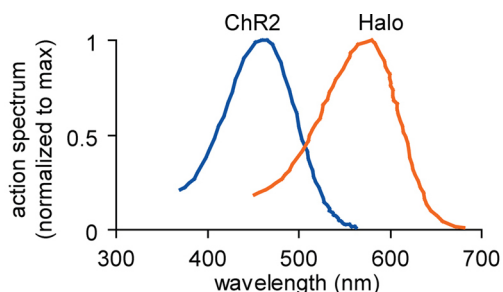


Figure 1.12: Absorption spectra for Channelrhodopsin, yellow, and Halorhodopsin, blue. Adapted from [33].

### 1.4.2 Genetic expression

Specific targeting of the optogenetic probe to the desired cell type, where “cell type” is intended as a population of neurons that cannot be divided into smaller units [34], is of paramount importance in optogenetic experiments. In fact, one of the key advantages offered by optogenetics is the manipulation of a genetically targeted subset of neurons: this allows the dissection of a neural circuit of interest by factoring out the contribution of non-targeted neurons. Opsin targeting of neural cells is accomplished with diverse strategies as viral transfection, transgenic mutations and electroporation.

Viral expression of optogenetic probes is obtained by infecting the target neurons with viruses that act as vectors to deliver opsin genetic materials into the cells. Specificity of viral transfection is achieved by selecting or assembling viral constructs which exhibit anatomical or genetic selectivity. This is achieved by modifying the protein coat which encapsulated viral genetic material. For example, adeno-associated virus (AAV) viral vectors, the most popular viral family for optogenetic targeting, can be engineered to preferentially enter the cells through axon terminals, thus allowing projection specific targeting. In the mouse, the generation of transgenic animals is another major strategy for opsin expression. This approach allows expressing opsin probes in cells where a specific promoter, which is a region of DNA that initiates the transcription of a certain gene, is found. For example, various studies have exploited a mouse line where a protein fusion between ChR2 and the fluorescent molecule eYFP is expressed under control of the Thy1 gene promoter (the mouse line is known as Thy1-ChR2-EYFP) [7, 35]. In addition, it is possible to express opsin probes with genetic techniques known as recombinase technologies [7]. These methods rely on enzymes, such as Cre-recombinase, that can insert, excise or modify DNA segments by recognising the location of a precise genetic sequence. This approach, which is well suited for opsin targeting, is typically employed by crossing two mice lines. In the first line, opsin genes are inserted in most cells but their transcription is inhibited by a DNA region known as STOP codon. This STOP codon, in turn, is flanked by the DNA sequence recognised by the Cre-recombinase enzyme. In the second line, Cre-recombinase is expressed in a specific cell population (for example neurons with parvalbumin). When the lines are crossed, the Cre-recombinase recognises the DNA location of the STOP codon and excises it, thus prompting the expression of optogenetic probes in the Cre-expressing cells types (parvalbumin neurons in our case). The availability of numerous Cre-recombinase lines in the mouse enables a wide panel of cell types to be targeted with optogenes: as reported in the following chapters, this work has taken advantage of this technology.

Electroporation, a common technique in cell research, introduces DNA into cells by permeabilising the cellular membrane with an electric field [36]. In optogenetic experiments, electroporation can be used to target up to a few dozen neurons, located *in vivo* with multiphoton microscopy, with a plasmid-filled patch pipette [34]. Neurons can be targeted based on their morphology, functional

properties or genetic identity. This provides tremendous precision and targeting for detailed neural circuit analysis, but at the cost of invasiveness and scalability to larger numbers of neurons.

### 1.4.3 Light delivery for optogenetic stimulation

The application of optogenetic manipulation in neuroscientific research encompasses a variety of different investigations [23]. In order to meet the requirements of diverse experimental design, a range of optical strategies have been developed to deliver light stimulation to the targeted neurons with the desired level of spatial, temporal and spectral control [34]. A key parameter in the designing of an optogenetic experiment is the photon flux or light power density which illuminates the targeted neurons. The minimal light power density needed to achieve optogenetic activation depends on the opsin of choice and on the stimulation wavelength. As a benchmark, action potentials have been reliably elicited with a stimulation of  $P \sim 1 - 5 \text{ mW/mm}^2$  at 473 nm in wild-type ChR2 preparations [7, 24].

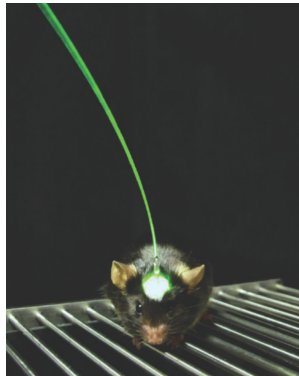


Figure 1.13: An example of fiber optic implant for optogenetic stimulation in the mouse. Adapted from [23].

The estimation of light power density delivered to a targeted location correlates with the size of the stimulated volume and is a key task, made non-trivial by the contribution of the illuminating beam divergence combined with scattering and absorption of light travelling through neural tissue. As a result, the activation volume depends on the illuminating wavelength and upon the spatial profile of the light source. In addition to experimental validation, the propagation of light through neural tissue is usually simulated with Monte Carlo methods. Among the many commercially-available light sources that can readily provide enough power, sources that emit at medium to high power with a narrow spectral bandwidth and that allow a fast temporal control are generally preferred. While an extended discussion of the optical strategies commonly employed in optogenetics can be found in [34], two sources are of particular interest for what concerns this work: laser beams and  $\mu$ LEDs arrays.

Lasers are a convenient choice for many optogenetic applications because they can deliver plenty of

power at a very narrow linewidth that can be matched to the opsin peak absorption by choosing the appropriate laser medium. Due to a very low divergence, laser beams can be optically manipulated or coupled with fiber optics without wasting a major portion of the initial power. Recent advances have exploited the inherent coherency of laser-generated wavefronts to implement holographic stimulation over many neurons across three dimensions [37]. Following the development of red-shifted opsins and the demonstration of two-photon optogenetic stimulation [38], which is covered in section 1.5.3, IR lasers sources have received increasing attention in the optogenetic community [39] where they were already widely employed for two-photon microscopy. Light-Emitting Diodes (LEDs) are another appealing light source which has been successfully applied in optogenetic experiments [40]: they are inexpensive, easily modulated at the desired frequency and emit with a relatively narrow spectral linewidth (tens of nm). LEDs have, however, highly divergent light output that can result in power losses when coupling with optical elements, such as fiber-optics or collecting objectives. The result is that high-power emitters are often needed to reach the required power output at the neuron level. LEDs can be miniaturise to microscopic size and engineered in single-element addressable arrays, which allow for the generation of high-resolution spatio-temporal patterns. Interesting research has demonstrated the potential of  $\mu$ LED devices implanted or delivered *in vivo* [41], with special attention to heating effects, or employed for stimulation of single cells and neurites *in vivo* [42].

In the present work, an array of high-power blue  $\mu$ LED, fabricated within the Institute of Photonics, is used to optogenetically identify ChR2 expressing retinal ganglion cells in large-scale retinal electrophysiology experiments (see chapter 4). These  $\mu$ LED arrays are composed by 256 square GaN LED pixels, 100  $\mu$ m a side, which are arranged in a 16 x 16 matrix and bonded to a CMOS chip. The CMOS control allows each element to be individually modulated at hundreds of MHz [43].

## 1.5 Two-photon microscopy

Since its inception [44], the application of two-photon excitation of fluorescence to microscopy and molecular manipulation, has earned a forefront role in neuroscientific research. A variety of imaging modalities have been developed alongside manipulation techniques [45, 46]. This introductory section has no ambition of covering the whole field and rather aims to convey a general understanding of the topic while underlying the features of multiphoton microscopy which are more relevant to the present work. An extensive description of the quantum physics and 3D imaging theory underlying two-photon microscopy is beyond the scope of this introductory chapter and can be found in [47].

### 1.5.1 Foundations

The physical phenomenon of fluorescence occurs when a molecule, known as a fluorophore or chromophore, gets excited to a higher electronic state following the absorption of a photon. The fluorophore then returns to the ground state by radiative decay, emitting a secondary photon at a longer wavelength. Typically, fluorophores are excited with UV or green-blue light.

As predicted by M. Goepfert-Mayer in 1931 [48], a molecule can undergo a fluorescence cycle following the simultaneous absorption of two photons that, by combining their energy, cause the chromophore to transition to an excited state. This process is referred as Two-Photon Excitation of Fluorescence (TPEF).

Intuitively, a fluorophore that is excitable with UV light could also make the electronic transition to an excited state by simultaneously absorbing two IR photons. As an approximate rule, one-photon,  $\lambda^{1P}$ , and two-photon,  $\lambda^{2P}_1, \lambda^{2P}_2$ , exciting wavelengths are linked by the following equation:

$$\frac{1}{\lambda^{1P}} \simeq \frac{1}{\lambda^{2P}_1} + \frac{1}{\lambda^{2P}_2}. \quad (1.1)$$

An energy diagram exemplifying one-photon and two-photon transitions is shown in figure 1.14.

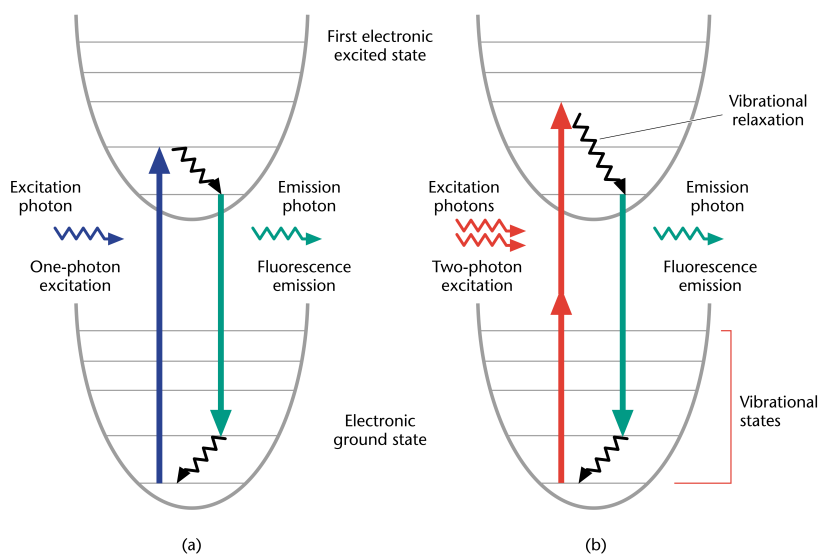


Figure 1.14: Comparison of Jablonski diagrams for one-photon (*left*) and two-photon (*right*) fluorescence excitation. In two photon excitation, the energy is provided by two longer-wavelength photons impinging on the molecule at the same time [49].

While the radiative decay that generates the fluorescent photons is identical, once the excited state has been reached [50], and the emission spectra overlap (figure 1.15), the cross sections of two-photon excitation are extremely low. In the NIR spectrum, common fluorophores have two-photon excitation (TPE) cross-sections that range from 1 to 300 GM, where  $1 GM = 10^{-50} \text{cm}^4 \text{s photon}^{-1}$

[51]. Large intensities are therefore required to obtain a sizeable two-photon absorption and the first reported experimental observation was achieved in 1961, illuminating a europium doped crystal with a ruby laser [52].

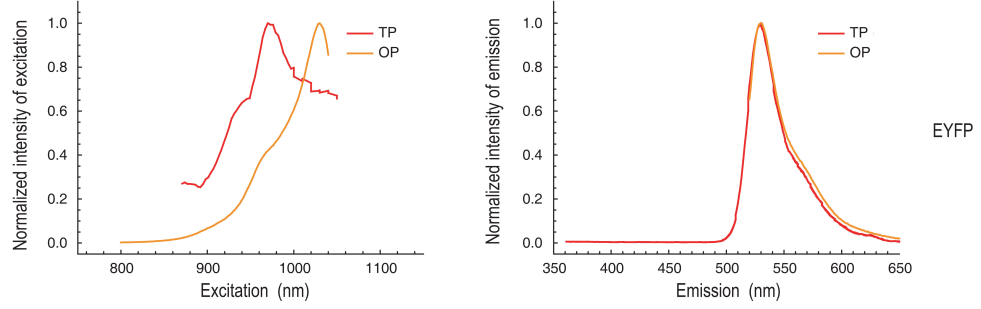


Figure 1.15: Comparison of one-photon and two-photon absorption and excitation spectra for the fluorescent protein eYFP. The excitation wavelength in the single photon absorption spectrum was multiplied by two for display reasons. Adapted from [53].

Following a wide application in spectroscopic studies [54], the advent of mode-locked lasers sources, capable of generating high-power pulses ( $\sim 100$  fs at  $\sim 100$  MHz) with low average power, has been instrumental in the development of multi-photon microscopy [55]. Two-photon laser-scanning microscopy (TPLSM) [44] has rapidly established itself as a valuable tool across the life-science community: in fact, the non-linear nature of two-photon absorption enables two-photon microscopy to achieve optical sectioning while imaging at greater depth into the specimens [56].

The higher penetration depth of NIR wavelengths is due to the optical properties of biological tissue in the so-called NIR-optical window, the spectral region commonly used in biological imaging where light has its maximum penetration depth, as shown in figure 1.16. Across this window, the attenuation of excitation light is dominated by scattering over absorption [57]. NIR wavelengths have a lower scattering coefficient and are better suited to penetrate deeper into the tissue. For example, in human gray matter the scattering coefficient has been measured to be  $\mu_s = 10.6 \text{ mm}^{-1}$  for at 510 nm versus  $\mu_s = 5.7 \text{ mm}^{-1}$  at 1064 nm [58]; the resulting penetration depth, which accounts for absorption and scattering anisotropies, resulted as  $\delta = 2.52$  mm at 510 nm versus  $\delta = 3.28$  mm at 1064 nm [58].

The sectioning capability arises from the high photon flux required to generate two-photon absorption. Such an intensity is reached only in close proximity to the focal point of the stimulating objective [60].

In fact, the probability  $n$  for a single fluorophore to simultaneously absorb two-photons during a single gaussian pulse can be expressed, as shown in [61] in paraxial approximation, as

$$n \simeq \frac{\delta P_{ave}^2}{\tau_p f_p^2} \left( \frac{\pi \text{NA}^2}{hc\lambda} \right)^2, \quad (1.2)$$

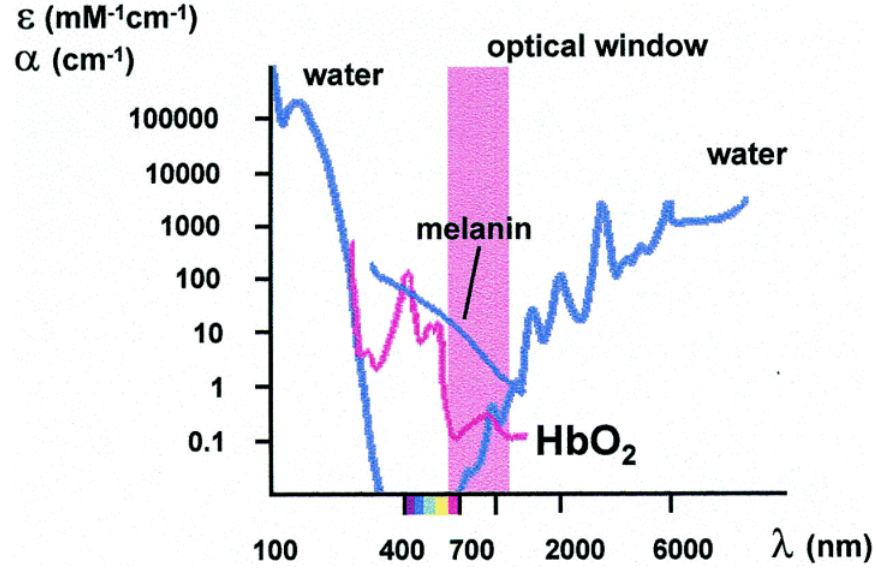


Figure 1.16: The NIR optical window typically employed in biological imaging. Light has a maximum penetration depth where the extinction coefficients of the major absorbers (oxygenated haemoglobin, melanin and water) have a local minimum. The figure shows molecular extinction coefficient for oxygenated haemoglobin and melanin alongside the absorption coefficient of water [59].

where  $\delta$  is the two-photon absorption cross section,  $P_{ave}$  is the average illuminating power,  $\tau_p$  is the pulse length,  $f_p$  is the repetition rate, NA is the Numerical Aperture of the excitation objective,  $h$  is the Planck constant,  $c$  is the speed of light and  $\lambda$  is the illuminating wavelength .

The square dependence over the illuminating power means fluorescence is generated only in a confined volume (fL). This a major advantage over confocal microscopy since it allows the imaging and manipulation of intact specimens in their living conditions with greatly reduced photodamage [50]. Figure 1.17 shows a comparison between stimulation spots in confocal and two-photon stimulation. However, longer excitation wavelengths imply that resolution in two-photon microscopy is slightly worse than in confocal microscopy. This trade-off can be compensated, at the expense of excitation efficiency, by using two-photon excitation in a confocal fashion.

In ideal imaging conditions, the lateral and axial resolution (Rayleigh criterion) for laser scanning two-photon microscopy can be expressed as [62]:

$$r_{x,y} \simeq \frac{0.6\lambda_{exc}}{NA}, \quad r_z \simeq \frac{n\lambda_{exc}}{NA^2}. \quad (1.3)$$



Figure 1.17: A comparison between confocal and two-photon excitation of fluorescence. In confocal stimulation, shown in the upper half of the cuvette, fluorescence from out-of-focus planes is generated at first and then filtered out at the detector. In two-photon stimulation, fluorescence is generated only in a confined volume around the focal position; the two-photon spot is indicated by the arrow.

### 1.5.2 Two-photon microscopy: practical implementation

Two-photon microscopy is usually implemented in a laser scanning microscope. A confocal microscopy setup can also be converted into a two-photon or multiphoton system [63].

Briefly, a laser is focused to a tight spot in the sample plane and raster scanned over a specimen; the beam steps over contiguous scan points separated by a distance known as step size or pixel size. When a fluorescent molecule is illuminated by the scanning focal volume, fluorescent photons are generated and, for a significant part, detected by photodetectors. The signal acquired in each scan point is integrated over a short period of time, known as pixel dwell time (typically a few  $\mu\text{s}$ ), and then mapped to the corresponding position on an intensity image [64].

While significant similarities can be drawn between a confocal and a two-photon setup the latter differs in the excitation source and in the detection strategy. In addition, all optical elements in a multiphoton system should be optimised for NIR light.

#### Light source

As previously mentioned, the low two-photon absorption cross section requires a high-intensity illumination pulse to produce a detectable signal.

Femto-second pulsed laser are the sources of choice, as they allow high peak powers with reasonably low average power, essential for avoiding extensive photodamage of the tissue. As shown in equation 1.2, the two-photon excited fluorescence yield depends on the square of the excitation power. For a pulsed laser with frequency  $f_p$ , pulse width  $\tau_p$  and average power  $P_{ave} = f_p \tau_p P_{peak}$ , the power

function over time  $P(t)$  can be simplified as

$$P(t) = \begin{cases} \frac{P_{ave}}{f_p \tau_p} & \text{if } 0 < t < \tau_p \\ 0 & \text{if } \tau_p < t < 1/f_p \end{cases}. \quad (1.4)$$

Thus, as shown in [65], the time average integral reduces to

$$\frac{1}{T} \int_0^T P(t)^2 dt = \frac{P_{ave}^2}{f_p^2 \tau_p^2} \frac{1}{T} \int_0^T dt = \frac{P_{ave}^2}{f_p \tau_p}. \quad (1.5)$$

A pulsed laser, therefore, allows the same excitation efficiency as a continuous wave laser with an average power that is a factor  $(f_p \tau_p)^{-1/2}$  lower. For example, the same peak intensity can be obtained with 10 W average power from a CW laser or some tens of mW from a typical femtosecond-pulsed laser ( $f_p \sim 100$  MHz,  $\tau_p \sim 100$  fs). Ti:sapphire lasers are near ideal sources for two-photon microscopy.

## Pulse broadening and spherical aberrations

As laser pulses travel through the glass and multilayered dielectric coatings of an optical system, the pulses spread out in time due to Group Velocity Dispersion (GVD). Light in ultrashort pulses actually consists of a range of wavelengths and wavepackets of different wavelengths travel with different speed. The group velocity dispersion gives rise to Group Delay Dispersion (GDD): light from the blue-end of the pulse is delayed with respect to the red-end and the pulse is therefore broadened in time. For this reason having very short pulses might not be ideal: shorter pulses, in fact, house a wider range of wavelengths and are more prone to be broadened. Group Delay Dispersion can significantly affect the excitation efficiency by elongating the pulse in time [66].

Dispersion compensation can be achieved by prechirping the beam through a prism arrangement that gives blue wavelengths a head start and allows different wavelengths to arrive simultaneously at the sample plane [67]. However, the advantages of prechirping must be carefully balanced against power losses and increased alignment complexity [68].

Wavefront distortions, such as spherical aberrations, represent another significant disrupting factor for the excitation efficiency as they hinder the generation of a diffraction limited focal spot. While water immersion objectives are the excitation method of choice to minimise spherical aberrations, the low photo-toxicity of multiphoton microscopy leaves room for increasing the stimulation power, thus compensating the aberration-induced intensity loss, without inducing photodamage [62] [55]. Nonetheless, absolute light levels must be taken into account when imaging in depth. On a converging path, imaging at depth has been improved by the implementation of adaptive optical schemes for wavefront correction [69].

## Scanning system

Galvanometric mirrors are commonly employed in multiphoton microscopy and sit at the heart of the raster scanning of most multiphoton systems. In a galvanometric scanner, the beam is deflected in the x-y plane by a pair of mirrors rotating on perpendicular axis. Mirror positions can be optimised for zooming and image rotation.

However, while having optimal optical properties, galvanometric mirrors are hindered by a relatively slow speed [64] due to intrinsic inertia: faster scanning methods are desirable to acquire images at the neuro-physiological time frame ( $\sim$  ms) and over an imaging field large enough to cover thousands of neurons. A variety of techniques have been developed towards high-speed imaging, amongst them are resonant scanning [70], multifocal excitation systems [71] and acousto-optic deflection [72].

## Excitation

As showed in equation 1.2, two-photon excitation of fluorescence strongly depends on the NA of the exciting objective lens. Since most configurations use a single objective for excitation and detection of fluorescence, the NA is a crucial parameter. Specifically designed objectives for multiphoton microscopy exhibit a high NIR transmittance, an ideally high NA ( $\geq 1$ ) and, typically, moderate to high magnifications ( $\times 40$ ,  $\times 60$ ).

Another key parameter is the objective's working distance, which forces a trade-off between imaging depth and collection efficiency when imaging beyond  $300\ \mu\text{m}$  [62].

The excitation objective in a two-photon microscope is forced to work with wavelengths ranging from the NIR exciting beam to the visible fluorescence. This results in chromatic aberrations since infrared and visible wavelengths are focused in different focal planes. The effect is known as focal plane mismatch: the fluorescence signal is generated in a focal plane, which is not the peak collection plane at that wavelength.

As a consequence, collection efficiency is reduced and fluorescence light is not properly imaged at the back of the objective. While the latter effect might be negligible in non-confocal architectures, the former is a clear drawback.

Approaches to overcome the focal plane mismatch rely on improving the detection efficiency or altering the excitation beam divergence to overlap excitation and emission volumes [62].

## Detection

Since the excitation of fluorescence is confined in a small region around the focus of the objective, multiphoton microscopes do not need to perform any spatial filtering in detection. While descanned detection is feasible and a detection pinhole has a beneficial effect on the lateral resolution, such a

configuration has significant drawbacks in detection efficiency [73]. Positioning the detector/s as close as possible to the objective's back aperture maximizes the collection of fluorescence photons and is a more convenient approach.

Photomultiplier Tubes (PMTs) are widely applied in optical microscopy and constitute the preferred option for detecting multiphoton excited fluorescence [64]. Multifocal setups, which illuminate a sample with a spatial matrix of foci, rely on 2D spatially resolved detectors such as CCDs, arrays of PMT or arrays of avalanche photodiodes [71], to map the detected photons to their conjugate position within the image.

## Chromophores

The presence of a different number of impinging photons implies that different selection rules dominate the transitions involved in one-photon and two-photon excitation [47]. As a consequence, the knowledge of the one-photon absorption spectrum for a particular chromophore allows no quantitative predictions on the two-photon absorption spectrum [55]. As an approximate rule, two-photon absorption spectra tend to be broader and have transition maxima that is shifted to shorter wavelengths than expected from simply doubling the one-photon maxima [64].

As previously mentioned, traditional chromophores have small two-photon cross-sections; nonetheless, significant advances have been made in the engineering of two-photon optimised [74] and photo-activatable proteins [75].

However, in light of the established selection of genetic animal models that employ traditional fluorophores as fluorescent markers, molecules designed for one-photon excitation are commonly used in both *in vivo* and *ex vivo* two-photon imaging studies.

### 1.5.3 Two-photon microscopy in neuroscience

Two-photon microscopy has been instrumental in developing innovative approaches in the life sciences, such as in-depth imaging of live intact tissue, functional imaging of neural populations and intravital optical manipulation [64]. For the purposes of this work, neural imaging of living retinal cells and two-photon optogenetic stimulation are central; however, a brief mention of functional imaging at depth is included to elucidate the potential of the setup described in Chapter 2.

#### Deep imaging

Imaging intact tissues at high resolution and through significant depths is a challenging task, which is ultimately limited by light scattering. Figure 1.16 shows the absorption coefficient of electromagnetic radiation for major intracellular absorbers; water, melanin and oxygenated haemoglobin. It is apparent how near-IR wavelengths are more suited to deep penetration, as they are less prone to scattering than the visible wavelengths employed in single photon microscopy. However, while

imaging at 500 nm has become standard, fluorescence excited near the surface is a limiting factor when targeting depths beyond 5-6 scattering mean free paths [76]. Remarkable penetration depths have been recorded by using slower repetition rates,  $\simeq 1$  mm with 800 nm excitation or by employing longer wavelengths, 1.6 mm in the mouse cortex with 1280 nm excitation [77]. Recently, subcortical imaging has been demonstrated in the living mouse with three-photon excitation of fluorescence at 1675 nm excitation. This promising approach, which allows to reach deeper imaging than two-photon microscopy, required the development of a novel high-pulse energy source employing a photonic crystal pumped by a telecom laser [78].

## Calcium imaging and all-optical readout

The spatial resolution of electrophysiological recordings, even at high-density, is often not suited for defining the type and location of recorded cells. While an innovative method to overcome this issue in the retinal ganglion layer is demonstrated in chapter 4, two photon excitation (TPE) microscopy has been widely employed in calcium imaging studies that have provided valuable insights into the functioning of neural circuits [79]. In fact, as mentioned in section 1.1.1, a variation of extracellular calcium concentration is correlated with spiking activity. As recently reviewed, improvements in optogenetic probes, Genetically Encoded Calcium Indicators (GECI) and microscopy techniques have allowed for all-optical approaches to the manipulation and recording of neural activity in genetically targeted populations [39].

## Two photon optogenetics

The spatial specificity and viability offered by two-photon excitation are desirable features for optogenetic stimulation in intact neural networks. In fact, single opsin molecules can be activated in living cells, at depth, with limited optical cross talk, scattering or tissue heating due to the linear absorption of radiation. Figure 1.18 exemplifies the idea behind two-photon optogenetic stimulation.

However, combining optogenetics with two photon stimulation is not a trivial task, since despite having a relatively high two-photon absorption cross section [38], ChR2 (the most common optogenetic probe) is characterized by a low channel conductance [30]. This means that the requisite number of molecules, which must be recruited to elicit an action potential, barely fit into the femtoliter volumes activated by two-photon stimulation. Very high expression densities are not an option since they might be detrimental for cellular health.

This problem has been overcome by enlarging the stimulation volume in order to spatiotemporally integrate photoactivated currents. Seminal work has achieved two-photon optogenetic stimulation by scanning a decreased-NA IR laser beam over the cell somata in a raster or spiral fashion. Spiral scans of  $\sim 30$  ms at 920 nm have proved effective in eliciting action potentials in tissue cultured

neurons, as shown in figure 1.19 [38].

Later approaches have employed patterned illumination to achieve two-photon optogenetics with short stimulation times (5 ms) [80] and, ultimately, scanless stimulation of multiple sites [81]. Patterned approaches split the laser power among excitation sites and so the available power might limit the number of addressable neurons. The development of red-shifted opsins with higher channel conductance and longer off-kinetic [82] has allowed significant advances in the field which, in combination with functional imaging performed on genetically encoded calcium indicators, has achieved remarkable results (e.g. two-photon optogenetics on dendritic spines [83]). Novel opsins and innovative combination of established optical techniques have led to promising all-optical approaches to the investigation of neural circuitry [84, 85]. However, while offering unprecedented control with minimal invasiveness, imaging-based read-out techniques still lack the high-temporal resolution provided by electrophysiology techniques.

The endeavour of the present work is rooted on the shared belief [39] that fruitful insights in future investigations of neural networks will arise from combinations of electrophysiological approaches and optical interfacing.

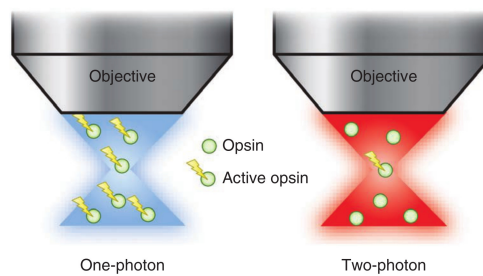


Figure 1.18: A simplified comparison between one-photon and two-photon optogenetic illumination strategies. While single-photon optogenetic stimulation excites all cells in the target volume, two-photon optogenetic stimulation allows to select a single transfected cell with 3D resolution. Adapted from [34].

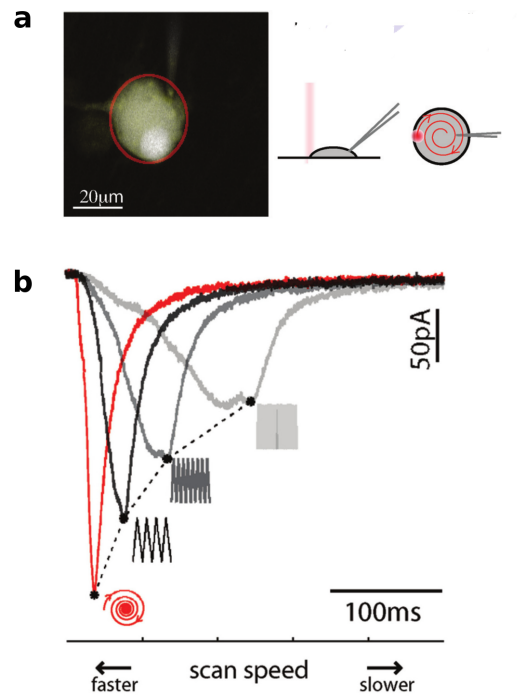


Figure 1.19: Scanning approaches to two-photon optogenetic stimulation. (a) *Left*, an image of a ChR2 transfected cell; *right*, a diagram of the spiral scan concept: action potential are elicited by spiral scanning an IR laser beam on the ChR2-transfected cell soma. (b) A comparison of scanning strategies in the excitation of action potential. The spiral scan, lasting for 16 ms at an illumination intensity of  $I=2.5 \times 10^{54}$  photons<sup>2</sup>/cm<sup>4</sup>s<sup>2</sup>, yields larger action potentials. Adapted from [38].

## Chapter 2

# A setup for two-photon microscopy, optogenetics and MEA recordings

### 2.1 Overview of the system

As discussed in the previous chapter, to advance our understanding of neural networks will require new and innovative experimental tools. For a complete investigation of neural networks, a tool is required that can detect electrical activity, modify this activity and image the neural network. This tool must have the ability to interface with hundreds of neurons with high spatio-temporal precision and single cell selectivity. No single current technology can accomplish all these tasks. However, a synergic approach combining high-density electrophysiological recordings, two-photon microscopy and optogenetic stimulation has the potential to open a new frontier in our understanding of neural circuitry [39].

This chapter reports on the construction and validation of an experimental tool, which combines a two-photon microscope, a  $\mu$ LED array optogenetic stimulation setup and a high-density micro-electrode array (MEA). An image of the system is shown in Figure 2.1. The system is based on an inverted microscope (Nikon).

### 2.2 Optogenetic stimulation system based on a $\mu$ LED array

An optical system has been assembled to integrate high-density electrophysiological recordings with spatio-temporal optogenetic stimulation. This setup meets the crucial requirements for optogenetic experiments: efficient light delivery and high-resolution read-out. The system consists of a high-density MEA, which can simultaneously record single action potentials from hundreds of

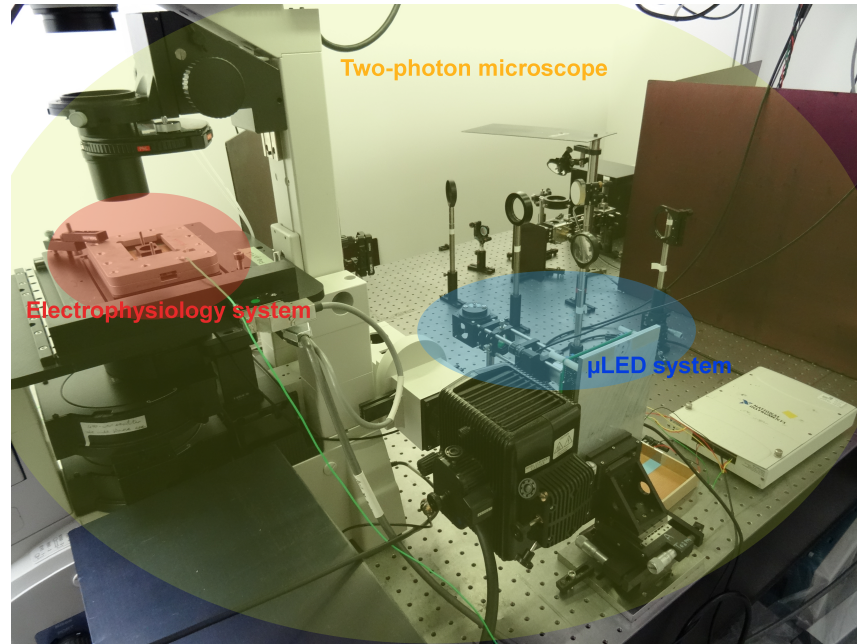


Figure 2.1: Image of the experimental setup. The two photon microscope, shaded in yellow, is integrated with the  $\mu$ LED optogenetic stimulation setup, shaded in blue, and the micro-electrode array electrophysiology system, shaded in red.

cells, combined with an array of individually addressable  $\mu$ LED light sources, which can stimulate genetically targeted cells. Previous work has demonstrated that  $\mu$ LED arrays can elicit action potentials in neural soma or neural processes [42] Optogenetic stimulation experiments performed with the  $\mu$ LED array are covered in Chapter 4.

### 2.2.1 Projection system

The  $\mu$ LED array [43] is composed of  $16 \times 16$  blue (450 nm) LED sources, each source is sized  $100 \mu\text{m} \times 100 \mu\text{m}$ . The light from the  $\mu$ LED array was projected into neural tissue mounted on the transparent MEA. Stimulation patterns selected on the  $\mu$ LED array were imaged above the electrodes plane of the MEA through a  $4f$ - relay system, shown in figure 2.3. A conceptual diagram of the projection system is presented in figure 2.2.

The  $\mu$ LED projection system was integrated with the inverted microscope via the lower illumination path of the microscope frame, typically employed for brightfield illumination. This choice imposed design constraints to avoid vignetting effects while maximizing the number of pixel imaged on the MEA. Moreover, in order to maintain brightfield imaging capabilities, the projection system relied on an external cage support which gave the possibility to insert and remove the illumination optics set in the fluorescence arm.

The optical train was arranged in order to accommodate the diagonal dimension of the  $\mu$ LED array,  $\sim 1.6 \text{ mm}$ , in the objective back aperture. LED light was collected with an infinity-corrected  $\times 4$  objective (working distance 17.2 mm, NA 0.13) and relayed to the back of a  $\times 20$  infinity-corrected

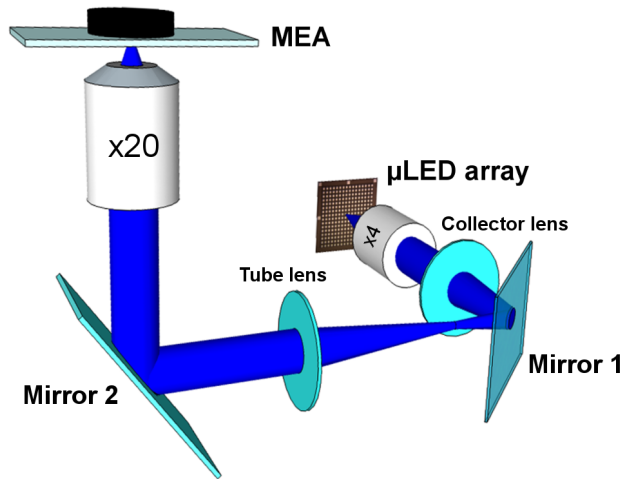


Figure 2.2: Schematic of the optical system used to project  $\mu$ LED. Light from LED sources is collected with a  $\times 4$  objective and relayed to the electrode's plane using a  $\times 20$  excitation objective. objective (WD 2.1 mm, NA 0.5) with a pair of conjugated lenses (focals  $f_T = 250$  mm,  $f_C = 150$  mm). As a result,  $\mu$ LED were optically demagnified to  $\sim 20 \times 20 \mu\text{m}^2$ . While figure 2.3 shows patterns of  $\mu$ LED projected on the MEA, a photograph of the projection system is displayed in figure 2.4. The collection efficiency was estimated assuming an ideal lambertian emission for the LED sources. Considering 15 degrees of acceptance for the objective, the collection efficiency is 1 %. The efficiency of the rest of the optical train was measured as the ratio between the collected intensity at the back of the  $\times 4$  objective and the projected power at focus of the  $\times 20$  objective. This yielded an efficiency estimation of  $\sim 80\%$ . The total efficiency of the projection system is therefore  $\sim 0.8\%$ . Future investigation will find benefit in a direct measurement of the power emitted by the  $\mu$ LED array.

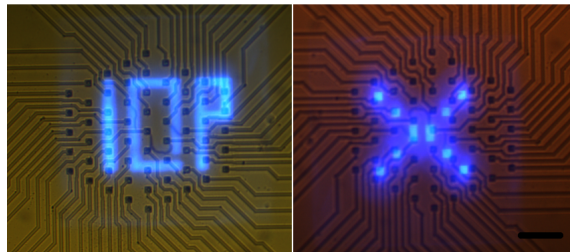


Figure 2.3: Images of  $\mu$ LED patterns focused on the 61 electrodes MEA. Scale bar is 120  $\mu\text{m}$ .

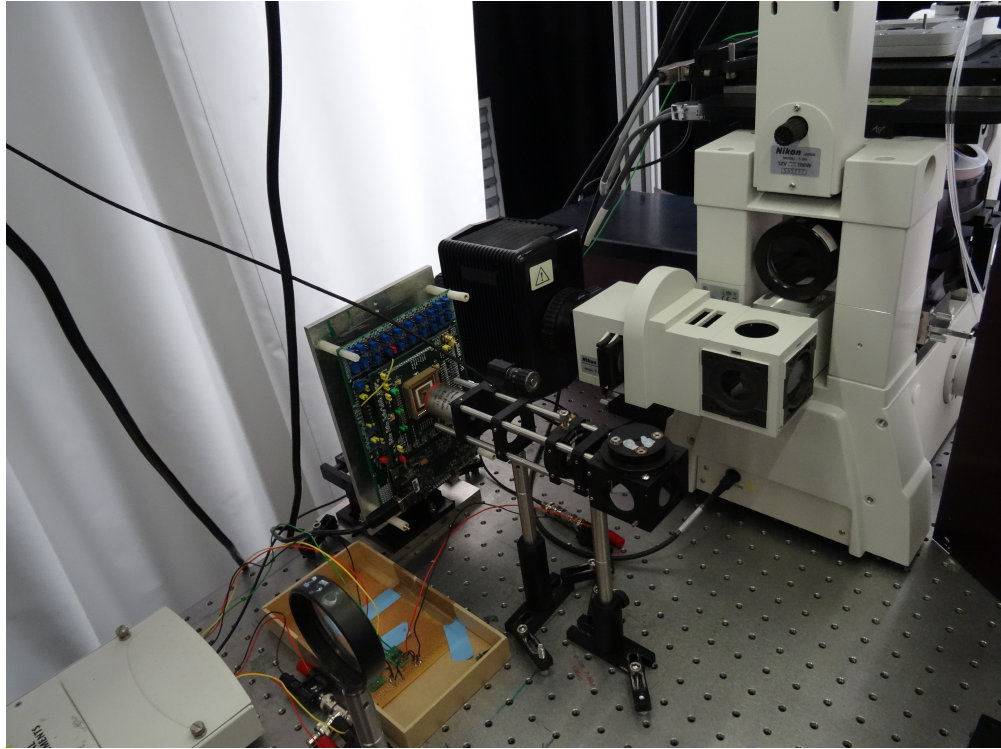


Figure 2.4: The figure shows a detail of the 4f-relay system used to project light from  $\mu$ LED array to the MEA.

### 2.2.2 Power modulation and pattern control

Control on spatio-temporal stimulation patterns and stimulating intensities was achieved via a custom LabView software [86], interfaced with the  $\mu$ LED control software. Optogenetic stimulation protocols have been designed as repeating flashes of an arbitrary pattern of multiple pixels, e.g. figure 2.3, or random sequences of single pixels.  $\mu$ LEDs timing was controlled with a master TTL trigger signal (2-20 Hz).

The emitted power was adjusted by modulating the duty cycle of a second TTL pulse which was convoluted with the master trigger. A third voltage signal was used as a reference to scale the voltage control from 5V (TTL) to 3.3 V (CMOS). The convolution of voltage controls, exemplified in figure 2.5, was performed with a dedicated electronic circuit based on hexagonal buffers. The emitted intensity at the focal point of the  $\times 20$  objective was  $50 \frac{\text{mW}}{\text{mm}^2}$ , significantly above the stimulation threshold for optogenetic experiments  $1-5 \frac{\text{mW}}{\text{mm}^2}$  [7].

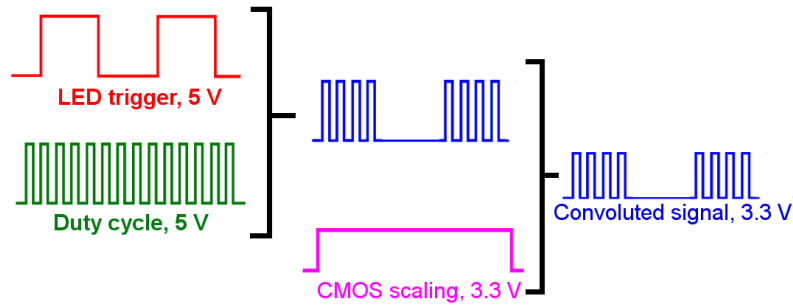


Figure 2.5: Schematic of the signal convolution for  $\mu$ LED power control. A slow TTL signal ( $\sim 10$  Hz ) controlling the stimulus timing was convoluted with a fast signal (50 KHz) that controlled the duty cycle. The resulting signal, in blue, was then scaled to 3.3 V to comply with the LED driver.

## 2.3 Two-photon microscope

A two-photon microscope was designed and assembled around the electrophysiology and optogenetic systems. The microscope allows for the imaging of live cells during optogenetic stimulation and electrical recording. This section reports on the microscope’s optical architecture, software control and validation.

### 2.3.1 Microscope architecture

#### Schematic of the optical path

Figure 2.6 shows the schematic of the microscope’s optical path. Briefly, a femtosecond pulsed laser beam was scanned with a pair of galvanometric mirrors conjugated in a 4f system. A keplerian beam expander was then used to enlarge the laser beam before relaying it to the back of the  $\times 20$  objective with a second 4f relay system. The following paragraphs describe the microscope in detail while referring to the numbers outlined in figure 2.6.

#### Laser source

Femto-second pulsed lasers are the sources of choice for two-photon microscopy since they express high-peak powers with a reasonably low average power [87]. This microscope employed a mode-locked, Ti:sapphire Mai-Tai laser from Spectra-Physics. The laser has a declared pulse width of less than 100 fs and a repetition frequency of 80 MHz. The tuning range spans from 690 to 1020 nm with maximum average power greater than 2.5 W at 800 nm, corresponding to a peak power greater than 310 kW. At 920 nm the oscillator nominally provides more than 1.35 W average power and 165 kW peak power [88]. The tuning curve is shown in figure 2.7. Laser power was modulated with a polarizer positioned in front of the beam output. The size of the laser beam was measured

using a knife edge technique [89]. The beam waist was estimated as  $w=0.8 \pm 0.1$  mm, as shown in figure 2.8.

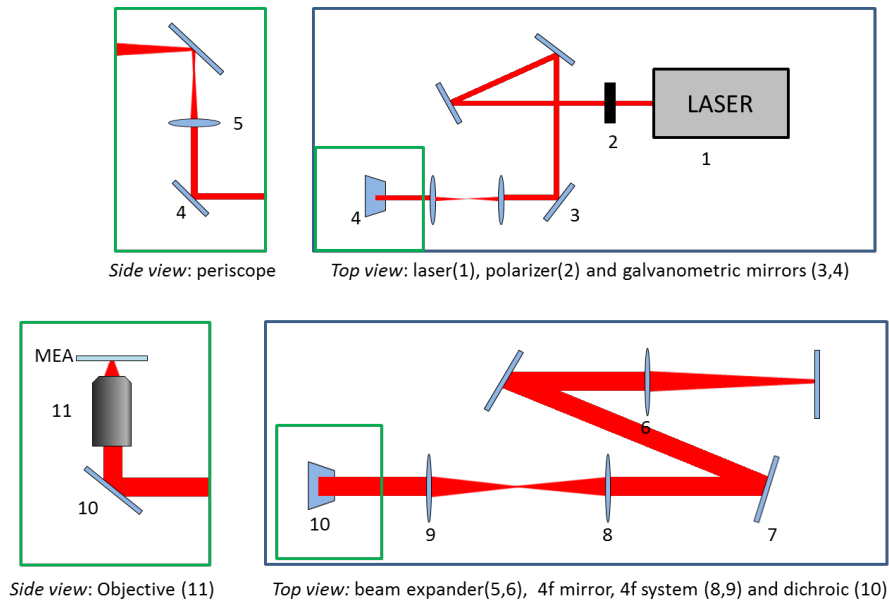


Figure 2.6: The figure shows the optical path of the laser beam in the two-photon microscope. At the laser output (1), the beam power is modulated with a polarizer (2). The beam is then deflected by a pair of galvanometric mirrors (3 and 4) and enlarged with a beam expander (5 and 6). The enlarged beam is then relayed with a 4f relay system (8 and 9) to the back of the objective after reflecting off a dichroic mirror (10). The 4f system provides for additional expansion of the beam. Finally, the beam enters the objective (11) and gets focused above the MEA top surface.

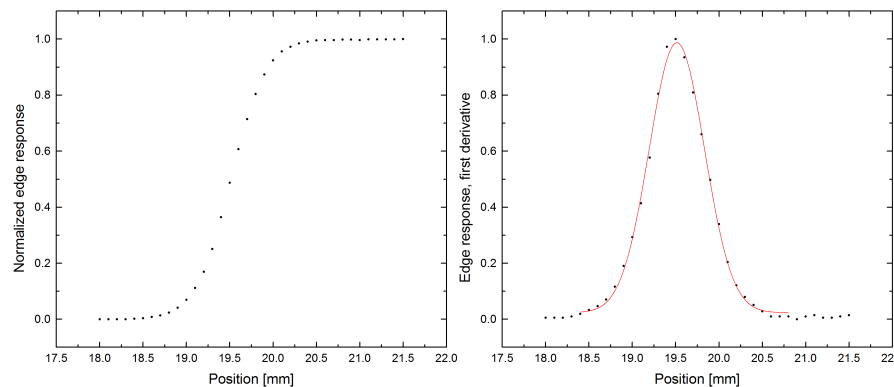


Figure 2.8: Left panel shows the normalized edge response, in power, as measured by scanning the beam across a sharp edge. Right panel shows the first derivative of the edge response with a gaussian fit. Parameters for the gaussian fit were  $x_{centre} = 19.5 \pm 0.1$  mm, amplitude= $0.77 \pm 0.01$  mm,  $\sigma = 0.32 \pm 0.01$  mm, reduced  $\chi^2 = 4 \times 10^{-4}$ . The fit yield a FWHM of  $0.75 \pm 0.01$  mm.

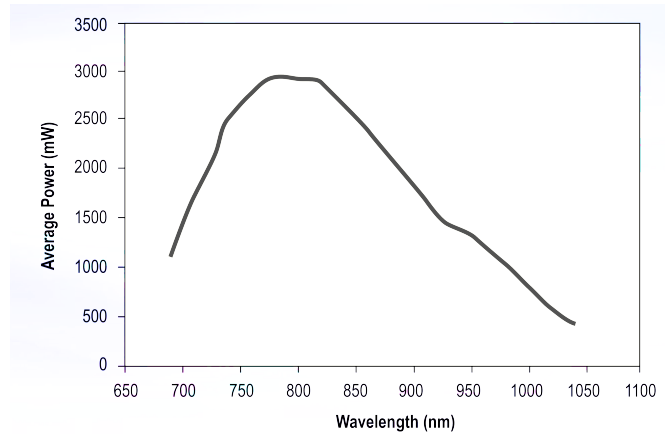


Figure 2.7: The figure shown the tuning curve for Mai-Tai HP laser [88].

### Scanning system

The scanning system consisted of two standard galvanometric mirrors (Cambridge Technology) oriented on perpendicular axis and positioned at the focal points of a 4f system. The mirrors were driven by a digital and an analog actuators, controlled via LabView software (see software control section 2.3.2). Scanning bandwidth was limited to a few kHz with the faster servo driver (Position Pro 2 TM 800) regulated by a 10  $\mu$ s clock [90]. Figure 2.9 shows a detail of the scan system.

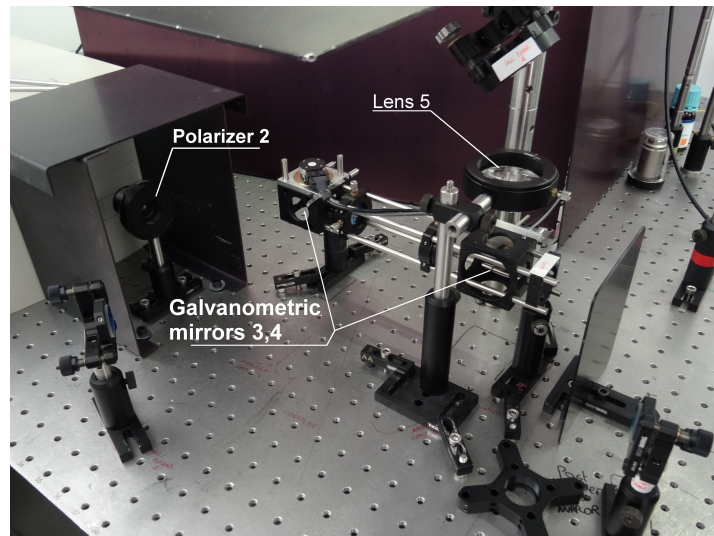


Figure 2.9: The laser output, attenuated with a polarizer, is directed to a pair of x-y galvanometric mirrors. The mirrors are reciprocally conjugated with a 4f relay system.

### Beam expander and optical relay system

In order to fill the back aperture of the objective and exploit its full NA [62], a beam expander was inserted after the scanning system. The back aperture of the main objective employed (Nikon  $\times 20$  PlanFluo) is 10 mm in diameter. The beam waist at the laser output was approximately 1 mm. A

magnification factor of  $\sim 10$  was therefore needed. A first step of  $\times 8$  magnification was performed with a Keplerian beam expander made of two 50 mm lenses. These two lenses, indicated as 5 and 6 in figure 2.10, had focal lengths  $f_5 = 100$  mm and  $f_6 = 800$  mm. The Keplerian beam expander conjugated the second galvanometric mirror with a reflector (7 in figure 2.6 and figure 2.10) which was optically relayed to the back of the objective via a 4f relay system. This system was made of two additional lenses working as scan and tube lenses (8 and 9 in figure 2.6 and figure 2.11). These two last lenses provided for an additional step of  $\sim 1.3$  magnification having focal lengths  $f_8 = 225$  mm and  $f_9 = 300$  mm. Laser light was then directed to the back of the objective with a short pass dichroic mirror (DMSP805R, Thorlabs) mounted in position 10 in figure 2.6. Spectral transmissivity of the mirror is shown in figure 2.12.

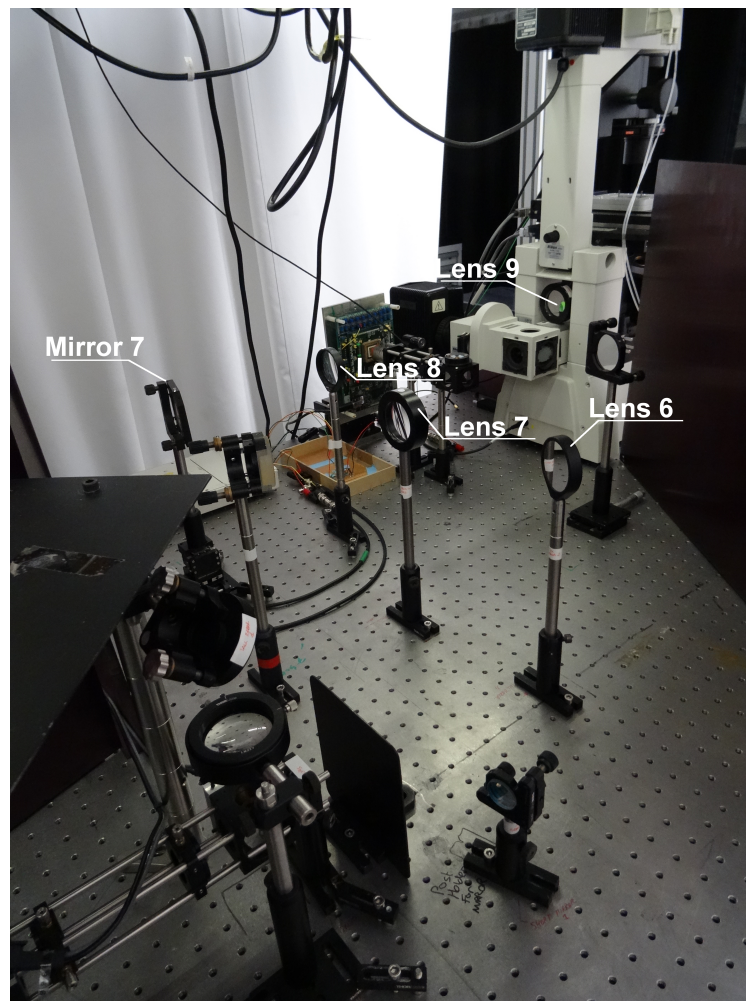


Figure 2.10: The laser, after being deflected in the scanning system, is enlarged with a Keplerian beam expander: lenses 5 and 6.

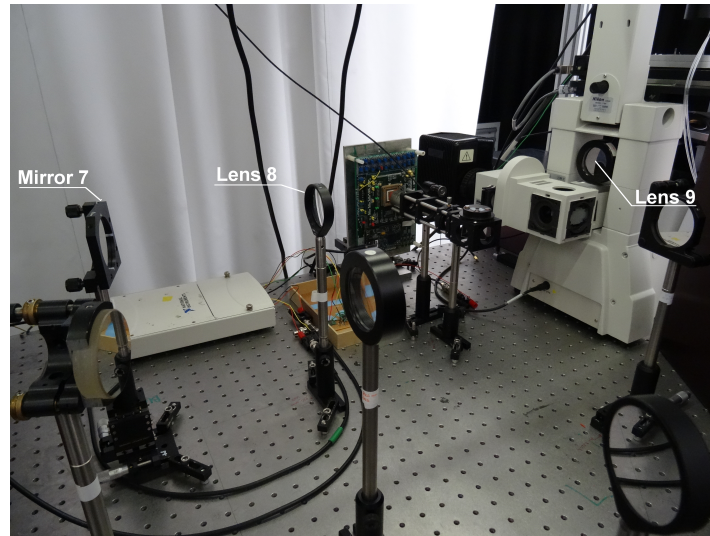


Figure 2.11: After the beam expander, the laser spot is relayed at the back of the objective with a final 4f system: lenses 8 and 9.

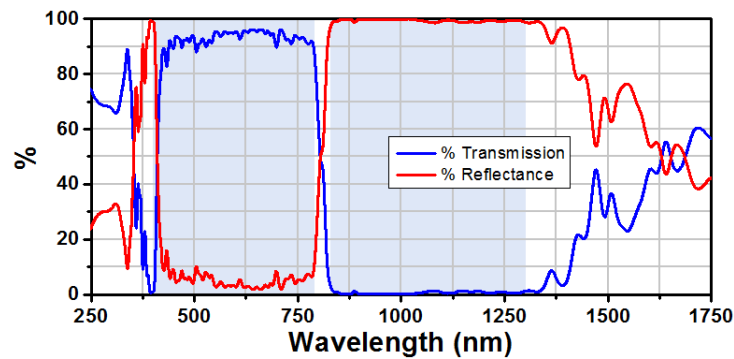


Figure 2.12: Transmittance and reflectance versus wavelength for short pass dichroic DMSP805R from Thorlabs. The NIR laser beam is reflected to the objective while the visible fluorescence is transmitted to the detectors.

### Planar and axial scanning with piezo-electric actuators

The theoretical field of view achievable with the described system can be estimated following the calculation outlined by Young et al [91]. The limit on the maximum scan angle can be inferred from the maximum displacement allowed on the 50 mm lenses employed in the beam expander. Considering the expanded beam is  $\sim 10$  mm in diameter, the maximum displacement from the centre of lens 6, which receives from the longest focal distance, is 15 mm ( it is worth noting that the laser beam is scanned over a square area). This constraint implies that the maximum scan angle at the back of the objective is  $\Theta_{max} \sim 0.028$ . The field of view for a  $\times 20$  objective with focal length  $f_0 = 10$  mm is therefore  $FOV = 2f_0\Theta_{max} = 560 \mu\text{m}$ .

The calculated FOV has not been exploited in its fullness as an alternative approach has been pre-

ferred, in light of the integration with the electrophysiology setup. As covered in the next chapter, the interaction of the laser beam with the MEA electrodes produces large electrical artifacts which interfere with spike detection and spike sorting. While it has been possible to successfully perform neuron identification in presence of laser scanning, large laser-induced artifacts prevented spike-detection in the artifact-affected time window. In order to minimise (or avoid in the best hypothesis) the electrode exposure to the laser beam, a scanning protocol has been developed where image tiles around a single electrode (e.g. squares of 60  $\mu\text{m}$  side) are acquired in adjacent positions and then automatically stitched off-line [92]. This method has been implemented using a piezo stage (ASI 2000 XY) controlled via LabView. Advantages and drawbacks of this approach will be further elaborated in the discussion section.

3D imaging was performed with a piezo-electric vertical positioner (PI E-665 Z), mounted under the objective. 3D images were generated acquiring planar images at progressive focal depths. The position of the axial focal plane was controlled via LabView software and images were stitched off-line with a custom macro extending existing ImageJ software. Volume rendering was obtained with the ImageJ-Volume viewer plugin.

### Imaging objectives

The microscope has been designed to image retinal tissue mounted on a MEA, fabricated on a 1.1 mm thick glass substrate with refractive index 1.5. During electrophysiological recordings, the retina is pressed on the MEA and retained by a plug. The plug is inserted in a plastic chamber glued on the top of the array to contain physiological solution. The plug system, which is described in Appendix A, prevents imaging from above the MEA. Imaging, therefore, has to be done through the glass substrate. Epi-fluorescence brightfield imaging is not particularly affected by this arrangement, but the thickness of the glass substrate imposes a trade-off in the choice of the lens for two-photon imaging. In fact, the employed objective lens must (a) have a working distance  $>1.1 \times 1.5$  mm to reach the retinal tissue mounted on the MEA and (b) must be designed to work in air.

Typically, dry objectives with long working distance have moderate NA and moderate magnification. While moderate magnification might be advantageous for a large field of view, the strong dependence of two-photon excitation on the objective's NA means that a moderate NA will translate to lower excitation efficiency [62]. Commercial options for lenses with high NA and long working distance do exist but are very expensive. To comply with these design constraints, the microscope was equipped with a Nikon PlanFluor  $\times 20$  objective, 2.1 mm working distance and 0.5 NA. As the objective is designed to work with 0.17 mm thick coverslips, spherical aberrations are expected when imaging through the MEA.

The order of magnitude of the expected photon flux for two-photon excitation of fluorescence of a single molecule can be calculated multiplying the probability of two-photon absorption in a single

pulse times the laser repetition rate [61]. Using the probability of two-photon absorption  $n_a$  in a single molecule

$$n_a \simeq \frac{\delta_2 P_{ave}^2}{\tau_p f_p^2} \left( \frac{\pi NA^2}{hc\lambda} \right)^2, \quad (2.1)$$

the expected rate of excited photons becomes:

$$\text{photons } s^{-1} \simeq n_a f_p \simeq \frac{\delta_2 P_{ave}^2}{\tau_p f_p} \left( \frac{\pi NA^2}{hc\lambda} \right)^2. \quad (2.2)$$

This, with  $P=10$  mW,  $\tau_p=100$  fs,  $f_p=80$  MHz,  $\lambda=920$  nm and  $NA=0.5$ , yields

$$\text{photons } s^{-1} = 2.8 \times 10^5. \quad (2.3)$$

It has been estimated, from the emission profile shown in reference [53], that the two-photon cross section for eYFP at 920 nm has half the peak absorption cross section at 960 nm. Excitation was usually performed at 920 nm because the laser was not as stable at longer wavelengths.

Benchmark values obtained by Diaspro et al. [87] with the same excitation power and a 1.4 NA objective are  $3 \times 10^7$  photons  $s^{-1}$ , two orders of magnitude larger than the calculated photon excitation rate. Even taking into account the different parameters used in the benchmark measurement (780 nm illumination, 38 GM cross section, 100 MHz repetition rate), the lower NA appears to be responsible for a major part of the excitation efficiency reduction ( $\sim 60\%$ ). The generation of images with good SNR has required illuminating powers higher than the ones generally employed in two-photon microscopy, e.g. 1 to 10 mW [61]. In addition to the aforementioned  $\times 20$  objective, a Nikon Plan Fluor  $\times 100$ , 1.3 NA oil-immersion objective has also been employed and characterized to assess the microscope performance with a higher NA. Having a working distance of 0.16 mm, this objective is not suitable for imaging through the MEA. However, imaging retinal tissue once removed from the MEA might be a useful asset which has been considered worth pursuing.

### Detection of fluorescence

The microscope has been equipped with CCD cameras and a PMT. Two CCD cameras have been employed for brightfield epifluorescence imaging: a Teledyne Dalsa Genie  $640 \times 480$  pixels ( $9.9 \mu\text{m} \times 9.9 \mu\text{m}$ ) and a air-cooled color QICAM from QImaging,  $1392 \times 1040$  pixels ( $4.65 \mu\text{m} \times 4.65 \mu\text{m}$ ). Spectral sensitivities for the two cameras are shown in figure 2.13. The Teledyne Dalsa was integrated with the LabView control software and controlled within the main microscope GUI. Two-photon imaging was performed with a PMM02 PMT from Thorlabs mounted in non-descanned mode to increase collection efficiency. The PMT was shielded from stray light and operated in the  $10^5/10^6$  gain region via a voltage gain control. PMT readout was performed within the microscope control software, as described in the next section, at 1 MHz rate. The spectral sensitivity of the

PMT is shown in figure 2.14. Before reaching the PMT, reflected laser light pump was blocked with a 5 mm thick filter (C3C-23 glass) positioned in front of the detectors. Transmittance properties of this filter are shown in figure 2.15.

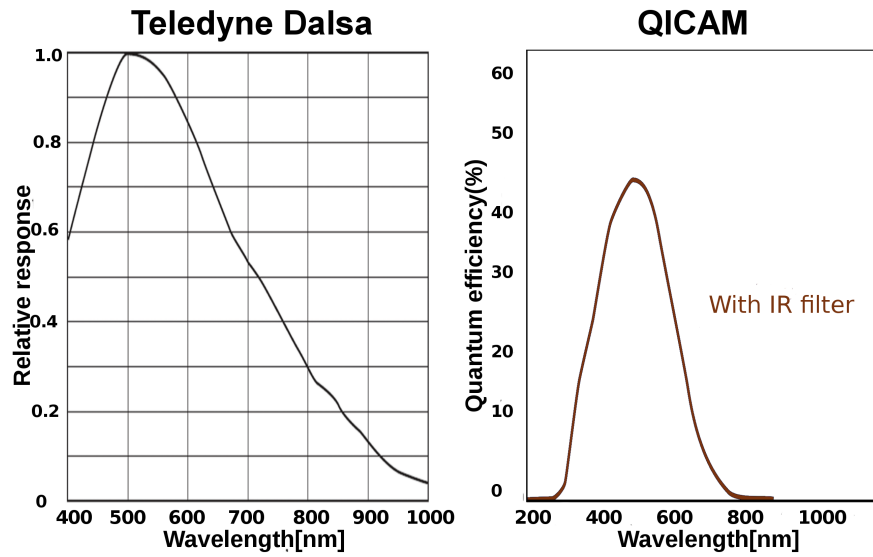


Figure 2.13: Spectral sensitivity of CCD cameras. *Left*, Teledyne Dalsa Genie CCD; *right*, QICAM CCD. Provided by manufacturers.

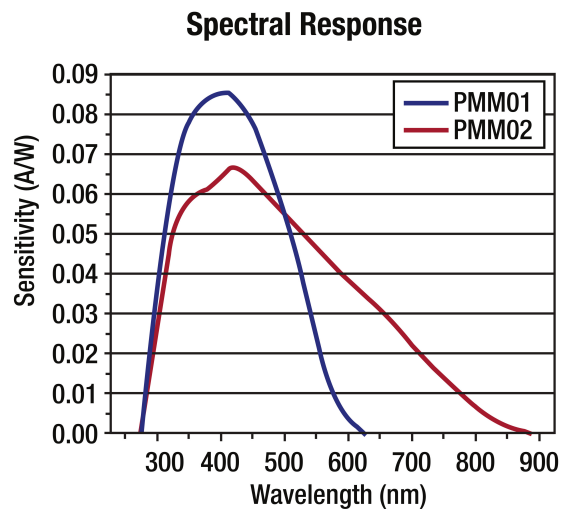


Figure 2.14: Spectral sensitivity of PMM02 PMT from Thorlabs.

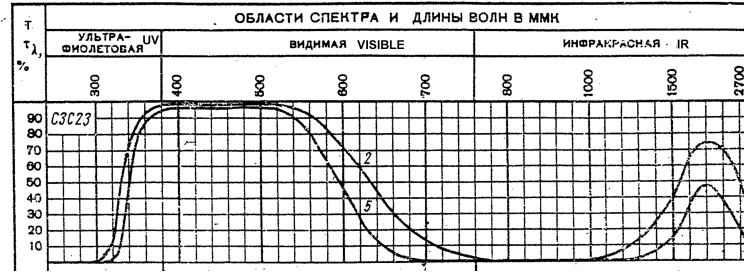


Figure 2.15: The figure shows transmittance versus wavelength for 2, top line, and 5 mm, bottom line, thick C3C-23 glass optical filter. Wavelengths in nm are indicated above the plots, divided in UV, Visible and IR regions. The english translation is inserted besides the original label.

### 2.3.2 Software control and image acquisition

The control software for the two-photon microscope was developed in LabView. A custom developed software was preferred to existing open-source alternatives for laser scanning two-photon microscopy [93, 94] because it allowed imaging protocols to be adapted to the unique problems in this system.

The principles of operation of the control software are exemplified in figure 2.16. The PC was connected to a USB-6259 NI board whose analog outputs communicated with the galvanometric mirrors drivers; the PMT signal was read via an analog input on the same board. Serial ports were used (through serial to USB adaptors in cases) to control the laser shutter, the X-Y stage and the axial piezoelectric actuator. Controls for the Teledyne Dalsa CCD camera have been incorporated in the software via Ethernet connection; as mentioned, the QICAM CCD was used with a proprietary software.

The control software loads user-defined scan parameters which determine the area and depth to be scanned, pixel dwell time, scaling of the PMT signal and saving options to store images. The GUI interface is shown in figure 2.17. The pixel size is fixed, in order to guarantee a spatial sampling of  $\sim 4$ -5 Nyquist frequency. Lateral scans are organized in adjacent and overlapping tiles, as shown in figure 2.16-d, whose area is fixed to  $60 \times 60 \mu\text{m}^2$  for the  $\times 20$  objective; tile overlap is fixed to 10 % by controlling the position of the XY stage. The number of tiles needed to cover a predetermined area is calculated by the scanning algorithm.

After loading the scan parameters, the software generates the analog voltage waveforms to drive the galvanometric mirrors, as presented in figure 2.16-c. Raster scans are performed by quickly moving one of the mirrors across a 1 V voltage range whilst the second mirror is stationary; this process is repeated until the stationary mirror has spanned a 1 V deflection. In order to minimise exposure of the tissue to the laser beam, the shutter was set open only for the duration of the scan. After each scan, the X-Y stage was re-positioned; in case of a 3D scan, the Z focus was moved at the completion of a plane.

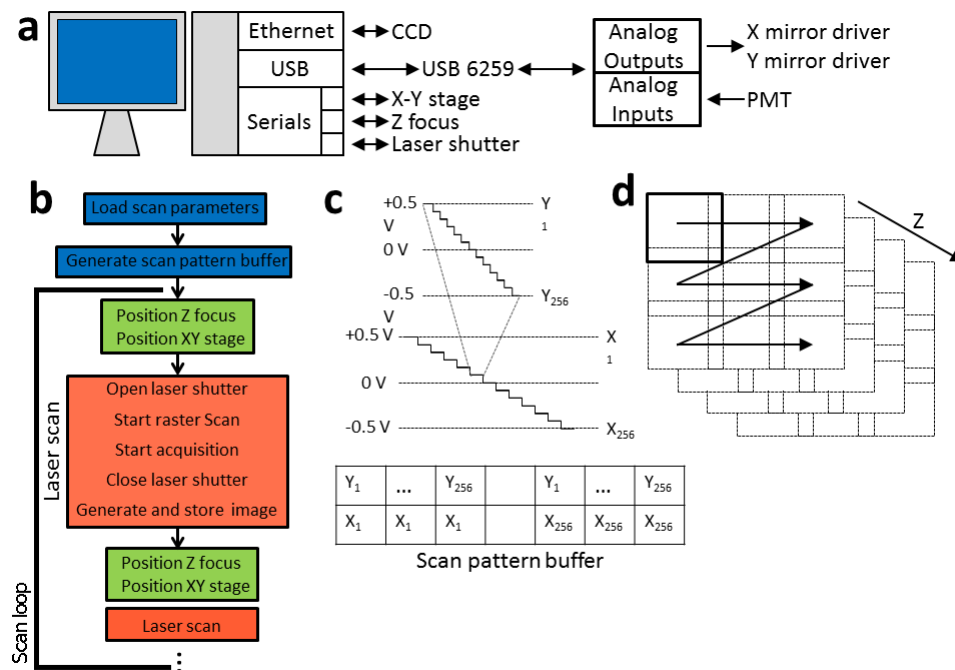


Figure 2.16: Principles of operation of the control software. (a) A diagram showing the devices used and their connections. (b) The flow chart of the control program. (c) A detail on the voltage waveforms sent to the galvo drivers to control the scan. For each step on the x axis, a fast scan on the y axis was performed. The bottom panel shows a table of the voltages sent to X and Y galvos during the scan. Galvo scanning and PMT acquisition were synchronised at the start of the scan with a trigger signal; this signal was refreshed every 4 scan lines. (d) The adopted protocol for planar and axial scanning. Partially overlaying square tiles were acquired for each plane. Then, the piezo stepper on which the objective was mounted was moved along the axial dimension to acquire a new plane.

The actual displacement of the laser spot on the sample plane was monitored with a calibration routine that calculated the  $\mu\text{m}/\text{V}$  response of both galvanometric mirrors. Briefly, the beam was focused on a fluorescent slide and the generated fluorescence was captured on the CCD camera. The CCD camera is a spatially resolved detector so the position of the fluorescent peaks yields information on the position of the excitation spot on the sample plane. Knowing the CCD pixel to  $\mu\text{m}$  calibration (see section 2.4),  $\mu\text{m}/\text{V}$  response can be inferred by calculating the position of the fluorescent peak in terms of CCD pixels for the mirror's maximal displacement. As shown in figure 2.17, the GUI allows for the automation of this process. Since variation in calibration values did not significantly differ from the reference value of  $60 \mu\text{m}/\text{V}$ , scanning routines were often performed with this parameter set. The lateral calibration of the microscope was independently crosschecked imaging fluorescent beads of known diameter, as detailed in the following section. Images were produced by acquiring the fluorescence generated in small, contiguous area (pixels) with a PMT. Mirror scan and data acquisition were synchronised using an internal clock signal

of the DAQ board as a digital trigger. Raw signals from the PMT were sampled at 1 MHz and averaged over 50-100  $\mu\text{s}$  time intervals (pixel dwell times). In order to improve execution speed, the software allows for several line scans to be acquired between two consecutive clock triggers. Once acquired and averaged, the data was arranged in arrays of  $256 \times 256$  elements, converted to 8-bit images and stored for off-line analysis. Following the approach described in [94], data acquired at the extremes of each line scan, when the mirror are turning around, was discarded. Experience suggested how the scanning routine can be improved allowing a longer flying-back time in the analog waveform supplied to the galvos. Moreover, it has been observed how relatively short pixel dwell times (10-30  $\mu\text{s}$ ) resulted in aliasing effect on the voltage waveform sampling by galvanometric mirror drivers: this undesired effect has been balanced using longer pixel dwell times (50-100  $\mu\text{s}$ ). As shown in figure 2.17, the front panel has been equipped for instantaneous display of the acquired images. However, this add-in was found to impair the scan speed and was rarely activated.

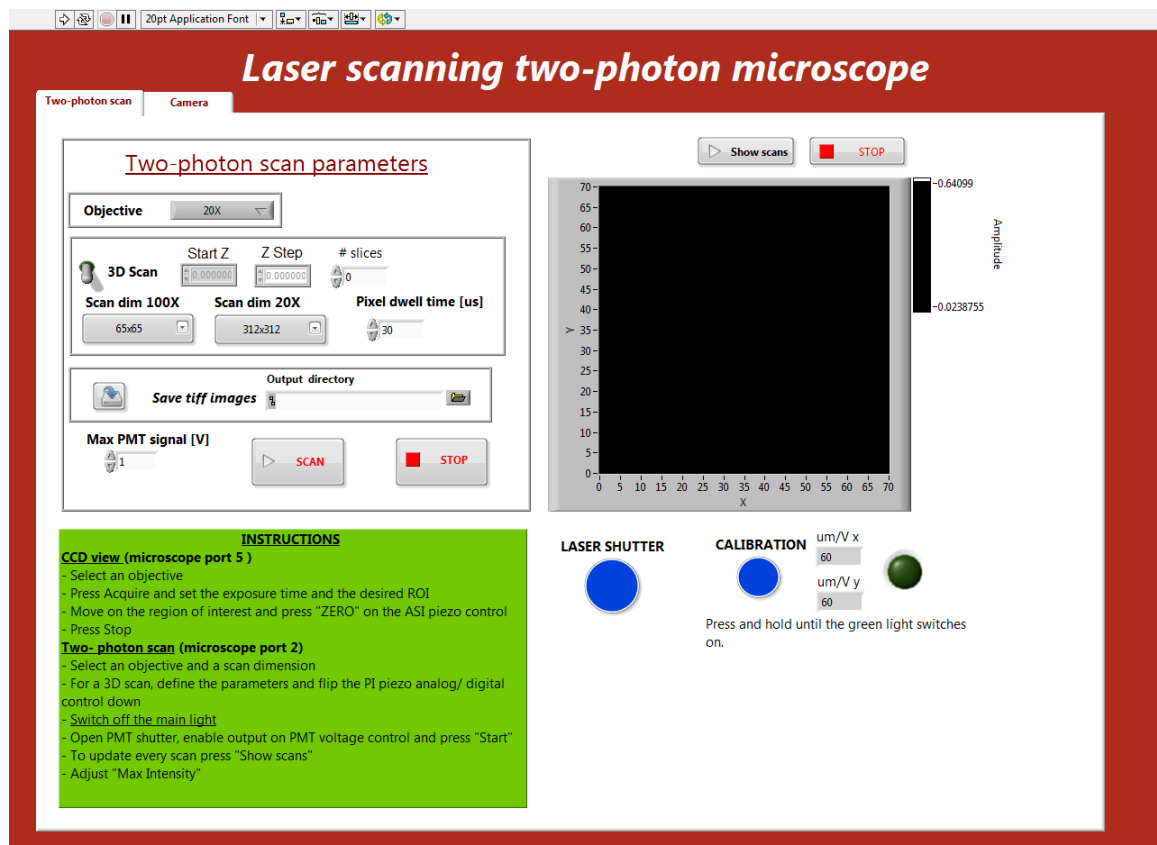


Figure 2.17: GUI for the two-photon laser scanning microscope software control

## 2.4 Characterisation of the two-photon microscope

The microscope was characterised by imaging calibration samples including fluorescent slides, fluorescent micro-spheres (beads) and resolution charts.

### 2.4.1 Excitation of fluorescence

Two-photon excitation of fluorescence has a quadratic dependence on laser intensity. This was checked to confirm the microscope is operating in a two-photon condition. The sample used was a green fluorescent slide (Chroma Technology) excited at 920 nm with a  $\times 20$  objective. Fluorescent yield was calculated as the average value of the pixel in an image scan; uncertainty was estimated as the standard deviation of the pixel values. The quadratic dependence of two-photon excited fluorescence against the excitation power is shown in figure 2.18.

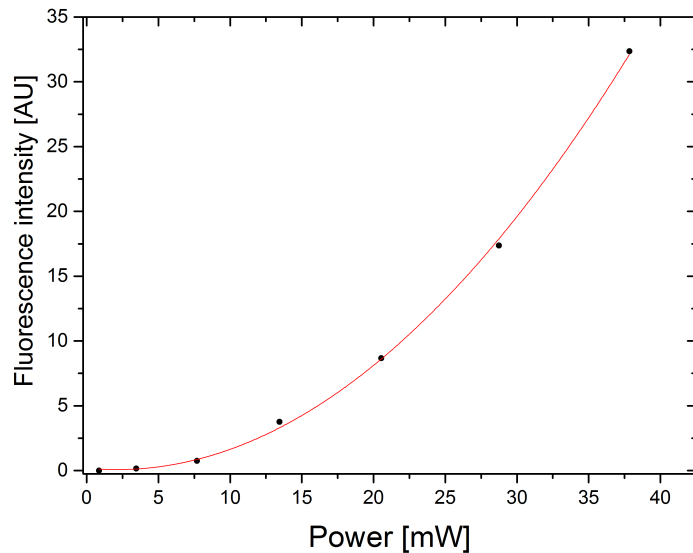


Figure 2.18: Quadratic dependence of fluorescence intensity on illuminating power compared with the expected quadratic dependence.

### 2.4.2 Optical resolution

The optical resolution of the microscope was characterized by measuring the intensity Point Spread Function (PSF) for two photon excitation of fluorescence. Measuring the intensity PSF is a common method for the characterisation of a microscope system since it conveys information on lateral and axial resolution and, ultimately, on the intrinsic optical sectioning capabilities [61]. PSFs were measured by imaging sub-resolution green fluorescent nano-spheres (505 exc./515 em., 0.18  $\mu\text{m}$  in diameter, PS-Speck from Molecular Probes) with a  $\times 20$ , 0.5 NA and a  $\times 100$ , 1.3 NA oil-immersion

Nikon objectives. Laser scans were performed at 920 nm.

#### 2.4.2.1 $\times 20$ , 0.5 NA objective

The lateral and axial resolution achieved with the  $\times 20$  objective were estimated from the FWHM of the PSF intensity profile by taking  $0.15\ \mu\text{m}$  lateral steps and  $1\ \mu\text{m}$  axial steps. The profiles were measured by projecting on a single plane the maximum intensity value of each pixel across the Z-stack of images. A 3D reconstruction of the intensity PSF is shown in figure 2.19. Figures 2.20 and 2.21 display the experimental PSF intensity profiles in the lateral and axial directions for a single fluorescent sphere. The lateral resolution, calculated as an average between the horizontal and vertical resolution, were measured to be  $r_{lat} = 2.8 \pm 0.2\ \mu\text{m}$ . The axial resolution resulted to be  $r_z = 11.0 \pm 0.5\ \mu\text{m}$ . Three nanospheres at different positions in the field of view were considered for these estimations. Since the limited amount of fluorescence excited in the nano-spheres resulted in a poor SNR, the lateral intensity profiles shown in 2.20 have been smoothed with a median filter of 1 pixel radius (each pixel value was replaced with the average of the values within 1 pixel radius). In the axial direction, the intensity plot was calculated by averaging the fluorescence levels in the region of interest in each plane. Then average background intensity was subtracted. Uncertainties were estimated with the standard error on the mean.

The intensity profiles show asymmetry in the PSF, perhaps a sign of optical aberrations. A comparison of the the measured optical resolution with expected values ( $r_{x-y} \sim 1.1\ \mu\text{m}$  and  $r_z \sim 5\ \mu\text{m}$  as from the formulas outlined in [62]) shows how the microscope is not performing in the diffraction limited regime with the  $\times 20$  objective. This is further elaborated in the discussion section.

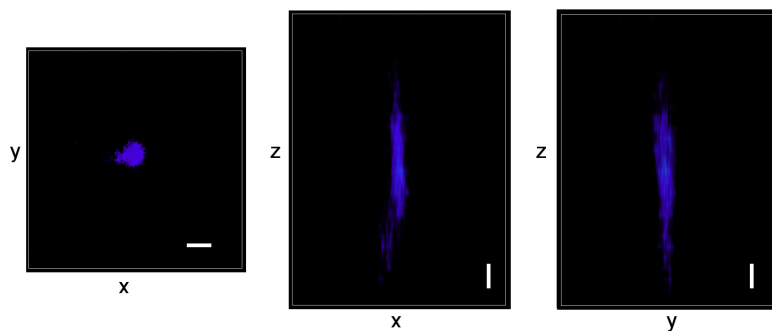


Figure 2.19: An example of a two-photon intensity PSF measured by imaging  $0.18\ \mu\text{m}$  fluorescent nanospheres with the  $\times 20$  0.5 NA objective. Scale bars are  $2\ \mu\text{m}$ . The 3D rendering was produced with ImageJ-Volume Viewer.

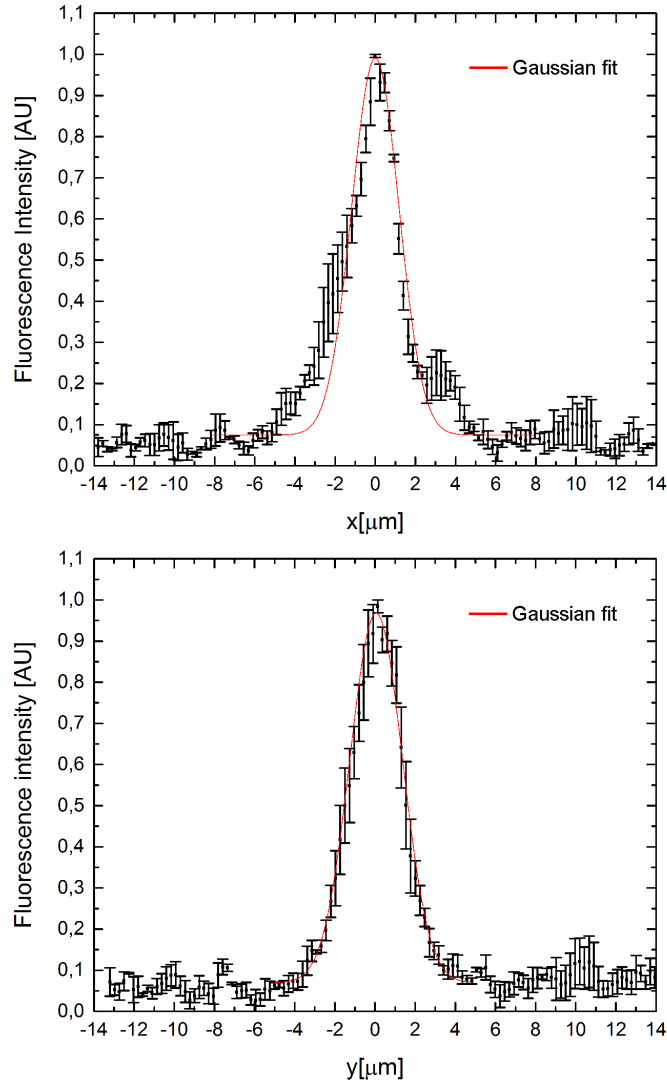


Figure 2.20: Average profiles of the fluorescent intensity of nanospheres measured in the horizontal,  $x$ , and vertical,  $y$ , directions with the  $\times 20$  0.5 NA objective. Uncertainties were estimated with the standard error on the mean of the measured values. The distributions were fitted with gaussian functions to obtain an estimation of the FWHM. It is evident how the intensity profile measured in the horizontal direction deviates from a reference gaussian profile. The gaussian fits gave the following parameters: for the horizontal direction, FWHM of  $2.8 \pm 0.1 \mu\text{m}$  with reduced  $\chi^2=6.4$  and 64 degrees of freedom; for the vertical direction FWHM=  $3.1 \pm 0.1 \mu\text{m}$  with reduced  $\chi^2=0.6$  and 37 degrees of freedom.

#### 2.4.2.2 $\times 100$ , 1.3 NA oil-immersion objective

A similar protocol was adopted for the characterisation of the  $\times 100$ , 1.3 NA oil-immersion objective. Lateral and axial resolutions were estimated from the FWHM of the intensity PSF measured by imaging 175 nm-diameter nanospheres with laser scans of  $0.100 \mu\text{m}$  lateral steps and 50 nm axial steps. The intensity profiles were calculated by projecting on a single plane the maximum intensity value of each pixel across the Z-stack of images. The intensity profiles recorded for a single

nanosphere are shown in figures 2.23 and 2.24. Figure 2.22 illustrates the 3D reconstruction of the PSF. Resolution for the  $\times 100$ , 1.3 NA oil-immersion objective was estimated as  $r_{lat} = 0.48 \pm 0.15 \mu\text{m}$  and  $r_z = 1.0 \pm 0.05 \mu\text{m}$  (4 nanospheres have been considered for this estimation). The lateral resolution is consistent with theoretical expectations as from the formula outlined in [62] (expected  $r_{lat} \sim 0.4 \mu\text{m}$ ) while the axial resolution is slightly larger than expected ( $r_z \sim 0.7 \mu\text{m}$ ).

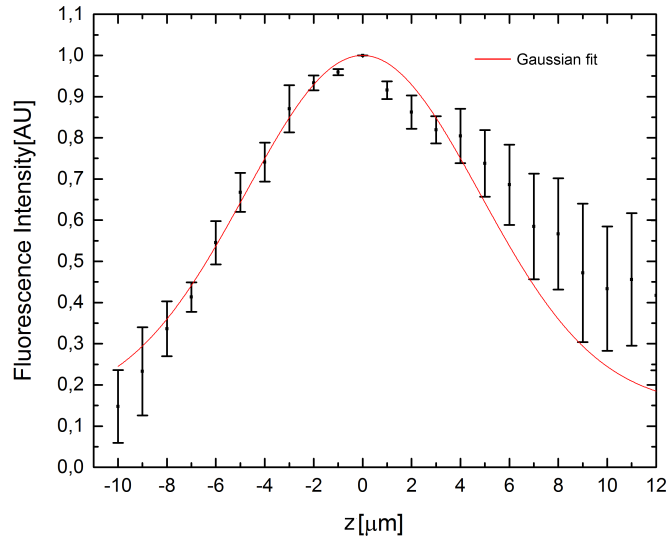


Figure 2.21: Average profile of the fluorescent intensity of nanospheres measured in the axial direction with the  $\times 20$  0.5 NA objective. Uncertainties were estimated with the standard error on the mean of the measured values. The distribution was fitted with gaussian function to obtain an estimation of the FWHM. The gaussian fit gave a FWHM of  $11.3 \pm 0.4 \mu\text{m}$  with reduced  $\chi^2=1.8$  and 19 degrees of freedom.

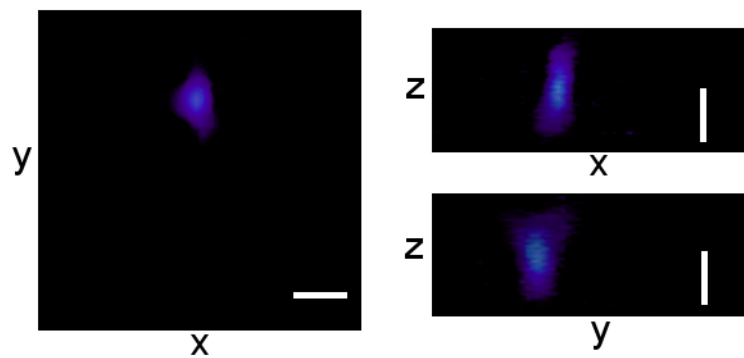


Figure 2.22: An example of a two-photon intensity PSF measured by imaging  $0.18 \mu\text{m}$  fluorescent nanospheres with the  $\times 100$  1.3 NA objective. Scale bars are  $1 \mu\text{m}$ . The 3D rendering was produced with ImageJ-Volume Viewer.

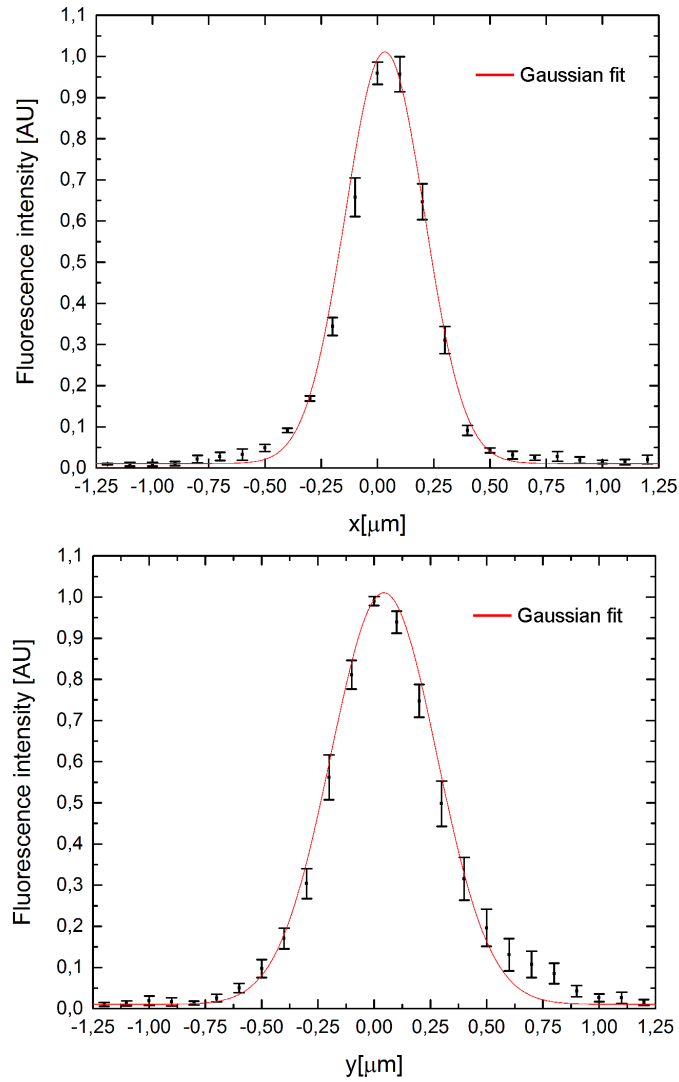


Figure 2.23: Average profiles of the fluorescent intensity of nanospheres measured in the horizontal,  $x$ , and vertical,  $y$ , directions with the  $\times 100$  1.3 NA oil-immersion objective. Uncertainties were estimated with the standard error on the mean of the measured values. The distributions were fitted with gaussian functions to obtain an estimation of the FWHM. The gaussian fits gave the following parameters: for the horizontal direction,  $\text{FWHM} = 0.41 \pm 0.01 \mu\text{m}$  with reduced  $\chi^2 = 3.31$  and 35 degrees of freedom; for the vertical direction  $\text{FWHM} = 0.55 \pm 0.02 \mu\text{m}$  with reduced  $\chi^2 = 1.74$  and 35 degrees of freedom.

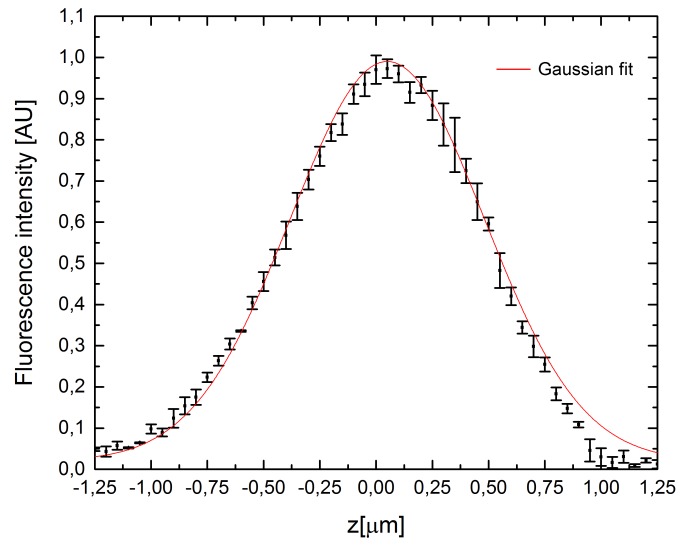


Figure 2.24: Average profile of the fluorescent intensity of nanospheres measured in the axial direction with the  $\times 20$ , 0.5 NA objective. Uncertainties were estimated with the standard error on the mean of the measured values. The distribution was fitted with gaussian function to obtain an estimation of the FWHM. The gaussian fit gave a FWHM= $1.01 \pm 0.05 \mu\text{m}$  with reduced  $\chi^2 = 9.89$  and 45 degrees of freedom.

### 2.4.3 Validation of imaging protocols

As discussed earlier, the adopted approach to planar imaging consisted of acquiring multiple image tiles, each covering a moderate area. This strategy, was used to prevent the effects the laser scanning beam has on the electrophysiological recordings (discussed in chapter 3). However, it required a precise composition of the several tiles. The procedure depends on both X-Y stage positioning, which was performed by the control software, and on off-line image stitching, performed with an ImageJ plug-in [95].

The microscope performance was validated by imaging distributions of fluorescent beads (505 exc./515 em.,  $6 \mu\text{m}$  in diameter InSpeck from Molecular Probes) in brightfield and two-photon. Figure 2.25 shows an example of overlay between the two imaging modes for a distribution of fluorescent beads. The two photon image was scaled by  $\sim 7\%$  in both directions to get an exact overlay. Calibration of pixel sizes for CCD-acquired images was retrieved from resolution charts for the  $\times 20$  objective. A linear fit of the pixel to  $\mu\text{m}$  conversion resulted in a calibration of:  $0.82 \pm 0.01 \mu\text{m}/\text{pixel}$  for the Teledyne Dalsa and  $0.46 \pm 0.02 \mu\text{m}/\text{pixel}$  for the QICAM camera.

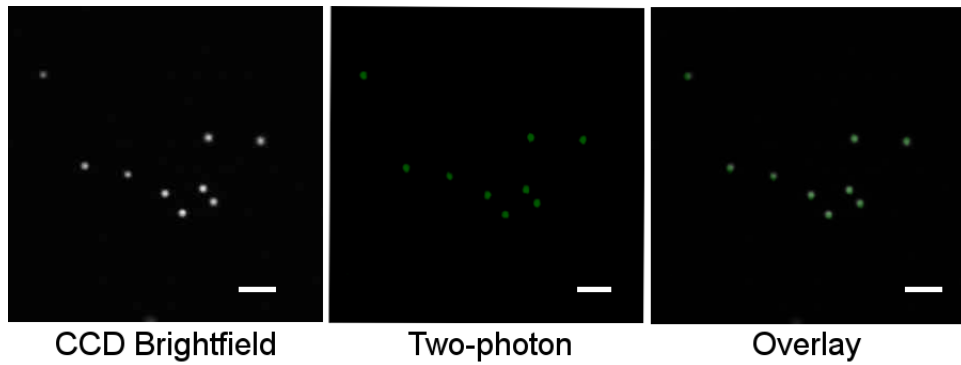


Figure 2.25: Distribution of fluorescent beads (resembling the Ursa Major constellation) imaged in brightfield, *left*, and two-photon fluorescence, *middle*; the *right* panel shows an overlay of the two. Scale bars are  $20\ \mu\text{m}$ .

The precision of the planar imaging protocol was demonstrated by imaging the interface between a LaserSoft USAF 1951 resolution chart and a fluorescent slide. Figure 2.26 shows a comparison between a brightfield image, acquired with a CCD, and a laser scanned two-photon image composed of multiple tiles stitched together. The two-photon image shows how the element 7-6,  $2.19\ \mu\text{m}$  line-width, is resolved. Unevenness in the illumination field was corrected for two-photon images by normalising the images to the illumination field measured with a fluorescent slide [96].

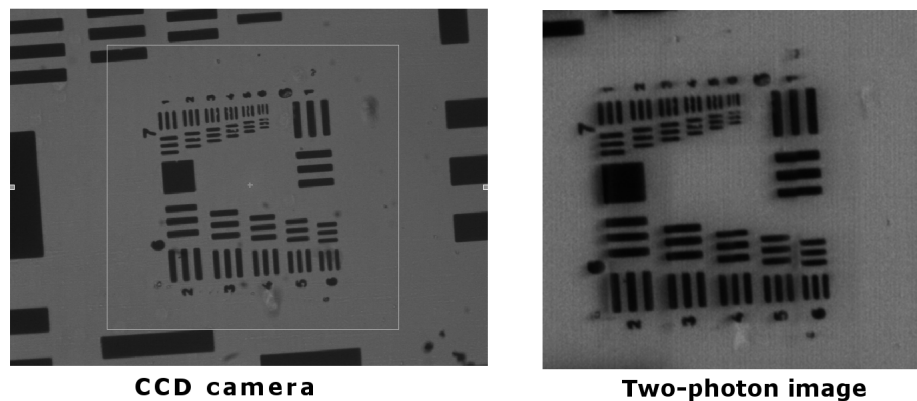


Figure 2.26: USAF 1951 Resolution Chart: brightfield image, *left*, and two-photon image of a fluorescent slide positioned on top of the chart, *right*.

The MEA is also an ideal reference of a spatial pattern fabricated at  $\mu\text{m}$  precision. Validation imaging was performed by focusing beam on the electrode plane. Figure 2.27, shows the structure of the ITO tracks and the electrodes is correctly reconstructed over an area of approximately  $\sim 240 \times 240\ \mu\text{m}^2$ .

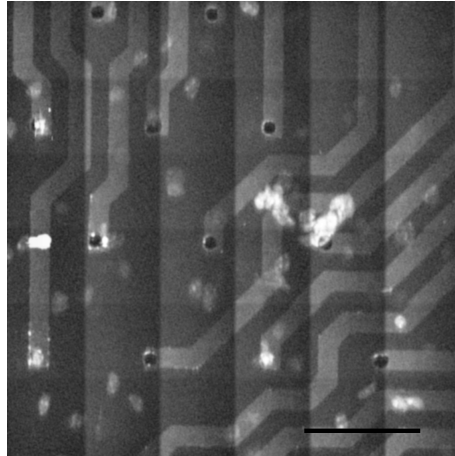


Figure 2.27: Two-photon image of DAPI-stained cells on the MEA. As further investigated in the next chapter, the ITO tracks are clearly distinguishable and properly reconstructed in the two-photon fluorescence image. Scale bar is 60  $\mu\text{m}$ .

Optical sectioning capabilities were assessed by imaging green fluorescent microspheres (6  $\mu\text{m}$  in diameter) with the  $\times 100$  objective, 1.3 NA. A 3D rendering of microspheres mounted in Vectashield mounting medium is shown in figure 2.28. Optical sectioning with the  $\times 20$  objective, 0.5 NA, will be demonstrated in the next chapter where axially resolved images of retinal tissue, acquired through the MEA, will be shown.

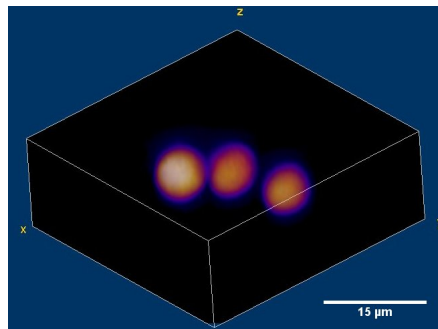


Figure 2.28: Two-photon image of 6  $\mu\text{m}$ -diameter green fluorescent microsphere. Scale bar is 15  $\mu\text{m}$ .

## 2.5 Imaging

After the characterisation stage, the microscope was validated by imaging fluorescent structures in brain and retinal tissue. This section will show images acquired from samples mounted on standard microscope slides, with 0.13-0.17  $\mu\text{m}$  thick coverslips, and expressing eYFP (excited at 920 nm) or stained with DAPI (excited at 800 nm).

### Brain imaging

Imaging performances were tested in brain slices from rat stained with DAPI or and brain slices from mice expressing eYFP. These preliminary studies confirmed that the microscope can image neural structures. Figure 2.29 and 2.30 shows examples of two-photon imaging in DAPI stained rat brain slices. The image in figure 2.30 was acquired from a cleared brain section previously mounted on a 3D MEA where the electrodes are fabricated on micro-needles [97]. The insertion points of the needles are clearly visible.

Optical sectioning capabilities were validated performing 3D imaging, with the  $\times 100$  objective, on mice brain slices expressing eYFP. While figure 2.31 shows a clear separation between two neural layers, cell bodies and processes, figure 2.32 displays four cell bodies resolved in the axial dimension.

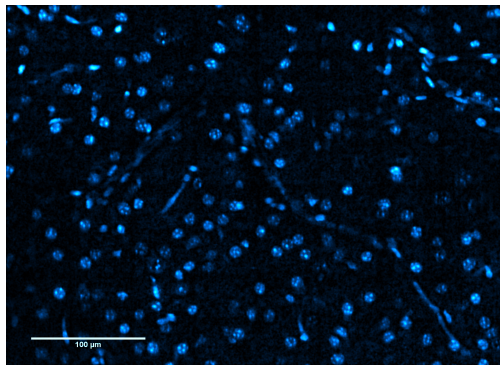


Figure 2.29: A two-photon image of DAPI-stained neural cells in the rat obtained with the  $\times 20$  objective. Scale bar is 100  $\mu\text{m}$ .

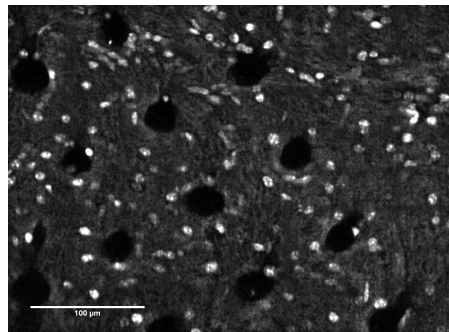


Figure 2.30: A two-photon image of DAPI stained neural cells in the rat. The imaged brain slice was previously mounted on a micro-needle array. The insertion points of the needles are clearly visible. The image was obtained with the  $\times 20$  objective. Scale bar is 100  $\mu\text{m}$ .

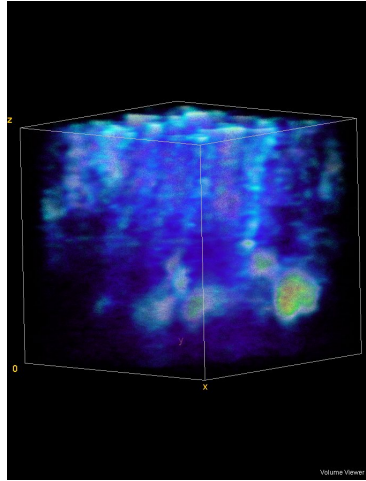


Figure 2.31: A 3D image of axially resolved neural cells expressing eYFP in a mouse brain slice. The image was obtained with the  $\times 100$  objective.

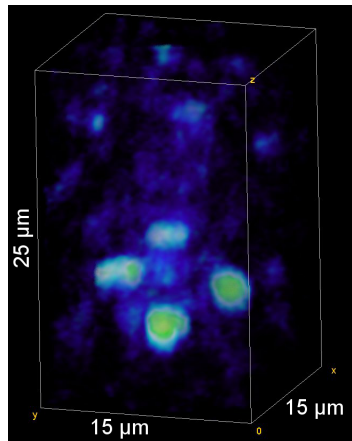


Figure 2.32: A second, 3D image of axially resolved neural cells in a brain slice from eYFP-expressing mice. The image was obtained with the  $\times 100$  objective.

### Retinal Imaging

Retinal imaging was performed on intact retinal tissue extracted from PV-Cre mouse expressing eYFP in Parvalbumin neurons. This mouse line was used to combined MEA electrophysiological experiments with two-photon imaging and two-photon optogenetic stimulation. Retinal sections were mounted on coverslips with no additional staining protocols, in order to mimic live imaging conditions. A two-photon image of retinal RGCs imaged with the  $\times 20$  objective at 920 nm illumination is shown in figure 2.33. Figure 2.34, instead, displays an image obtained with the  $\times 100$  objective.

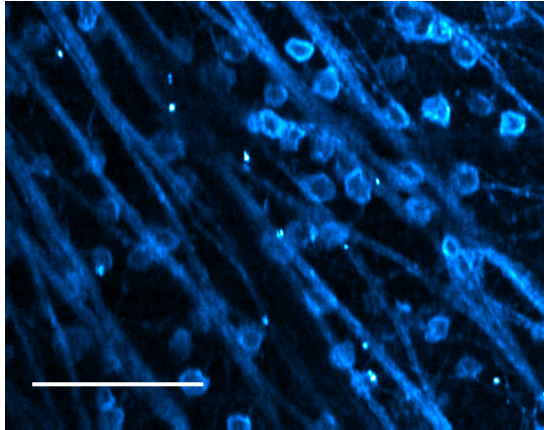


Figure 2.33: Two-photon image of RGCs in PV-Cre retina obtained with the  $\times 20$  objective. Scale bar is  $100\ \mu\text{m}$ .

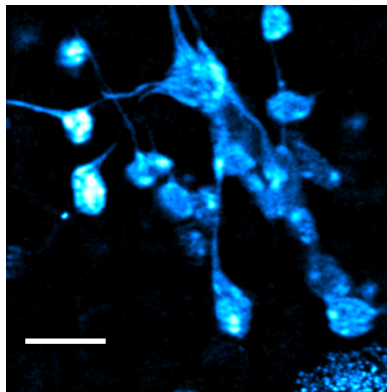


Figure 2.34: Two-photon image of retinal cells imaged with the  $\times 100$  objective. Scale bar is  $15\ \mu\text{m}$ .

## 2.6 Discussion and conclusions

This chapter reported on the construction and validation of an experimental tool that combines a two-photon microscope with a  $\mu\text{LED}$  based optical system for spatio-temporal optogenetic stimulation. This setup was designed to integrate with a high-density electrophysiological recording system. This was done to perform simultaneous recording, imaging and stimulation of genetically targeted retinal ganglion cells.

In order to perform spatio-temporal optogenetic stimulation, a  $\mu\text{LED}$  array coupled with a projection system was integrated with an inverted microscope frame which hosts the electrophysiology setup. The  $\mu\text{LED}$  pixels can deliver the necessary intensity to drive ChR-expressing cells ( $1 - 5\ \text{mW}/\text{mm}^2$  [7]) and can provide stimulation in spatial patterns of choice. The optical demagnification performed within the projection system allows the targeting of single cell somas leading to single cell stimulation. This approach was integrated with the electrophysiological recordings, as Chapter 4 will demonstrate.

In addition to the optogenetic system, a custom-made two photon microscope, designed to combine with the electrophysiological setup, was built and characterized. As detailed in the introduction, two-photon microscopy excitation of fluorescence is a valuable tool in the investigation of neural networks. Several custom-made two-photon microscopes systems guided the design and implementation of this microscope [94, 98, 99]. The two-photon system in exam was not developed with the aim to set new standards in imaging performances. Instead, the primary task was the investigation of innovative approaches for the characterisation of neural networks. Therefore, imaging protocols were tailored to integrate with the micro electrode array.

The microscope performance for two-photon excitation of fluorescence was validated by imaging reference samples (fluorescent slides, fluorescent micro-spheres, resolution charts) and neural cells expressing fluorescent markers over areas of hundreds of  $\mu\text{m}^2$ . The custom software developed to control laser scanning and data-acquisition was validated in the context of the microscope characterisation.

Optical resolution was estimated via the FWHM of the intensity PSF. This was done by imaging fluorescent nano-spheres (175 nm in diameter) with two objectives:  $\times 100$  1.3 NA oil-immersion and  $\times 20$  0.5 NA. While the  $\times 100$  objective exhibited an optical resolution in line with the theoretical expectations for a diffraction limited spot, the PSF measured with the  $\times 20$  objective presented significant asymmetry. These lead to an estimation of resolution which exceeds the theoretical limit. This can be explained by considering different factor which lead to a deterioration of the PSF. Firstly, the beam profile at the back of the objective might fail to fill the 10 mm-diameter back aperture with an even illumination. Therefore, the full NA of the objective was not exploited. This condition was likely met when imaging with the  $\times 100$  objective as its back aperture is a smaller (roughly a factor 2). Secondly, PSF measurements performed with the  $\times 20$  objective gave a lower SNR. Therefore, a spatial average needed to be performed on the pixel values to facilitate an estimation of the optical resolution estimation. Larger micro-particles (e.g. 500 nm in diameter) might serve better to estimate the  $\times 20$  resolution. Thirdly, the asymmetry of the PSF profiles testifies for the presence of optical aberrations.

However, despite the optical performances of the microscope mounting the  $\times 20$  objective are not ideal, and can be improved by further developments in the optical setup, it was possible to perform two-photon imaging in genetically targeted retinal cells (figure 2.33) with no staining enhancement. Two-photon imaging through the MEA will be demonstrated in the following chapter.

As previously detailed, the  $\times 20$  objective has a moderated numerical aperture which doesn't guarantee high-efficiency in the excitation of fluorescence. However, considering the constraints imposed on the working distance by the MEA thickness, this lens was adopted as the objective of choice for imaging during electrophysiological recordings. Alternative objectives with similar working distance and larger NA are commercially available, although expensive.

Concerning the optical path, an interesting point of discussion can be drawn around the beam

expander. Most of the optical magnification of the laser beam was obtained with two 2-inch lenses arranged in a Keplerian beam expander. While these large lenses are a convenient choice to avoid clipping of the scanned laser beam, the long distances involved in the beam expander limit the maximum scan angle the beam experiences. This, in turn, reduces the available field of view. Further developments on the microscope system might consider different arrangements for the beam expander, especially in light of the resolution measurements.

Planar scanning over hundred of  $\mu\text{m}^2$  was performed by combining multiple image tiles. This approach, validated by imaging distributions of fluorescent micro-spheres and resolution charts, was adopted to minimise the effects the scanning laser beam has on recordings and spike sorting. In fact, as the following chapter will demonstrate, laser scanning performed during electrophysiological recordings generates large artifacts which disrupt spike sorting algorithms (see Chapter 3). Since large, correlated artifacts recorded across multiple electrode sites have the potential to invalidate the recordings, the multi-tile approach was adopted because it allows to confine the laser induced artifact in a limited time-window for each electrode, while the rest of the array is unperturbed. Chapter 3 will demonstrate successful spike sorting in presence of laser induced artifacts. However, this approach limits the execution speed and, although confining the laser scan to small angles might play a role in the minimisation of astigmatic aberrations, a single scan covering the whole electrode area would remove the requirement for image stitching.

In conclusion, an experimental tool combining spatio-temporal optogenetic stimulation, two-photon microscopy and high-density electrophysiological recordings was assembled and validated. The following chapters will report on electrophysiology experiments performed in combination with two-photon imaging, two-photon optogenetic stimulation and spatio-temporal single-photon optogenetic stimulation.

## Chapter 3

# Combining two-photon excitation and MEA recordings

The combination of optical imaging and stimulation with high-density electrophysiological recordings is a promising path to gain insight into the behaviour of neural networks, as recent studies have pointed out [39]. Readout techniques, which can achieve sub-cellular spatial resolution ( $\sim\mu\text{m}$ ) at sub-millisecond temporal precision, are required to access deeper levels of information contained within the intricacies of neural circuitry. As anticipated in the introduction and detailed in the previous chapter, this challenge has been approached by implementing a single experimental setup able to incorporate multiphoton microscopy, high-density electrophysiology and optogenetic stimulation. This chapter will report on the interaction between the laser scanning beam and the electrophysiological system, will describe high-density electrophysiology experiments and, finally, will discuss pilot multi-photon optogenetic experiments.

### 3.1 Laser scanning interaction with MEA

The first part to consider is the interaction between the IR laser beam and the MEA array. The main focus of the reported measurements was to establish operating parameters at which laser scanning protocols would not damage the MEA.

#### 3.1.1 MEA composition

The high-density MEAs used for electrophysiological recordings have been designed to characterize the functional properties of retinal neural circuitry by recording RGC spiking activity in presence of a known visual stimulus. These MEAs are made of transparent material to allow for visual

stimulation of the photoreceptor response and brightfield imaging of the RGC layer. Conductive tracks are, in fact, fabricated, on a glass substrate, in the transparent conductor Indium Tin Oxide (ITO) and insulated with a transparent layer of SiN

The fabrication process is detailed in [14]. Briefly, 150 nm-thick ITO tracks are fabricated on a 1.1 mm-thick glass substrate and a protective coating of SiN is deposited on the tracks, in the range of 1 to 2  $\mu\text{m}$ , to act as an insulating layer. Circular electrodes, 5  $\mu\text{m}$  in diameter, are fabricated by opening vias into the passivation layer, in order to expose the conductive ITO electrode sites, at a pitch of 30  $\mu\text{m}$  or 60  $\mu\text{m}$ . Each ITO tracks connects an electrode site to a bond pad at the side of the array which is used to connect to read-out electronics (64-channel Intan system).

Impedances in the order of 100  $\text{k}\Omega$  are obtained by electroplating platinum on the electrodes at current density of 4  $\text{nA}/\mu\text{m}^2$  to provide the so-called 'platinum black' material. A diagram of the MEA, equipped with a plastic chamber to contain physiological solution and a grounding platinum wire, is shown in figure 3.1.

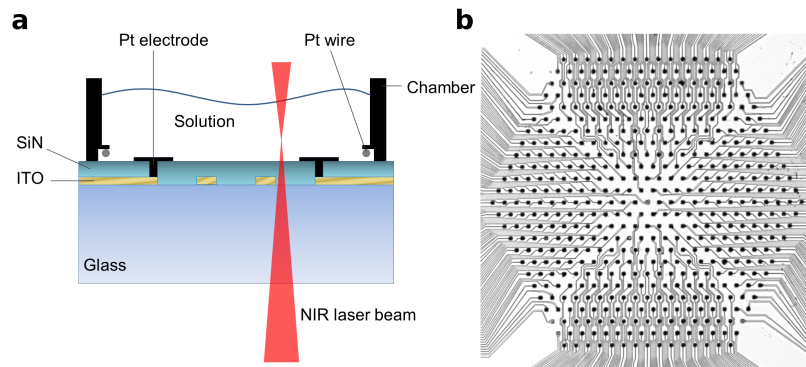


Figure 3.1: Structure of the MEA. (a) Section diagram of the MEA with a NIR laser beam travelling through the constituent materials; not to scale. (b) Image of a 519 MEA showing the electrodes (black circles) and the ITO conductive tracks (grey lines)

Chapter 4 will report on experiments in which the MEA's transparency is exploited for visual stimulation of photoreceptors, optogenetic stimulation of RGCs and brightfield fluorescence imaging of RGCs with visible light. Here, the focus is on the interaction between MEA component materials and a NIR femtosecond-pulsed laser beam, which is the light source of choice for two-photon excitation of fluorescence.

While travelling through the MEA, the laser beam encounters the thick glass substrate, the ITO tracks and, at last, the SiN layer or the Pt deposited on the electrodes. Refractive index and absorption coefficients for ITO and SiN vary according to the fabrication parameters[100]. Extinction coefficients for ITO and SiN at 920 nm are, respectively,  $1 \times 10^{-2}$  and 0 [101, 102, 103]. A plot of the refractive index is shown in figure 3.2 for values which approximate the optical properties of the layer in our arrays. It should be noted that the graph shows the refractive index for  $\text{Si}_3\text{N}_4$  while the arrays are insulated with SiN obtained with Plasma Enhanced Chemical Vapour Deposition

(PECVD): the value of the refractive index, however, is not expected to differ substantially [104]. With the exception of Pt, the optical properties of ITO and SiN indicate high transmission and small absorption coefficients at NIR wavelengths. However, clear signs of interactions, sometimes in the form of damage, have been observed by visual inspection in connection with the laser beam hitting ITO tracks or defects in the SiN.

The following sections will report on the measurements performed in order to characterize the observed phenomena and define operating parameters to perform two-photon imaging without inducing damage in the array.

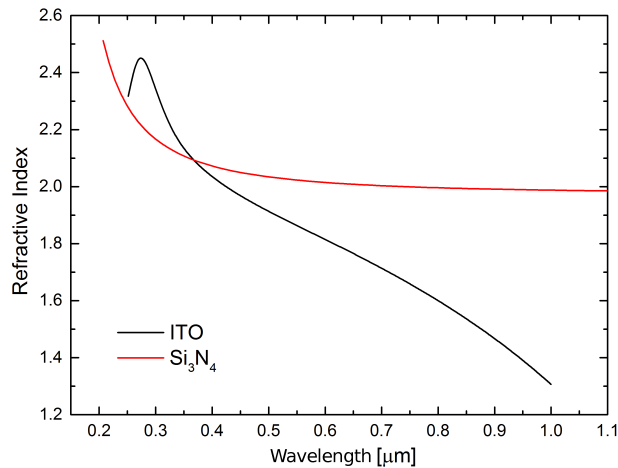


Figure 3.2: Refractive index for  $Si_3N_4$  and ITO versus illuminating wavelength. Data:  $Si_3N_4$  [102], ITO [101] via [103].

### 3.1.2 Optical resolution through MEA

The objective lens used for two-photon excitation has a 2.1 mm working distance and is designed to work with 0.17 mm thick coverslips. However, the setup described in chapter 2 aims to image retinal cells through the MEA, which is fabricated on a 1.1 mm thick glass substrate. When objective lenses are employed with an extra-thickness of glass, this tends to lead to a deterioration of the effective NA, due to aberration effects. While this phenomenon is more important for objective lenses with a high NA, even a moderate NA lens like the  $\times 20$ , 0.5 NA objective used might be affected.

The microscope's capabilities while imaging through the MEA were characterized by measuring the size of the excitation spot in the lateral and axial directions, so as to obtain an estimation of the resolution. Commonly, resolution parameters for scanning microscopes are calculated from the Full-Width-at-Half-Maximum (FWHM) of the measured Point Spread Function (PSF) or from the gradient of the response function to the fluorescence from an edge-like object (for example a

plane of fluorescent material perpendicular to the optical axis, when measuring axial resolution) [105]. However, these methods can be misled by aberrations that perturb the PSF's symmetry, such as the aberrations the glass substrate may well induce. An alternative approach estimates the resolution from the spatial extent under which half of the total integrated fluorescence excited within the PSF falls [106]. This parameter gives an estimation of the PSF spatial spread. This was obtained by looking at the intensity distribution when scanning across the separation between fluorescent and non-fluorescent regions.

Axial resolution was estimated by measuring the axial response to what can be regarded as an interface between the MEA and a semi-infinite fluorescent volume of solution. This was obtained by filling the MEA chamber with an homogeneous solution of fluorescein. An average profile of the fluorescent response was obtained by scanning the beam at increasing depths along  $z$  (step  $5 \pm 1 \mu\text{m}$ ) starting below the MEA-fluorescein interface. Resolution through the MEA in the axial direction was measured as  $r_z = 20 \pm 5 \mu\text{m}$  from the extent of the region between 25 % and 75 % of the total integrated fluorescence, as shown in figure 3.3 and previously described in [106]. This estimation was obtained by fitting the linear part of the axial fluorescence profile measured while scanning in the axial direction. The linear fit provided with a guidance to estimate the position of the points at 25% and 75 % of the total intensity.

The reference zero point on the  $z$  axis was set at the position where the laser beam was focused on the MEA top surface. This was done imaging the laser reflection with a CCD camera. It is interesting to note that the point corresponding to the 50% value of the intensity profile does not sit at zero; instead it is at approximately  $+45 \mu\text{m}$ . This indicates a systematic error in the  $z$  axis position. This error, besides an experimental uncertainty, might account for a focal mismatch occurring between the NIR exciting beam and the visible fluorescent signal. Focal mismatch is a well known problem in non-linear microscopy [62]. The observed focal mismatch implies that visible wavelengths are focused closer to the objective tip and the objective has to travel further to reach the reference position indicated by the NIR beam focus. Since this microscope operates in non descanned mode, focal mismatch has not been considered concerning for the detection efficiency [62].

Lateral resolution was characterized by imaging fluorescent micro-spheres (beads) of  $6 \mu\text{m}$  in diameter. The bead edge can be considered as a step function between the fluorescent material within in the bead and the outside of the bead. The lateral extend of the PSF can be measured by looking at the intensity profile acquired while scanning across the bead edge. This intensity profile was fitted with a gaussian function whose FWHM served as an estimator of the lateral resolution. Beads were imaged with  $0.234 \pm 0.120 \mu\text{m}$  pixel step size and  $30 \pm 10 \mu\text{s}$  pixel dwell time. By averaging over to 3 beads, in both scanning directions, lateral resolution was estimated as  $3.26 \pm 0.07 \mu\text{m}$ . Figure 3.4 shows the intensity profiles across  $x$ - and  $y$ -axis for a bead imaged in two-photon microscopy with an example of the FWHM of the derivative. As evident in figure

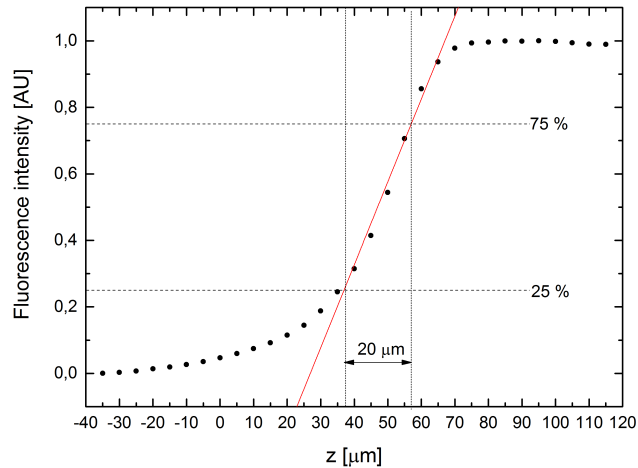


Figure 3.3: Fluorescence response to scanning the NIR beam (which passes through the MEA substrate) in the axial direction of a semi-infinite fluorescent volume of fluorescein. Negative x-values correspond to the fluorescence signal excited by the beam focussed inside the MEA, with zero being the interface between the solution and MEA. Dotted lines box the region comprising half of the total integrated power excited within the PSF. The linear fit  $y=ax+b$  had the following parameters:  $a = (2.5 \pm 0.2) \times 10^{-3} \mu\text{m}^{-1}$ ,  $b = -0.67 \pm 0.08 \text{ AU}$  with a Pearson coefficient of 0.99.

3.4, the edge response is elongated when scanning along the x-axis. This elongation is reflected in the intensity profiles. Since x is the direction in which the galvos are scanned at fast speed, this elongation might indicate photons leaking from one pixel to the adjacent ones. Moreover, this elongation might indicate positioning effects due to the galvo driver operating close to its maximum capabilities (30  $\mu\text{s}$  pixel dwell times against a sampling rate of 100 kHz). As a further consideration, the different extent of the PSF across the two axis perhaps indicates the presence of astigmatic aberrations.

It is interesting to note that the assumptions that considered the bead edge as a step-function interface between a fluorescent and a non-fluorescent region might not be accurate. This is because the bead size might be too small to accommodate for the full extent of the PSF volume. The beam diameter, in fact, is only 2 to 3 times large than the expected focal spot (2 to 3  $\mu\text{m}$ , based on previous measurements). This means that the tails of the PSF might fall outside the bead. As consequence, the total intensity excited within the bead is less than the total intensity that can be excited by the PSF volume. This implies that the PSF extent might be underestimated. If the PSF volume was underestimated, then the apparent lateral resolution parameter would be smaller than the actual value. This ambiguity can be solved by devising other methods to measure the lateral resolution through the MEA. While producing a sharp, planar distribution of fluorescent material on the MEA surface is not straightforward, larger beads might be a starting point.

By comparing the measured axial resolution through the MEA with the expectations from the equations in chapter 1 section 1.5.1, the effective NA achieved while imaging on top of the MEA

can be estimated as  $\sim 0.3$ . This degradation of the NA, however, might not be fully due to the MEA thickness. In fact, similar resolution parameters have been obtained when characterising the  $\times 20$  objective through coverslips. As discussed in chapter 2, the laser beam profile at the back of the objective might fail to fill the back aperture, thus reducing the available NA [62].

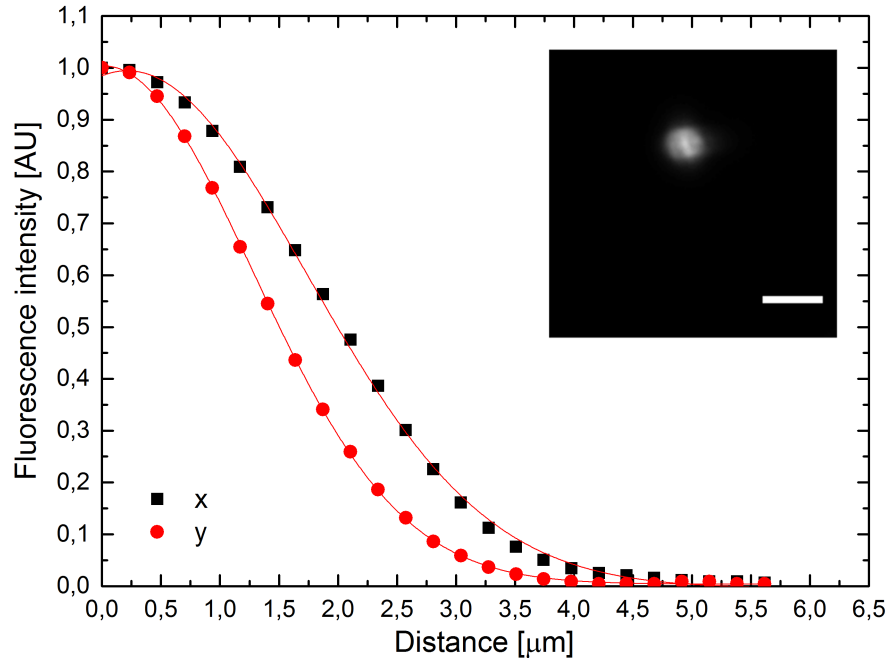


Figure 3.4: Fluorescent intensity profiles for x and y scanning directions measured across the edge of a 6  $\mu\text{m}$  diameter fluorescent microsphere. The inset at the top right shows the first derivative of the intensity profile for both scanning directions. The black and red lines are gaussian fits for, respectively, x and y scanning directions. The estimation of the PSF extent from the interpolated FWHMs produced  $3.58 \pm 0.07 \mu\text{m}$  for the x-axis and  $2.95 \pm 0.02 \mu\text{m}$  for the y-axis. The inset shows an example of a bead imaged in two-photon; scale bar is 10  $\mu\text{m}$ .

### 3.1.3 Laser interaction with ITO

Projection of the NIR light from the top is challenging, as the neural tissue require a physiological solution circulated at a tightly controlled temperature and with a dialysis membrane holding the tissue on to the electrode array. As a result, the simplest method is to project the NIR light through the transparent MEA. However, absorption effects were observed on the glass-ITO-SiN interface while performing laser scanning. This was observed as the ITO track became optically opaque after being exposed to the beam. This is shown in figure 3.5 where exposure to the NIR laser beam has resulted in damage to the ITO tracks.

Ultrafast laser ablation of ITO thin films coated on glass substrate was observed in previous works dedicated to micro-structuring of transparent materials [107]. A study on 200 nm thick ITO films, defined an ablation threshold of  $0.07 \text{ J/cm}^2$  at 810 nm wavelength with 150 fs laser pulses [108].

In particular, full ablation of 200 nm of ITO was reported, with less than ten laser pulses, at 0.5 J/cm<sup>2</sup> fluence, for an instantaneous intensity  $\sim 3 \times 10^{12}$  W/cm<sup>2</sup>.

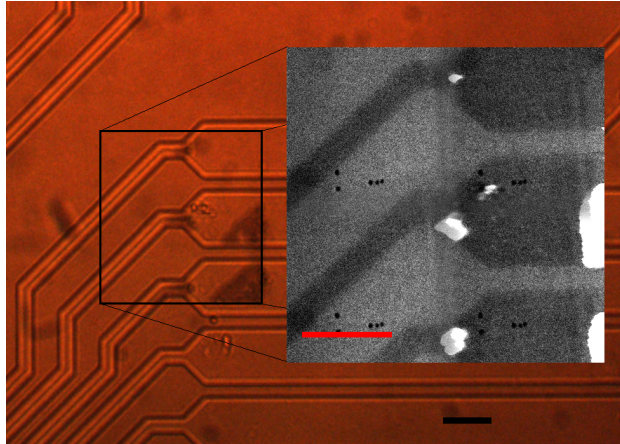


Figure 3.5: Example of laser-induced damage on ITO tracks at 30 mW incident power. The laser scanning image shows detail of the damage produced (shown in black in the main image and white in the inset). The black dots in the inset are an imaging artifact. Scale bars are 30  $\mu$ m.

In order to test the response of the MEA's ITO tracks to laser scanning at a wavelength of 920 nm, scans were performed at increasing intensities.

Focussing the beam in the vicinity of the MEA surface, damage occurred at 40 mW with 100  $\mu$ s pixel dwell-time ( $\sim 8 \times 10^3$  pulses). Laser fluence can be calculated from the beam parameters estimated in section 3.1.2. For 40 mW of average illumination power, assuming half of the power is confined in a radius of 2  $\mu$ m in diameter, the fluence per pulse is  $\sim 8 \times 10^{-3}$  J/cm<sup>2</sup> for an instantaneous intensity of  $8 \times 10^{10}$  W/cm<sup>2</sup>. In light of the moderate increase for ITO absorption from 810 nm to 920 nm ( $1.7 \times 10^3$  cm<sup>-1</sup> at 810 nm versus  $2.2 \times 10^3$  cm<sup>-1</sup> [109]), the lower fluence threshold for ITO damage with respect to the cited results can perhaps be explained with the prolonged exposure to a high number of laser pulses. As elaborated in the discussion section, faster scan rates might help in reducing the likelihood of MEA damage.

In order to mimic imaging conditions in the retinal bipolar layer, scans were conducted by focussing 70  $\mu$ m above the electrodes: no evidence of damage in the ITO was found below a level of 70 mW with a 100  $\mu$ s pixel dwell time.

Despite the measurements above, damage effects have not always been evident while scanning at the aforementioned intensities, indicating that NIR absorption in the MEA is not perfectly uniform. A useful benchmark for safe operations can be identified as: maximum of 30 mW laser power at 100  $\mu$ s pixel dwell time in the retinal ganglion layer and less than 60 mW laser power at 100  $\mu$ s pixel dwell time in the bipolar layer. At these levels, no evidence of damage was observed over the course of the experiments.

It is worth noting that the higher damage threshold in the bipolar layer doesn't translate into a

net gain in imaging performances since the extra energy will be required to compensate for SNR deterioration due to scattering effects.

A second interesting effect has been observed in connection with the ITO tracks. As anticipated in chapter 2, imaging of DAPI stained RGCs at 810 nm revealed how the glass-ITO-SiN layer gives a brighter signal than the glass-SiN interface. The generation of this luminescence was probed by scanning an 810 nm beam on the MEA at increasing intensities. Figure 3.6 compares the average signal from the two interfaces, both showing a linear dependence compatible with the hypothesis of laser light leaking through the detection filters.

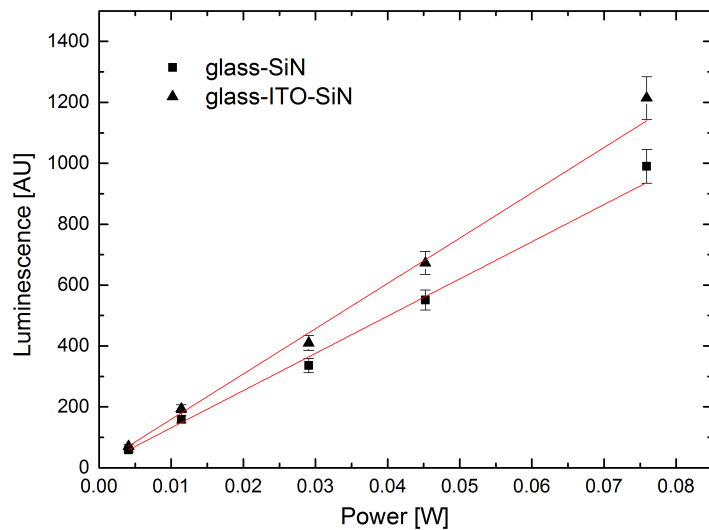


Figure 3.6: Linear dependence of luminescence signal from glass-SiN and glass-ITO-SiN interfaces. Both linear fits were accepted with 0.01 significance having Pearson's coeff.  $> 0.99$  with 3 d.o.f. Slope coefficients were estimated as  $(1.22 \pm 0.05) \times 10^4$  AU/W and  $(1.48 \pm 0.07) \times 10^4$  AU/W.

### 3.1.4 Laser interaction with platinum black and defects in the passivation layer

The platinum layer, deposited on the electrode by electroplating, is a highly conductive material (high  $Z$ ) used to reduce electrode impedances, which also strongly absorbs in the NIR. While no significant damage on the electrodes was observed below the damage threshold for ITO, at higher powers the platinum deposition can be removed completely or partially, nullifying the impedance optimisation. Section 3.2.4, dealing with electrophysiological recordings in the presence of laser scanning, shows how the electrode recording capabilities are not altered when the beam parameters are kept below the damage threshold.

As reported in the previous chapter, the laser scanning protocol is organized in adjacent tiles,

which are positioned with a piezoelectric stage. This arrangement can be exploited to avoid the electrodes during the scan so as to minimise absorption and, as detailed later, minimise laser induced artifacts in the recording. However, aligning the electrophysiology system at  $\mu\text{m}$  precision is a challenging task and a better approach would register the electrodes position in a preliminary scan and then feed the information to the laser scanning software.

Another issue are physical defects in the passivation layer, for example cracks. These appear to be prone to damage when exposed to the laser beam. In particular, cracks next to the electrodes region were often enlarged by the scanning beam. While defects can be avoided as for the electrodes, a more direct approach would use defect-free arrays, which are readily available.

### 3.1.5 Power requirements for two photon excitation

As a benchmark, it is interesting to repeat the calculation done in chapter 1 to estimate the rate of photon emission per molecule in view of the MEA damage threshold and the lower effective NA. The rate of photons per molecule can be estimated by multiplying the probability that a fluorophore absorbs two photons in the same pulse, times the pulse repetition frequency [87]. For eYFP with a two-photon cross section of  $\delta_2 = 12.5 \text{ GM}$ , the formula

$$\text{photons } s^{-1} \simeq \frac{\delta_2 P_{ave}^2}{\tau_p f_p} \left( \frac{\pi NA^2}{hc\lambda} \right)^2, \quad (3.1)$$

with  $P = 40 \text{ mW}$ ,  $\tau_p = 100 \text{ fs}$ ,  $f_p = 80 \text{ MHz}$ ,  $\lambda = 920 \text{ nm}$  and  $NA_{\text{eff}} = 0.3$  yields

$$\text{photons } s^{-1} = 5.8 \times 10^5. \quad (3.2)$$

It has been estimated, from the emission profile shown in reference [53], that the two-photon cross section for eYFP at 920 nm has half the peak absorption cross section at 960 nm. However, excitation has been performed at 920 nm since the laser was not stable at longer wavelengths.

By comparing the calculated photon rate with typical values of  $3 \times 10^7 \text{ photons } s^{-1}$  [87], it is evident how the limited NA used has a major effect in the efficiency of excitation. As detailed in section 3.3.2, acquiring images through the MEA has required illuminating intensities beyond the damage threshold.

## 3.2 Electrophysiological recordings of retinal ganglion cell activity

After establishing operating parameters for laser scanning through the MEA, the integration of the electrophysiology system with the MEA began with electrophysiological recordings on mouse retina while scanning the laser beam. The next chapter concentrates on the functional characterisation

of RGCs using the combination of an MEA and an optical system. However, an important prerequisite is to understand how any laser-induced artifacts effect the detection of retinal signalling (commonly known as neuron finding). The following experiments, detailed in this section, focus on this particular aspect.

As covered in the background chapter, the retina is a sheet of neural tissue, which sits at the back of the eye and can be thought of as an input/output circuit. The input layer (photoreceptors cell) transduce incoming photons into electrochemical signals that are decomposed by the retinal circuitry and sent to the brain via the axons of retinal ganglion cells, which constitute the output layer.

The general aim of retinal multi-electrode electrophysiological recordings is to investigate the functioning of retinal circuitry by monitoring the spiking activity of many RGCs simultaneously. In fact it is possible to characterise the functional response of RGCs against a known stimulus by isolating single firing units in the electrophysiological recordings.

All animal experiments have been conducted in strict observance of the guidelines for Animal Care and the author has obtained a personal license for the handling of small animals.

### 3.2.1 Electrophysiological recordings system

Electrophysiological recordings have been performed with the previously described 61 planar micro-electrode arrays.

In order to provide nutrients to the retina and keep it viable, the MEA was equipped with a plastic chamber, glued to the passivation layer, in which a physiological solution was constantly circulated, at 35 C, via a peristaltic pump. Ames' solution, oxygenated with a mixture of 95 % O<sub>2</sub> and 5 % CO<sub>2</sub>, 7.4 pH was used in all the experiments. The physiological solution, which is a ionic conductor, was grounded with a ring of platinum wire surrounding the electrodes.

The array was interfaced with a 64-channel read-out PCB shielded in an aluminium box that acts as a Faraday cage.

Signals recorded by the electrodes were amplified and digitised by a RHD2164 64-Channel Amplifier Board by Intan Technologies, which is equipped with 64 low-noise amplifiers ( 200 gain, 2.4  $\mu V_{rms}$ ) and a 2<sup>16</sup>-bit ADC on-chip. The smallest detectable voltage step was 0.2  $\mu V$ , though this level of sensitivity masked by the overall system noise.

Digital signals from the amplifier board were sampled at 20 kHz by a RHD2000-Series amplifier evaluation system by Intan Technologies, sent to an acquisition PC and stored for offline analysis. A 50 Hz notch filter and a lower cut-off filter at 70 Hz were imposed on raw signals in order to filter out electrical pickup.

### 3.2.2 Retinal preparations

To record signals from retinal ganglion cell layer it is necessary to extract the retina from the living eye and mount it on the micro-electrode array system. This is a challenging and delicate task, which requires practice and experience.

Retinas were obtained from mice approximately 3 to 4 weeks in age, both male and female. Eyes were enucleated after cervical dislocation (Schedule 1 method) and retinal dissections were performed in the dark, under red light illumination, to minimise metabolic demand from the cells and ensure that the retina is in a healthy condition post surgery.

After cleaning any residual muscular tissue, retinas were pierced at the edge between the cornea and the sclera. Then, a circular cut was produced, following the edge of the sclera, to detach the cornea and the iris from the posterior part of the eyeball. The following step consisted in adsorbing the lens to leave the intact eye cup in contact with the retina.

After removing any remaining vitreous with blunt tweezers, the eyecup was torn, taking extreme care not to pinch on the retina in the process.

The retina was then cut in a four-leaf shape and a suitable piece of periferic retina was isolated, trimmed to size with a scalpel and transferred on the MEA with a pipette.

After being transferred to the MEA, the retinal section was positioned on the electrode area and pressed down with a plug, which slots into the chamber and is held in position by a resistance ring. Appendix A describes the plug system in detail.

Pressing the retina is a crucial step: in order to maximise the recording of action potentials, it is in fact necessary to bring the ganglion cells as close as possible to the electrodes, without damaging the neural structure. Note that the photoreceptors are very delicate and over-pressing the retina will abolish any light responses and make functional studies of the retina impossible.

### 3.2.3 Electrophysiological identification of neurons

As a first step, electrophysiological recordings were performed without scanning a laser on the electrodes with the goal of achieving good recordings and identifying single firing units.

MEA devices can record from tens to hundreds of cells, at the kHz rate and sorting the recorded signals in order to identify individual neurons is not a simple task: a single neuron can induce signals on multiple electrodes, making isolating signals from an individual neuron challenging.

Individual firing units can be identified from their characteristic spike signals with a process known as spike sorting [110], which isolate single firing units by clustering together spikes with similarities in major components - for example, amplitude and width.

Since a typical experiment with multi-electrode array provides hundreds of GB worth of data, we performed spike sorting in an automated fashion with software, developed at the University of California Santa Cruz, whose algorithms have been previously described in [2]. In brief, spikes

candidates are found in the raw traces recorded by the electrodes when the signals overcomes and goes below a preset threshold in a short interval of time (1 to 3 ms). Typically, a threshold of 4.5 times the root mean squared noise is set for spike candidates detection. In mice, the signal amplitude can range up to 100-200  $\mu\text{V}$ . An example from an electrode raw trace with identified spikes is shown in figure 3.7.

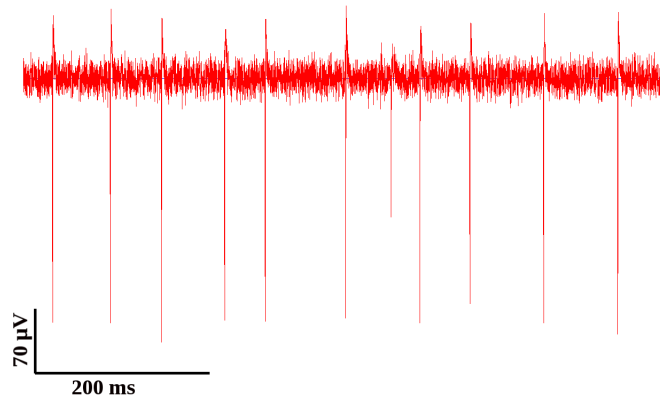


Figure 3.7: Example of raw spikes detected from a retinal ganglion cell on a single electrode.

For each spike identified on a *seed* electrode, the analog waveforms recorded around the spike time on the *seed* electrode and the surrounding ones are stored in a high-dimensionality vector. Through a Principal Component Analysis (PCA), only the  $M$  most significant variables are selected amongst the linear combinations of the measurements composing the recorded waveforms.

The data on spike waveform are then projected in the space defined by the PCA. In this space, the spikes belonging to a neuron will cluster in a confined region which can be fitted and identified as neuron candidates. Once a neurons has been electrophysiologically identified, a unique signature of its spiking activity can be computed from the pattern of voltage deflections induced on the recording electrodes. This signature, usually referred as Electrical Image (EI), is composed by the average waveforms which a neuron has generated on the electrodes, yielding information on the approximate location of the cell soma, the direction of the axon and the propagation speed of the action potential.

A bi-dimensional spatial representation of the EI can be produced by plotting the average maximum negative deflection induced by the spike at the electrode location as a circle of proportionate radius. Figure 3.8 shows an EI obtained from retinal recordings in wild type with a 61 array, 30  $\mu\text{m}$  spacing.

### 3.2.4 Artifacts from laser scanning and neuron finding

The next step in the integration of the laser scanning microscope with the electrophysiology system consisted of verifying the performance of the electrophysiological system during laser scanning.

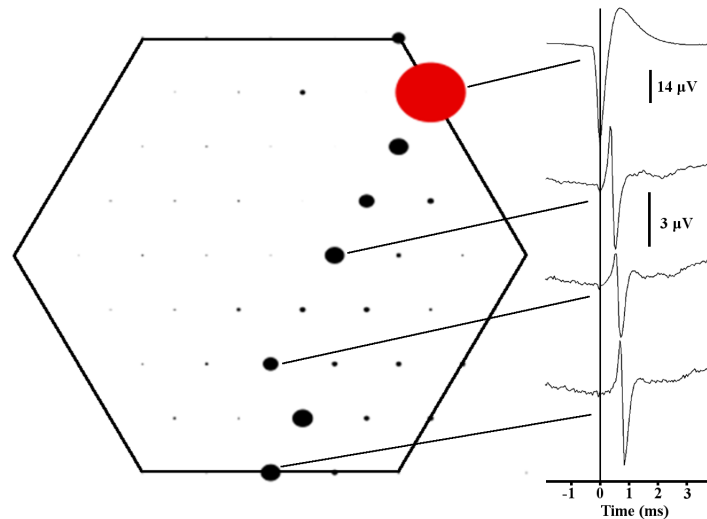


Figure 3.8: Example of an Electrical Image (EI) calculated from a mouse retinal ganglion cell. The EI highlights the direction of the axon, an approximate location of the cell soma and the spatio-temporal pattern of the elicited action potential. The hexagon outlines the area covered by the array of microelectrodes. Within this boundary electrodes, that have detected a signal, are shown as a black circle, the diameter of which gives an indication of the signal amplitude. The red circle indicates the “Seed” electrode, where the signal from the neuron was the least contaminated - typically this is the signal with the greatest amplitude and as a result the circle diameter is reduced by a factor of 4 to ensure the circle does not mask neighbouring electrodes.

The presence of a scanning laser beam complicates the process of neuron identification because the electric field associated with the laser pulse induces artifacts on the conductive elements of the MEA. These artifacts vary in amplitude and waveforms, covering a parameter range that overlaps with neural spiking activity. As a consequence, laser-induced signals are detected as spike candidates during the signal processing steps, which results in complications during the neuron identification process (contamination of the neuron clusters in principle component space). Despite significant advances in the past decades, which allowed spike sorting to be translated to microelectrode array recordings, the limited efficiency of spike sorting algorithms is a well recognised problem in the neuroscience community [111].

In order to investigate the effect of laser-induced artifacts in neuron identification, electrophysiological recordings have been performed while raster scanning a femto-second pulsed laser beam, described in chapter 2, in the vicinity of the electrode area. To mimic imaging or stimulating conditions, the beam was focussed above the electrodes, tuned at 920 nm and modulated in power at  $\sim 30$  mW.

Raster scanning protocols were organised in a matrix of adjacent tiles and clocked with a TTL pulse at the beginning of each scan so to have a reference for the beam position on the MEA.

### Artifacts

The observed laser-artifact varied in amplitude and waveforms according on the position of the beam with respect to the conductive elements. For a pixel dwell time of 50  $\mu\text{s}$ , the artifact amplitude ranged from tens of  $\mu\text{V}$  to  $\text{mV}$ ; at the same time, the temporal extension of the artifact waveforms spanned from 5 to  $\sim 15$  ms. Examples of artifact in a portion of raw data on two neighbouring electrodes are shown in figure 3.9 .

Interestingly, simultaneous artifact have been observed on different electrodes. Simultaneous artifact with opposite polarity, as in figure 3.10, can be explained by capacitive coupling effects between the tracks. Conversely artifacts occurring at the same time with a similar waveform, as in figure 3.9, might be due to simultaneous absorption of photons while the focal spot is travelling between the two electrodes.

The density of photons in the tails of the focal distribution can be estimated assuming a Gaussian intensity profile. The effective NA calculated in section 3.1.2 can be used to estimate the intensity along the axial direction: with 30 mW of illuminating power, at  $\sim 30$   $\mu\text{m}$  from the focal point, half of the pulse is expected to be confined in a diameter of  $\sim 12$   $\mu\text{m}$  for an instantaneous intensity of  $4 \times 10^9 \text{ W/cm}^2$ . By considering this parameter as a FWHM, the intensity distribution can be approximated with a gaussian function with  $\sigma = FWHM/2\sqrt{2\ln 2} \sim 5$   $\mu\text{m}$ .

Since the fraction of the total integral of a Gaussian comprised from  $3\sigma$  to infinity is  $\sim 1.3 \times 10^{-3}$ , an electrode positioned 15  $\mu\text{m}$  away from the focal spot can receive up to  $5 \times 10^6 \text{ W/cm}^2$ . A comparison with a typical illumination from LED in optogenetic stimulation experiments, which delivers  $10 \text{ mW/mm}^2 = 1 \text{ W/cm}^2$  and doesn't generate artifacts (see Chapter 4) clarifies how electrodes in the proximity of the focal spot can receive substantial illumination.

### Neuron finding

Laser induced artifacts interfere with spike sorting since spike clusters are contaminated by the presence of false spike candidates. Moreover, while neural spikes can be successfully detected amongst a burst of artifacts of similar amplitude and waveform as shown in figure 3.11, no evidence of spike detection has been found in the presence of large artifacts which dwarfed the amplitude of neural spikes.

However, neuron identification can be performed in artifact affected recordings, as figure 3.12 shows, albeit with a low efficiency. In a comparison between artifact-affected and artifact-free recordings in two retinas where 12 and 3 neurons were respectively identified in the absence of artifacts, 1/12 and 1/3 neurons could be retrieved in the artifact-affected recordings.

It is worth noting, however, that neuron identification in the artifact affected recordings was conducted on a limited spike statistic generated within the laser scanning execution time.

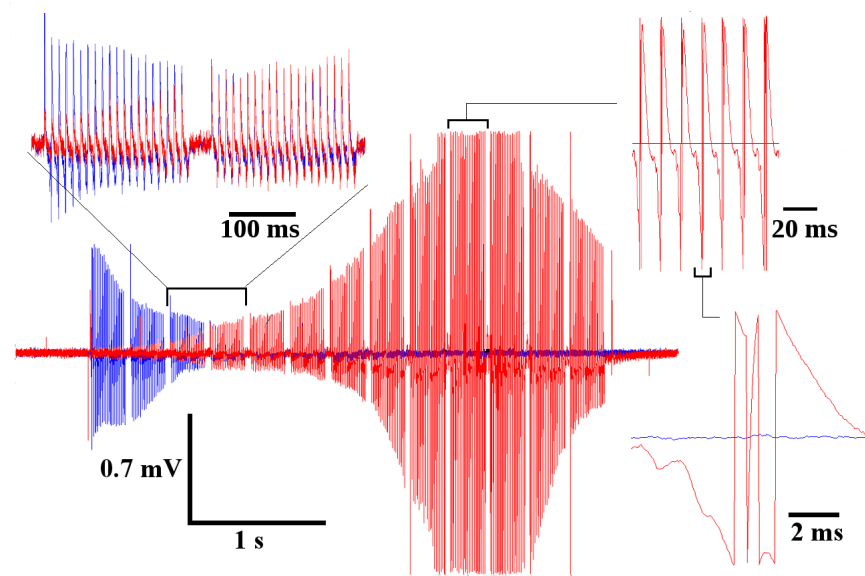


Figure 3.9: Example of the voltage deflections induced by the laser beam on two neighbouring electrodes. Close ups show simultaneous signals with similar waveforms, *top left*, and voltage deflection associated with the beam crossing an electrode, *top and bottom right*.

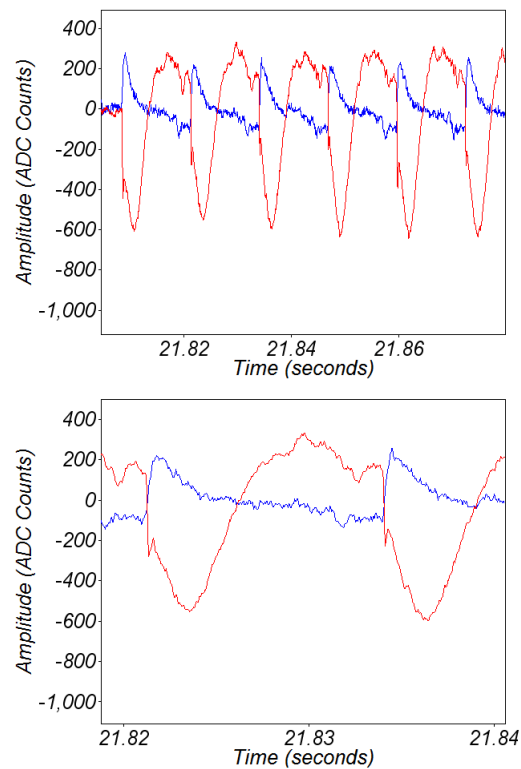


Figure 3.10: Example of capacitive coupling between two neighbouring tracks. The red line is from an electrode on which the beam is incident and the blue track has an induced signal from capacitive coupling. 1 ADC unit corresponds to  $0.7 \mu\text{V}$ .

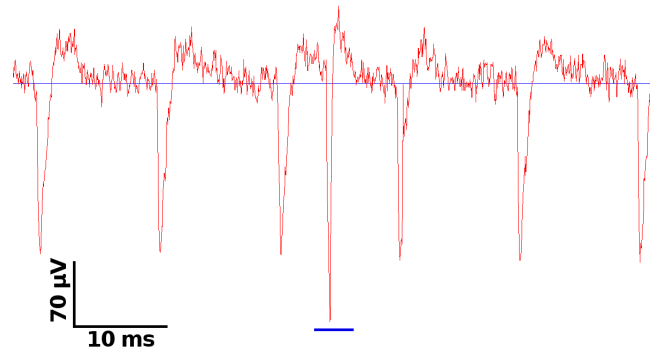


Figure 3.11: Example of a spike detected amongst laser-induced electrical artifacts: the spike is underlined in blue. 1 ADC unit corresponds to 0.7  $\mu\text{V}$ .

While it is reasonable to assume that a longer recording after the end of the laser scan would be beneficial, the artifact contribution could also be moderated by recording over multiple scan routines. This approach, in fact, would diminish the relative exposure of each electrode to the laser beam.

Further discussion on approaches to limit the effect of artifacts on neuron identification will be covered at the end of the chapter.

### 3.3 Experiments towards electrophysiology, imaging and optogenetic stimulation in PV-Cre mouse

As detailed in the previous sections, the presence of a scanning laser beam induces artifacts on the electrophysiological recordings and although sometimes this can be limiting, in terms of neuron identification, it is possible to conduct successful experiments.

The last section of this chapter reports on pilot experiments conducted on genetically modified mice to investigate two applications of the multi-photon setup: imaging the retina while alive on the array and stimulating optogenetic response from the ChR2-transfected retinal ganglion cells.

#### 3.3.1 PV-Cre mouse

Experiments were conducted on a genetically modified mouse line, which expressed a protein fusion ChR2-eYFP in Parvalbumin (PV) neurons, targetted with a Cre-recombinase promoter. As covered in the background chapter, cellular sub-populations with genetic identity can be targetted with promoters in order to express opsin proteins, such as ChR2, in a subset of cells. We used the offspring of PV-Cre animals crossed with Ai32 animals that expressed ChR2-eYFP in ubiquitous region of DNA. This produced animals with ChR2 expressed in PV-cells.

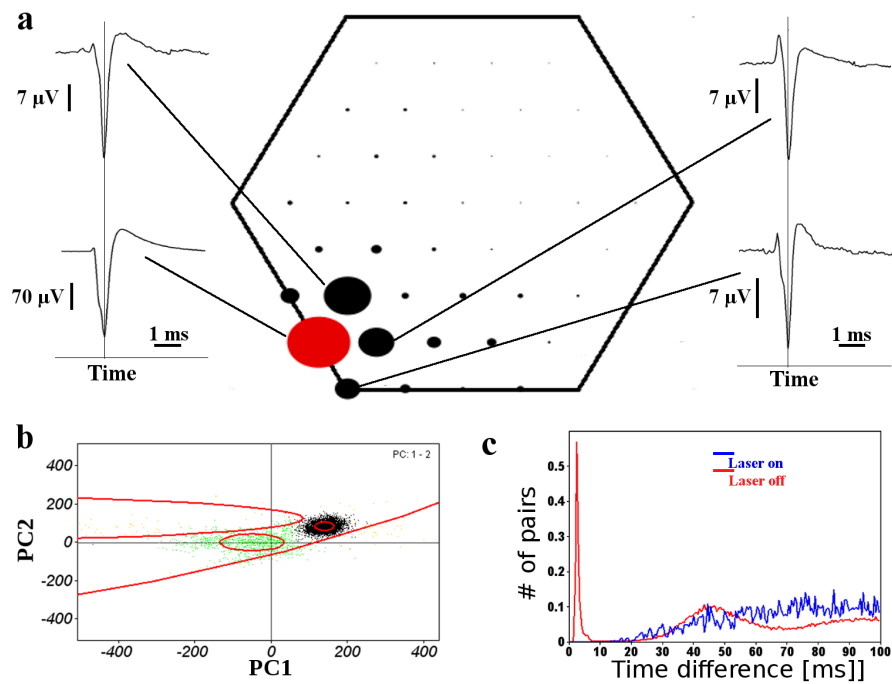


Figure 3.12: Example of a neuron electrophysiologically identified during laser scanning. (a) Electrical image with electrode traces. (b) Portion of the principal component space where the spikes are projected. The black cluster is formed by the spikes from the identified neuron; the green and orange clusters are possibly generated by laser induced artifacts or noise. The red lines represent the boundaries of the 2D Gaussian fits used to identify the neural clusters. The line shows the 1-sigma level of the fit. (c) Distribution of the inter-spike intervals for the same neuron recorded during laser scanning (blue) and with the laser turned off (red).

Parvalbumin (PV) is a calcium binding protein, widely expressed in the central nervous system, which has been observed in subclasses of retinal cells of various vertebrate species [112]. While a recent work on the functional diversity of RGCs in the mouse has identified 14 PV-expressing RGCs types [21], previous morphological investigation had found native immunoreactivity for PV in approximately a third of the RGCs [113]. However, a recent investigation by Gabriel et al. found no evidence of successful expression of a desired transgene in PV-retinal neurons when crossing PV-Cre mice with a line analogous to Ai32 [114]. Analogous here means that the line used by Gabriel et al. expressed the transgene in the same DNA region that is connected to ChR2 in Ai32 mice. As shown in figure 3.13, a dim fluorescence was observed from portions PV-Cre retina: the image in figure 3.13, which shows the retina mounted on the MEA, was acquired with an arc lamp at full power and long exposure time (612 ms).

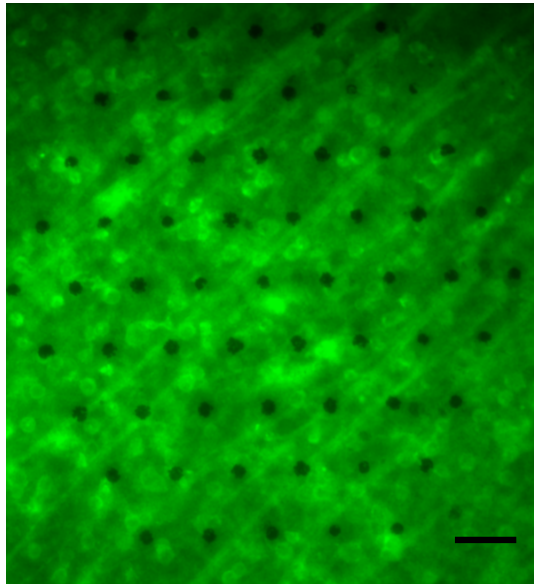


Figure 3.13: Image of a piece of PV-Cre retina mounted on the MEA. The black circles show the Pt-coated microelectrodes and the green indicates the fluorescence from the eYFP. Scale bar is 60  $\mu\text{m}$ .

### 3.3.2 Two-photon Imaging through the MEA

Two-photon imaging experiments have been performed by scanning a femto-second pulsed laser beam on retinas from PV-Cre mice mounted on the MEA.

The microscope was equipped with the  $\times 20$ , 0.5 NA objective lens whose resolution through the MEA has been characterized in section 3.1.2.

The dim levels of fluorescence observed in brightfield imaging testify for a weak expression of the ChR2-eYFP protein fusion; since the fluorescence yield is proportional to the concentration of

fluorescent molecules, obtaining a good SNR in weakly labelled tissues requires high excitation intensities. However, as detailed in section 3.1.3 power limits have to be considered so as not to induce damage in the MEA. The research question of interest was, therefore, whether RGCs can be imaged through the MEA, with a moderate NA, without damaging electrodes and tracks. If so, this opens up the possibility of determining the morphology of genetically targetted neurons at the same time as collecting their position with respect to the microelectrodes, which is collecting the functional information from the cell.

Acquiring images of RGCs while complying with the excitation parameters prescribed in section 3.1.3 is challenging, since images produced with 30 mW of illuminating power and pixel dwell times ranging from 30 to 100  $\mu\text{s}$  showed unsatisfactory SNR. Acquiring images of living genetically targetted RGCs through the MEA, sometimes required high excitation powers (80-120 mW). Long pixel dwell times (600  $\mu\text{s}$ ) were used to increase the number of collected photons. In order to comply with the established MEA safety limits and to employ more practical pixel dwell times, the expression of fluorescent markers is a central parameter that needs to be improved.

Figure 3.14 shows a two-photon image recorded through the MEA where RGCs cell bodies are clearly distinguishable. The image consists of adjacent scans stitched together with ImageJ [92]. An example of two photon imaging above the electrode area is shown in figure 3.15. While RGC bodies can be seen besides electrodes and tracks, the SNR is low and undesired absorption effects could not be avoided. These results clarify how RGC cell bodies can be imaged in multi-photon microscopy, with a 0.5 NA lens, through the MEA. Moreover, it is possible to register cell body positions in 3D, as shown in figure 3.16, where a  $60 \times 60 \mu\text{m}^2$  scan has been performed from the array surface to 55  $\mu\text{m}$  deep into the retina. The discussion section at the end of the chapter will cover approaches to improve imaging performances while reducing the average power needed for excitation of fluorescence.

### 3.3.3 Two-Photon optogenetics with MEA recordings

As covered in the background chapter, optogenetic techniques allow the stimulation of neural activity in genetically-targetted neural populations with high-spatio temporal precision, by delivering a visible light stimulus. A combination of optogenetics and MEA recordings is therefore an interesting approach for the characterisation of retinal neural circuits selected on a genetic basis. This section will report on pilot experiments towards optogenetic activation of ChR2-transfected RGCs with two-photon stimulation.

While the spectral sensitivity of common optogenetics probes peaks at visible wavelengths [7], two-photon stimulation of optogenetic response offers advantages in retinal applications. In first

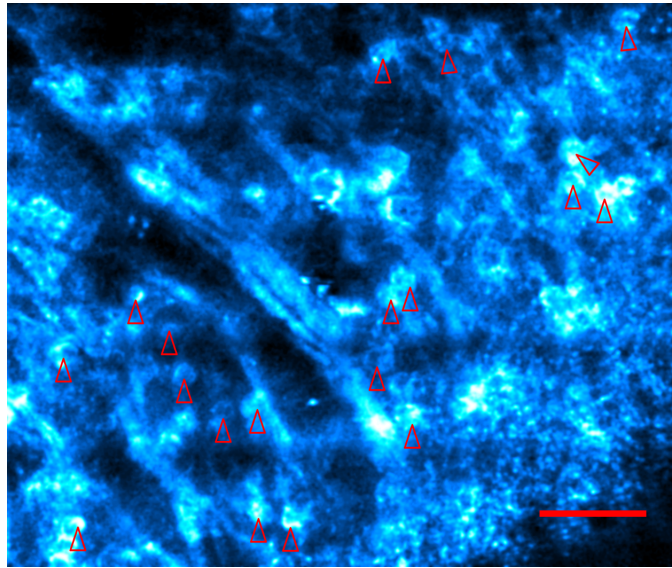


Figure 3.14: Two photon image of a portion of PV-Cre retina mounted on the MEA. RGC bodies are indicated by empty arrowheads. Scale bar is 50  $\mu\text{m}$ .

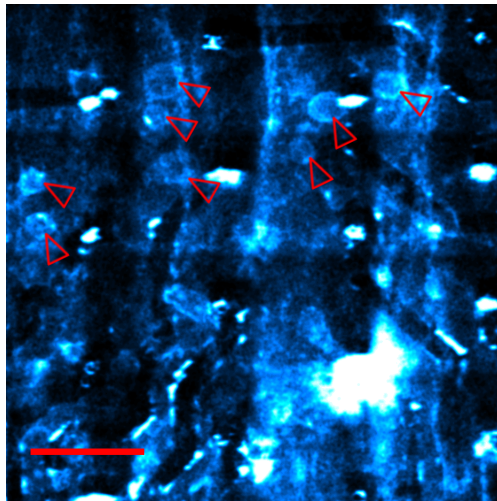


Figure 3.15: Two-photon image of a portion of PV-Cre retina on the MEA electrode area. RGC bodies are indicated by empty arrowheads. Scale bar is 50  $\mu\text{m}$ .

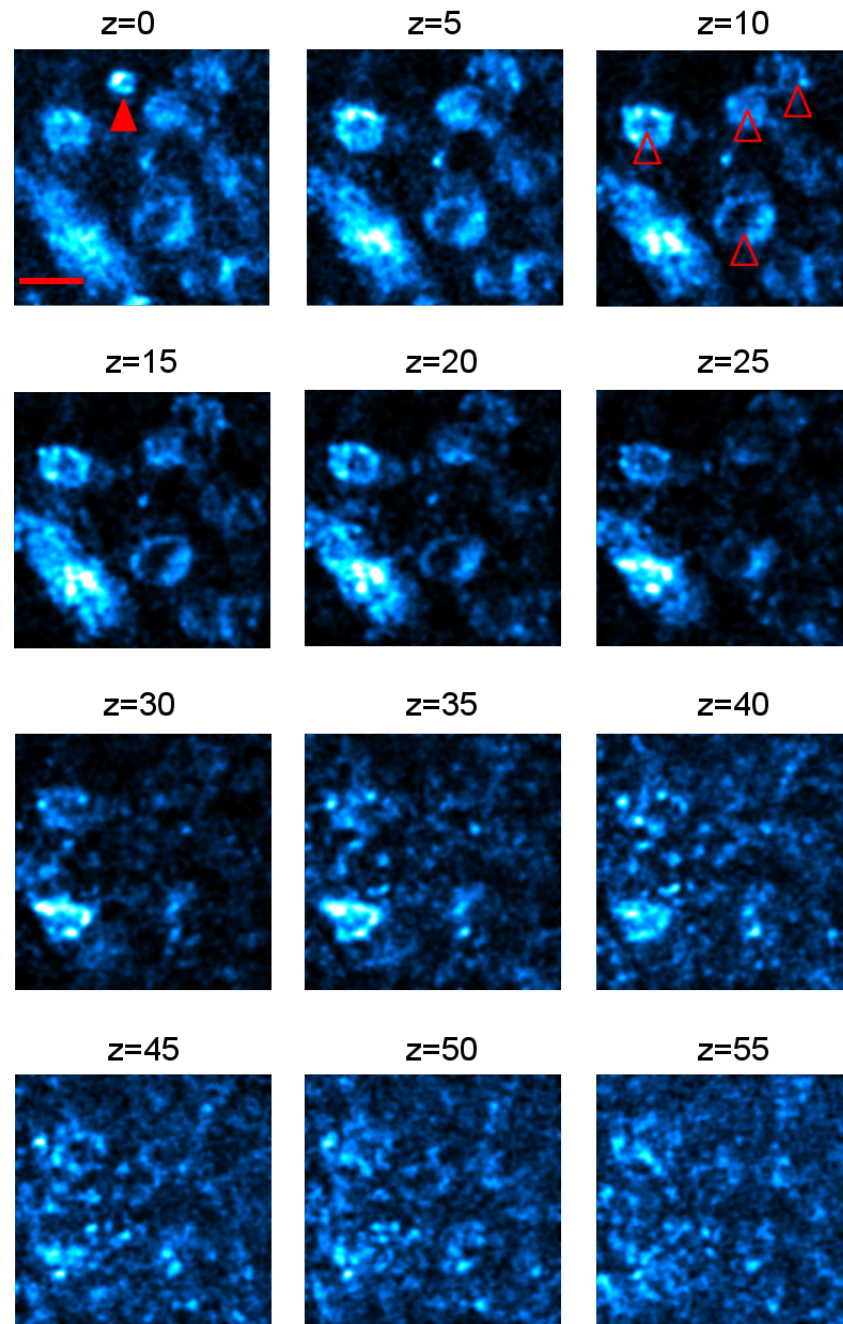


Figure 3.16: Z stack acquired in two-photon from the surface of the MEA to 55  $\mu\text{m}$  deep into a portion of PV-Cre retina. The filled arrowhead indicates a recording electrode; cell bodies are indicated by empty red arrowheads. Scale bar is 15  $\mu\text{m}$ .

instance, since photoreceptors are insensitive to NIR wavelengths, it is possible to elicit responses from RGCs-only without employing pharmacological blockers (see Chapter 4) to stop signal propagation through the retina. Secondly, the intrinsic sectioning capabilities and the penetration depth of two-photon stimulation gives access to bipolar and amacrine cells, populations that are challenging to reach with single-photon stimulation.

Two-photon optogenetic stimulation during MEA electrophysiological recordings has been investigated in the ganglion cells layers of retinas from PV-Cre mice. As demonstrated by [38] and covered in the background chapter, despite having a relatively high two-photon absorption cross section, ChR2 has a rather low channel conductance. As a consequence, the stimulation area has to be enlarged to recruit enough ChR2 molecules. Seminal works on two-photon excitation of ChR2 achieved this by artificially reducing the objective NA or by scanning the laser spot across the cell membrane.

In light of the limited expression of ChR2 in the recorded retinas, a scanning approach has been adopted in addition to the low effective NA arising from the interaction with the MEA glass substrate (see section 3.1.2).

Stimulation runs consisted of 250 stimulation, at 2 Hz, with the femto-second pulsed laser tuned at 920 nm and modulated in power at 30 mW. Each stimulation consisted of a spiral scan produced by inducing two sinusoidal waveforms, in quadrature of phase, on the galvanometric mirrors. Scan parameters were modulated to cover an area of approximately 20  $\mu\text{m}$  in diameter. Scans were clocked with a TTL pulse and a monitored in time with a software clock control which indicated  $\sim 90$  ms of execution time. As earlier reported, galvanometric mirrors can be moved at a maximum frequency of 30 kHz. An example of the spiral scan is shown in figure 3.17.

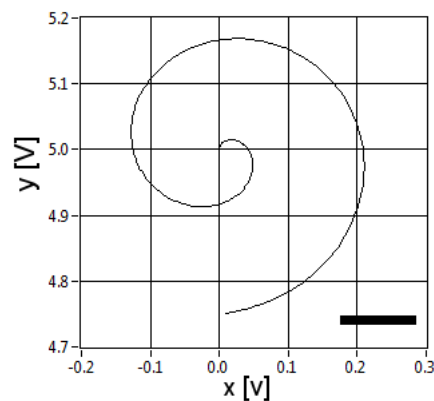


Figure 3.17: Example of a spiral scan induced on the galvanometric mirrors. Scale bar corresponds to  $\sim 6$   $\mu\text{m}$  displacement in the object plane. Voltage on the y axis is subjected to a 5 V offset.

Figure 3.18 shows an epifluorescence image of a PV-Cre mouse retina mounted on the MEA: the red Region of Interest (ROI) indicates a targetted area, presumably hosting a cell soma, where spiral scans were originated. Stimulations were targetted to this area by moving the piezo-electric

stage on which the electrophysiology system was mounted. As previously stated, the expression of fluorescent markers can be improved.

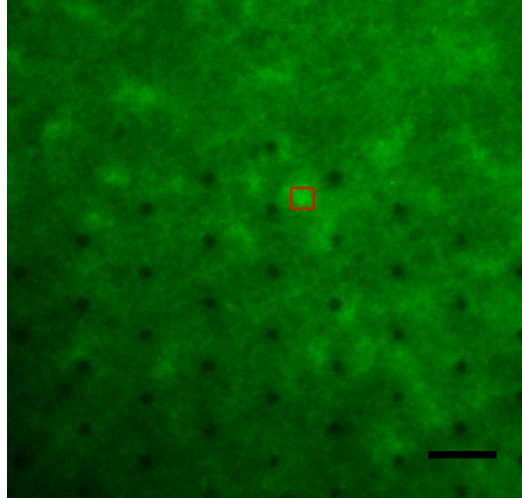


Figure 3.18: PV-cre retina mounted on MEA. Red ROI indicates the targetted area for two-photon optogenetic stimulation. Scale bar is 30  $\mu\text{m}$ .

As detailed in section 3.2.4, the presence of a scanning beam affects the electrophysiological recordings by inducing contamination in the spike clusters or by preventing spike detection. While it has been possible to identify individual neurons by manual clustering, this occurred in presence of contamination effects.

A signature of optogenetic activation of spiking activity has been looked for in the temporal correlation between recorded spikes and the temporal trace of the laser stimuli. Peri-Stimulus Time Histograms (PSTHs) were produced by calculating the time interval between each recorded spike and the last preceding TTL pulse. These time intervals were binned in 20 ms bins. The number of spikes falling in each bin was then averaged over 250 stimulations so as to obtain a distribution of the number of spikes per bin per stimulation. If a cells were optogenetically stimulated by the laser beam, the number of spike per bin is expected to increase and peak during the laser stimulation. No evidence of two-photon activation of Chr2 was observed over 12 targetted RGCs in a single retina where neurons could be electrophysiologically identified; four experiments have been ignored because of low or absent spiking activity.

The investigation of PSTHs clarified how the presence of laser artifacts interferes with spike detection. Figure 3.19 shows an example of PSTHs calculated, for the same neuron, with and without laser stimulation: the quick drop in spike rate is likely connected to a reduced efficiency in spike detection when the laser beam hits or retrieves from the MEA. A discussion on the optogenetic stimulation protocols is postponed to the next section.

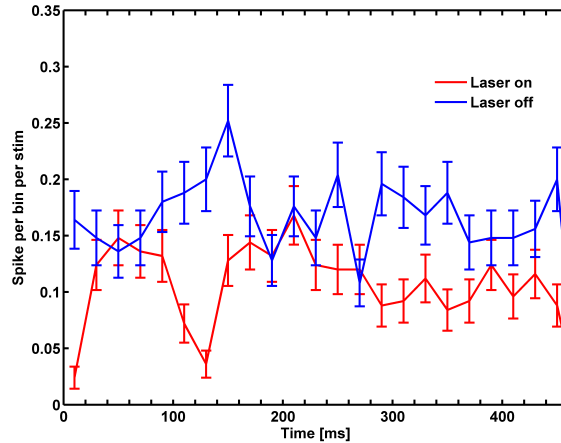


Figure 3.19: Peri-Stimulus-Time-Histogram (PSTH) calculated for a neuron during laser stimulation (red line) and during a control run with the laser beam blocked (blue line). The drops in spike rate are connected to reduced efficiency in spike detection that is synchronised with the beam onset/offset.

### 3.4 Discussion and conclusions

The present chapter has detailed the integration between the high-density electrophysiology system and the two-photon laser scanning microscope.

The purpose of the reported studies was, firstly, to understand the interaction between laser light and electrophysiological recordings in the context of neuron identification, with particular attention paid to the array integrity. Secondly, the chapter aimed to understand the possibilities connected with two-photon imaging of intact and living retinas on the MEA. Thirdly, exploratory experiments towards two-photon optogenetic stimulation were performed.

#### 3.4.1 Laser interaction with the MEA

As stressed in section 3.1.3 high intensities of the laser beam can damage the MEA beyond repair. This is clearly an undesirable side effect, which can be significantly reduced if not avoided.

From the fabrication point of view, the likelihood of laser induced damaged can be minimised by obtaining passivation layers and ITO tracks free from physical defects. However, not only this is a challenging task, but it is compounded by thermal damage that affects the interface areas. For example, the area surrounding the platinised electrodes, will always be a point of weakness.

An effective approach would, instead, focus on reducing the energy deposition from the laser beam. This could be obtained by enhancing the fluorescence yield and/or by using higher scan rates.

The excitation of fluorescence can be improved by using objectives with higher NA. However, as detailed in section 3.1.2, the thickness of the MEA requires objectives lenses with long working distances to be employed. Typically, long working distance objectives have a moderate NA which, as discussed earlier, is not ideal for two-photon excitation. While objectives with long working

distance and high NA are commercially available, they are very expensive and might turn out to be ineffective unless arrangements in aberration correction are taken. In fact, higher NAs are more prone to aberrations while travelling through thick glass interfaces [115]. From the labelling point of view, as discussed in section 3.3.1, the fluorescence from PV-Cre mouse retinas was very dim. Since genetic lines with higher expression of fluorescent markers in the retina are available, these animals could be used in future experiments to investigate multi-photon imaging protocols through the MEA with lower average powers.

Two-photon microscopes with non resonant scanning techniques use pixel dwell times in the order of a few  $\mu\text{s}$  [87]. While faster galvanometric mirrors can help reducing the exposure time of the MEA, this will not improve the SNR of images unless a stronger fluorescent labelling or an objective with higher NA are employed.

### 3.4.2 Electrophysiology and laser-induced artifacts

Laser scanning protocols performed during electrophysiological recordings experiments are subjected to laser-induced artifacts which can be detected as spike candidates and contaminate the clusters used for neuron identification.

However, identification has been successfully performed in presence of laser induced artifacts. Unfortunately, due to the limited statistics of neurons recorded, no spikes have been found on electrodes subjected to large artifacts: it is therefore not possible to conclude that neuron identification is possible regardless of the artifact magnitude. Nonetheless, scanning protocols organized in a matrix of tiles mean that each electrode is contaminated by laser-induced artifacts for a limited amount of time only. It is therefore reasonable to assume that neuron identification would not be jeopardised by a drastic approach which dismissed the contaminated portion of raw data electrode by electrode. In fact, since sufficient spike statistics can be built running longer recordings. Clearly, neuron identification would benefit from lower average powers since voltage deflection would be smaller and simultaneous artifact on different electrodes would be less likely to occur.

### 3.4.3 Two-photon optogenetic experiments

Pilot experiments for two-photon optogenetic stimulation have been conducted on retinas from PV-Cre mice. As detailed, no significant temporal correlation between recorded spikes and laser stimulation was observed. This might be due to the low expression of ChR2, testified by the low levels of fluorescence or to non-ideal parameters in the stimulation. Mouse line with higher expression of fluorescence, as for example the Thy1 of Grik4-Cre lines which have been used in the experiments reported in chapter 4, are an interesting option for future experiments.

Rickgauer et al. [38] reported an increase in spike amplitude inversely proportional to the scan duration, with better results for scans of  $\sim 16$  ms. The employed spiral scans were designed to last for 50 ms but the software clock control indicated  $\sim 90$  ms of execution time from the opening to the closing of the laser shutter. While the measured scan time takes into account the communication

time between PC and laser unit ( $\sim 2/3$  ms each way), spiral scans can be improved towards a shorter execution. An external control on the galvo position would also be beneficial to keep track of the actual beam location.

As a next step, therefore, two-photon optogenetic stimulation of RGCs could be performed on genetically modified mouse from Thy1 line with spiral scans lasting  $\sim 20$  ms. A scan tailored to the cell morphology, which could be inferred via preliminary two-photon imaging, would also enhance the likelihood of successful stimulation.

An interesting experiment, which has not been pursued because of time constraints, would focus on the stimulation of cell types which are not accessible to visible optogenetic stimulation. For example, two-photon optogenetic stimulation could be instrumental in investigating the functional properties of amacrine cells, a sparse population of cholinergic neurons located above the ganglion cell layer which are hardly accessible with traditional methods. RGC response could be monitored while optogenetically stimulating amacrine cells with a NIR beam, in a two-photon fashion. This will lift the requirements of pharmacological blockers to avoid cross stimulation and will allow, if performed with a spatio temporal visual stimulus, to characterise the functional role of amacrine cells. For example, the role of starburst amacrine cells, might be investigated using a commercially available mice line (Chat-Cre) where these cells are marked with a fluorescent tag [116].

## Chapter 4

# Large scale matching of anatomy and function of retinal ganglion cells

The previous chapter reported on the integration between MEA recordings and two-photon excitation in retinal electrophysiology experiments. The main purpose of the chapter was to demonstrate that two-photon imaging can be combined with MEA recordings. This chapter, instead, focuses on MEA recordings experiments performed in combination with the  $\mu$ LED optogenetic stimulation setup described in chapter 2. This investigations were pursued to devise a novel, large-scale method that could link the information on morphology, genetic identity and neuronal spiking patterns towards the characterisation of RGCs.

### 4.1 Introduction

Insight on the links between morphology, function and genetic identity is pivotal in understanding the role of neurons in encoding and transmitting. However, electrophysiologists have long experienced the trade-offs between single-cell recording techniques, which are anatomically-accurate but non scalable, and high-density multi-cellular recording methods, which are affected by poor anatomical correlations. On the other hand, techniques like patch clamp [117] and calcium imaging [21] have allowed significant advances in the comprehension of the retinal architecture; nonetheless, they fail in delivering spiking activity data with high temporal resolution over a large number of cells.

A recent work [118] has reported anatomical identification of extracellularly recorded RGCs, where the spiking-induced electrical signature on an MEA (the Electrical Image, EI) was used to attribute electrophysiological signals to anatomical somas imaged in confocal microscopy. This approach, however, involves complex experimental procedures and this has motivated the development of an innovative and accessible method to match anatomy and function in the RGC layer.

This chapter presents a novel technique that addresses this central challenge by combining large-scale MEA recordings with precise anatomical and genetic identification. This method was developed in the mouse retina through optogenetic stimulation and subsequent confocal imaging of genetically targeted retinal ganglion cell sub-populations where a fusion protein ChR2-tdTomato was expressed. Namely, experiments were performed on retinas from Grik4-Cre, CRH-Cre and Thy1 mice lines [116, 119].

The method worked in consecutive steps. First, a visual characterization of RGCs was obtained illuminating the photoreceptor layer with spatio-temporal visual stimuli, while RGC spiking activity was recorded on a 512-channels MEA [2, 16]. This produced a set of electrical images for the recorded RGCs and allowed for a functional characterization of the cells, as described in section 4.3. The cells were then imaged in brightfield fluorescence on the MEA to register soma locations. At this stage, soma locations could not be unambiguously attributed to the EIs. To address this, the synaptic transmission within the retina was pharmacologically blocked as described in section 4.4. Then, highly-localised optogenetically-induced spatial receptive fields (OptoSTAs) were generated using a spatio-temporal optogenetic stimulation [7, 24, 31]. This stimulation was performed with a high power  $\mu$ LED array [120]. This produced a precise location for the soma and the optogenetically-induced EI, which matched the visually-induced spiking pattern. Moreover, optogenetic stimulation produced a new set of electrical images that were unambiguously linked with the position of the optogenetic receptive field.

As a result, it was possible to successfully match anatomical and functional identity amongst RGCs by applying strict significance cuts on the correlation between: (1) the spatial position of fluorescent cell somas and the optogenetically induced receptive fields and (2) the unique signatures of spiking activity (electrical images) induced on the MEA by visual and optogenetic stimulation. Finally, retinas were carefully removed from the array, fixed, and imaged in confocal microscopy.

## 4.2 Materials and methods

### 4.2.1 Animals

The experiments reported in the following paragraphs were conducted on retinal tissue from genetically modified mice. Animals were cared for and used in accordance with guidelines of the U.S. Public Health Service Policy on Humane Care and Use of Laboratory Animals and the NIH Guide for the Care and Use of Laboratory Animals. All procedures were performed in accordance with the UCSC Institutional Animal Care and Use Committee. Mice, purchased from Jackson Laboratories, were back crossed to C57Bl/6 lines and genotyped using DNA from a tail clip. Initial testing was done on Thy1-ChR-YFP strains (JAX 007615) that expressed ChR2 in many RGCs. Then, lines with a sparser ChR2 expression were used, namely CRH-ires-Cre (JAX 012704) and

Grik4-Cre (JAX 006474) after crossing them with a Rosa26-fsf-chR-tdTom strain (JAX 012567).

### 4.2.2 Retinal preparations

Eyes were enucleated from terminally anesthetized mice with an intraperitoneal injection of 16 mg/mL ketamine and 4 mg/mL xylazine in PBS, after 20 minutes of dark adaptation. The anterior portion of the eye and the vitreous were removed immediately after eye enucleation that, alongside retinal dissections, was performed under dim red light. Nasal-dorsal segment of the retinas were then dissected and placed flat on an extracellular micro-electrode array (MEA) with the RGCs side down. While recording, retinas were perfused with Ames' solution ( $34 \pm 2$  °C) bubbled with 95% O<sub>2</sub> , 5% CO<sub>2</sub>, pH 7.4.

### 4.2.3 Electrophysiological recordings

Electrophysiological recordings were performed on an MEA consisting of 519 electrodes with 30  $\mu$ m spacing [16]. The electrodes, arranged in an isosceles triangular lattice, covered an hexagonal region of approximately 0.43 mm<sup>2</sup> (450  $\mu$ m a side); 7 out of 519 electrodes were disconnected. Voltage signals induced on the electrodes by the action potentials released by RGCs were digitized at 20 kHz per channel with a custom designed integrated circuits and stored for offline data analysis, as previously described in [2]. Recordings were analysed in order to segregate spikes of different cells as described in [2, 3]. Briefly, spike candidates were revealed using an amplitude threshold on each electrode and comparing the spike-candidate voltage waveform with the traces on neighbouring electrodes across the same time window. Clusters of similar waveforms were then identified as neuron candidates with the algorithm described in chapter 3. Electrical images (EIs) of the recorded cells were calculated by averaging the voltage waveforms induced on all the electrode. As covered in chapter 3, for each spike a 5 ms time-window centred on the peak negative deflection of the voltage waveform was considered. A 2D plot of the maximal absolute voltage deflection at each electrode site was used as a spatial representation of the EI. After an initial recording of spontaneous activity, retinal segments were subjected to a stimulation protocol that combined visual and optogenetic stimulation to characterize RGC response. This procedure is covered in section 4.3 and 4.4.

### 4.2.4 Imaging

After recording, retinas were carefully removed from the electrode array, fixed for 30 minutes in 4% PFA and washed in PBS with 0.5% Triton X. Retinas were blocked for 1 day in the PBS and 3% donkey serum and incubated for 2 days at 4 C in block solution with primary antibodies against tdTomato and ChAT at 1:1000 dilutions. Retinas were then washed in PBS and incubated overnight in fluorescent conjugate secondary antibodies. Finally, the tissue was washed and

mounted on glass slides with Vectashield mounting medium. Retinas were imaged on a Leica SP5 Confocal microscope with a  $\times 60$  objective. Images were stitched using the FIJI plugin [95].

### 4.3 Functional characterisation of RGCs with visual stimulation

The experimental setup consisted of a 519 MEA electrophysiology system, a visual stimulation system and an optogenetic stimulation system integrated with an inverted microscope, as shown in figure 4.1. This setup was devised to allow not only for retinal stimulation and recording but also for retinal imaging. It is in fact possible to image the RGCs in epifluorescence by illuminating through the back of the array. The first step in the development of the proposed method was to demonstrate that visual stimulation of photoreceptors and direct optogenetic stimulation of RGCs can be combined to (a) characterise RGCs functional response and (b) to identify optogenetically-driven spiking units. To do this, a functional characterisation of RGCs with visual stimulation was performed first.

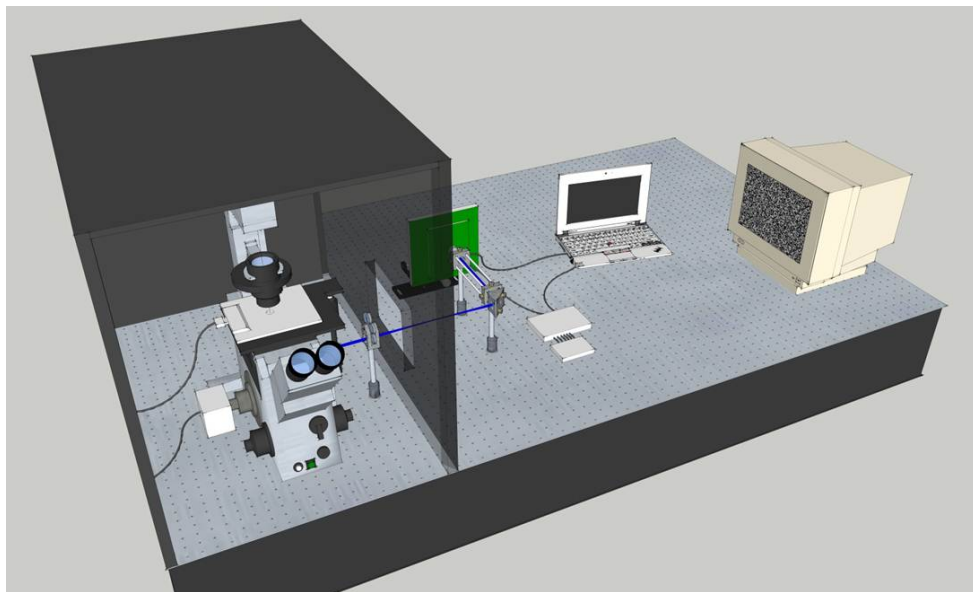


Figure 4.1: A diagram of the experimental setup, not to scale. The MEA array was mounted on an inverted microscope allowing for epifluorescence imaging from the back of the array. Visual stimulation was performed by projecting white noise frames generated on a computer monitor on the photoreceptors. Direct optogenetic stimulation of RGCs was obtained by projecting patterns of  $\mu$ LEDs selected on a  $\mu$ LEDs array via a 4f system.

MEA recordings combined with visual stimulation provide for an efficient method for large-scale characterisation of RGCs functional properties [2]. As described in chapter 3, it is possible to electrophysiologically identify single firing units and to compute an electrical image of the electrophysiologically identified RGCs. Visual receptive fields for each recorded cell can be characterized

by stimulating photoreceptors with a white noise movie composed of black and white checkerboard frames while recording from the RGCs [121]. Moreover, it is possible to characterise by illuminating the photoreceptors with a combination of moving gratings changing direction and speed. Figure 4.2 shows an example of visual stimulation for receptive field and direction selectivity characterisation.

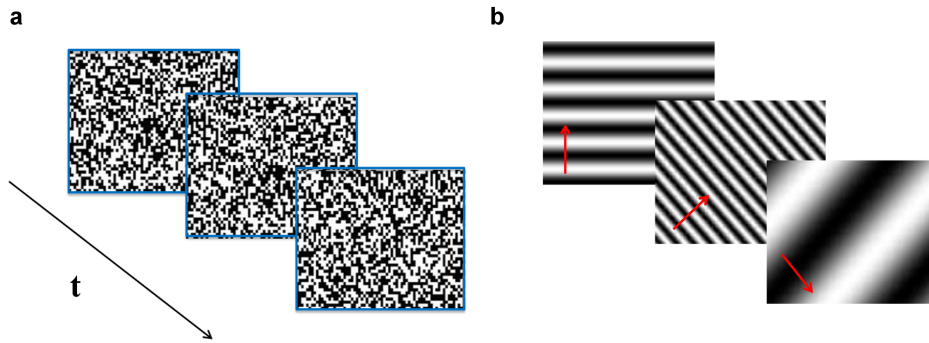


Figure 4.2: An example of visual stimulation frames. (a) a sequence of white noise frames from the binary white noise stimulus and (b) a sequence of frames from the moving bars stimulus where the red arrows indicate the direction of motion of the bars.

### 4.3.1 Visual receptive fields characterisation

Receptive fields are calculated from the average sequence of stimulating frames for each cells. This average, known as Spike Triggered Average (STA) calculated by triggering on each spike attributed to the cell. The STA yields information on the extent of the cell receptive field, on its temporal characteristic and on the ON/OFF polarity of the cell. For example an ON(OFF) RGCs will tend to respond to white (black) stimulating pixel in its receptive field; their STA, as a result, will exhibit a bright (dark) region that corresponds to the receptive field. The extent of the receptive field can be estimated with a fit on the spatial extent of this region.

A temporal characterisation of the cell response can be calculated by triggering on each spike and looking back at the average value of the stimulating pixels in the last 20 frames. This generates a response versus time plot known as time-course. Different cell families can be distinguished, for example, on their difference time-courses.

Figure 4.3 shows the visual STAs, the time course and the electrical image for an ON and an OFF RGCs. These were obtained with spatio-temporal white noise generated on a CRT monitor and projected on the photoreceptors with a stixel size of  $45 \times 45 \mu\text{m}^2$  and frame rate 60 Hz.

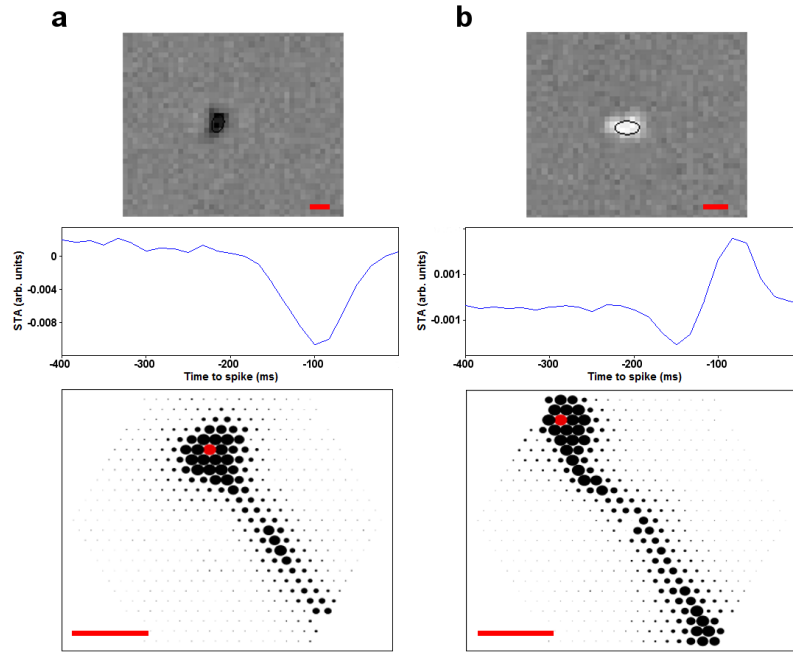


Figure 4.3: An example of functional characterisation of RGC visual response. (a) Top panel shows the averages stimulating frame calculated by triggering on a spike and computing the average of the pixel values in the last 20 frames preceding the spike. This process is known as Spike-Triggered Average (STA), and by extension, the average frame shown in the top panel is here referred to as visual STA. The middle panel shows the time course, namely the average value of the pixel within the cell's receptive field in the frames used to compute the STA. The bottom panel shows the electrical image of the recorded cell. The visual STA and the time-course characterize this RGC as an OFF cell; (b) As from the left side, the right side panels show visual STA, time course and electrical image for an ON RGC. Scale bars are 180  $\mu\text{m}$ .

### 4.3.2 Direction selectivity characterisation

Direction selectivity was characterized by calculating a Direction Selectivity Index (DSI) defined as

$$\text{DSI} = \frac{p - n}{p + n}, \quad (4.1)$$

where  $p$  and  $n$  are average spike rates;  $p$  corresponds to the average spike rate in the cell's preferred direction, and  $n$  corresponds to the average spike rate in the direction opposite to the preferred one. This means that a Direction Selective cells will have a DSI closer to 1, while a non Direction Selective cells will have a DSI closer to 0. In this work, cells were considered as Direction Selective if they had a  $\text{DSI} > 0.5$  in at least one of nine spatial/temporal combinations used for the moving gratings (spatial periods: 576  $\mu\text{m}$ , 1152  $\mu\text{m}$ , 2304  $\mu\text{m}$ ; temporal periods: 0.53 s, 1.07 s, 2.13 s). Typically, direction selectivity is graphically conveyed with polar plots of the spike rate versus the moving gratings inclination. Figure 4.4 shows an example of spike rate polar plots obtained for a Direction Selective RGCs in a Grik4-Cre retina.

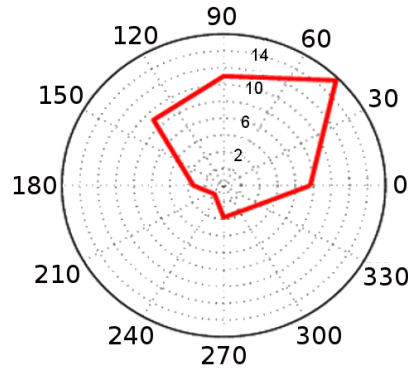


Figure 4.4: Polar plot of the spike rate of a direction selective RGCs in Grik4-Cre retina. The azimuthal coordinate represents the orientation of the moving gratings in deg. The radial coordinate represents spike rate. This plot was calculated for a stimulation with moving gratings at  $576 \mu\text{m}$  spatial period and 2.13 s temporal period. This cell had a direction selectivity index (DSI)  $>0.5$  in this spatio-temporal arrangements of moving gratings and was considered as direction selective (DS).

## 4.4 Optogenetic stimulation

After the visual stimulation runs were completed, visual response was blocked by a pharmacological cocktail (DNQX at  $150 \mu\text{M}$ , DL-AP7 at  $200 \mu\text{M}$ , L-AP4 at  $50 \mu\text{M}$ , Kynurenic acid at  $1 \text{mM}$ , Picrotoxin at  $50 \mu\text{M}$ , and Strychnine at  $50 \mu\text{M}$ ) washed in through the perfusion system. This step was taken in order to avoid any contamination between visual and optogenetic responses. No visual artefact was observed after washing in the pharmacological cocktail. Retinas were then imaged by illuminating through the back of the MEA. An image of a Grik4-Cre retina on the MEA is shown in figure 4.5. The bright soma in the fluorescence image belong to RGCs that express ChR2 and the targeted Grik4 gene. This images gave the positions of ChR2-expressing cells with respect to the electrodes.

While the photoreceptor response was pharmacologically blocked, sparse white noise optogenetic stimulation of ChR2-labelled RGCs was performed by projecting blue LED pixels from a  $16 \times 16$  high-intensity  $\mu\text{LED}$  array [120].

The  $\mu\text{LED}$  array was imaged and focused on the RGC layer, through the back of the MEA, with a 4f optical system shown in figure 4.6. Squared LED pixels,  $100 \mu\text{m}$  side, were optically reduced to  $\sim 23 \times 23 \mu\text{m}^2$  in size and focused on the RGC layer for 50 ms-long pulses refreshed every 100 ms at  $\sim 10 \frac{\text{mW}}{\text{mm}^2}$ . An example of projected pixels is shown in figure 4.7. Action potentials from ChR2 expressing cells were elicited by projecting flashes of repeating arbitrary pattern or random sequences of single pixels (a sparse white noise). An example of sparse white noise frames is shown in figure 4.8. Optically induced electrical artifacts, associated with the photoelectric effect, are

common with optogenetic stimulation and, typically, complicate spike detection. Interestingly, no light-induced artifact associated with the onset/offset of blue light was observed in the physiological recordings (figure 4.9).

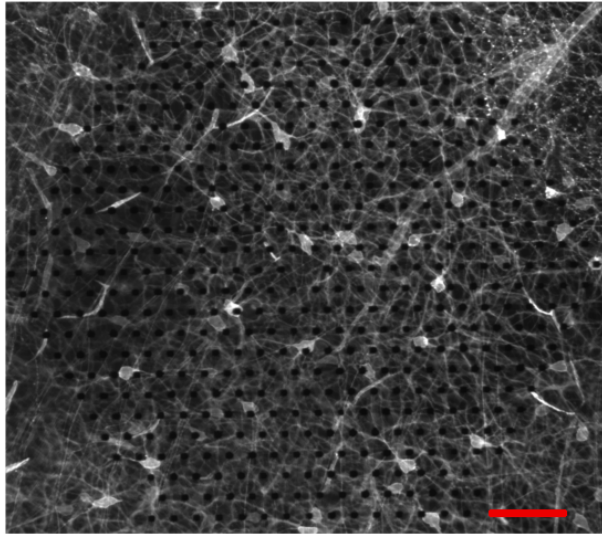


Figure 4.5: Epifluorescence image of a section of Grik4 retina mounted on the MEA. The black circles are the electrodes, the bright cells bodies are ChR2-transfected RGCs that express Grik4 gene. Scale bar is 100  $\mu\text{m}$ .

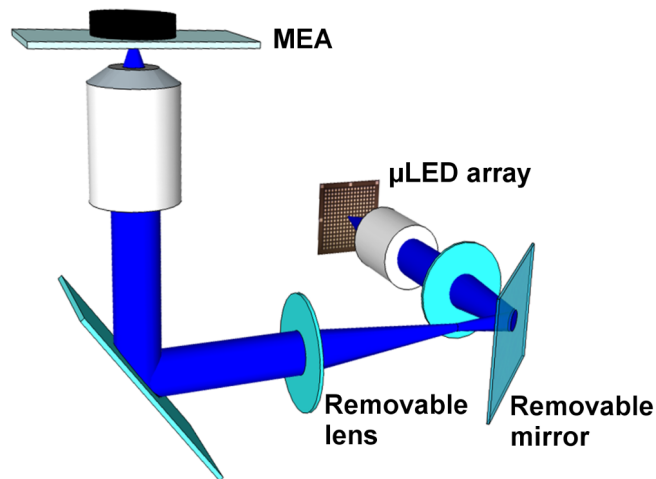


Figure 4.6: Diagram of the optical system used to project the  $\mu\text{LED}$  pixels on the MEA. LED lights was collected with a  $\times 4$  objective relayed with two lenses in a  $4f$  system and projected to the electrodes plane with a  $\times 20$  objective. The relay system used a removable mirror and a removable lens to allow for visual stimulation to be follow the same optical path, as shown in figure 4.1.

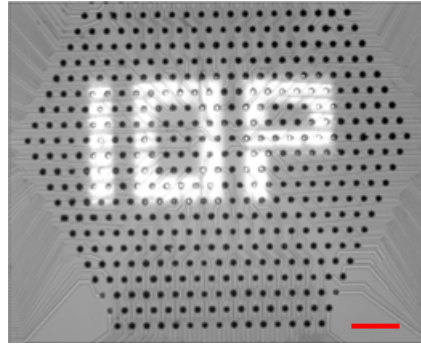


Figure 4.7: The figure shows a pattern of  $\mu$ LED pixels projected on the 519 MEA. The black circles are the electrodes. Scale bar is 90  $\mu$ m.

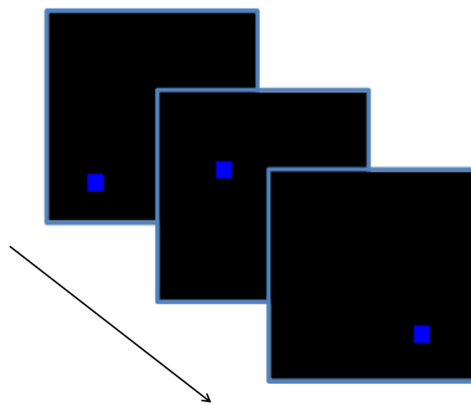


Figure 4.8: The figure shows a diagram of a sparse white noise stimulus obtained by selecting a single pixel at a time on the LED array. This stimulus was used to generate optogenetically-induced receptive fields.

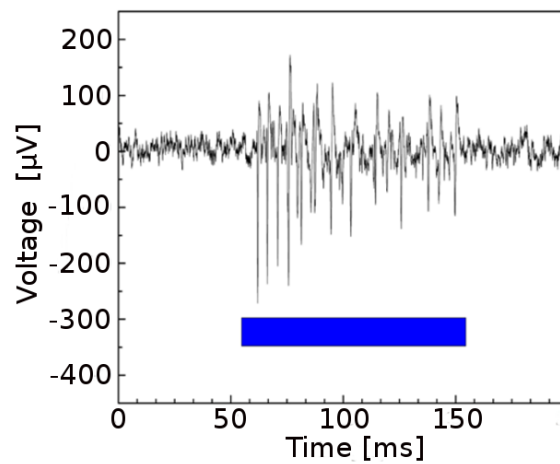


Figure 4.9: The figure shows an optogenetically induced spike burst. The blue bar represent the duration of the light stimulus. No artifact connected with the onset/offset of the blue light was observed. It is interesting to note how the spike amplitude diminishes during the burst.

#### 4.4.1 Optogenetically induced spatial receptive fields

By segregating the optogenetically elicited spikes, it was possible to successfully identify firing units and calculate optogenetically-evoked electrical images. In order to locate the soma position of ChR2-expressing cells, optogenetically-induced spatial receptive fields were generated by reverse-correlating spike times with the spatio-temporal  $\mu$ LEDs stimulation sequence. In a similar fashion to the visual STA, an average sequence of stimulating frames preceding a spike was calculated for each recorded cell. Averages were computed over a statistical ensemble of stimulating frames selected using each spike attributed to a cell as a temporal trigger. This produced Optogenetically-induced Spike-Triggered Averages (OptoSTAs) that appear in the  $\mu$ LED array map as bright pixel centred on the cell soma as shown in figure 4.10 and figure 4.11. OptoSTA receptive fields were highly localised with an average area of  $(1.8 \pm 0.1) \cdot 10^3 \mu\text{m}^2$  (5 experiments, 70 cells), an order of magnitude smaller than the average area calculated for Visual STAs,  $(3.3 \pm 0.2) \cdot 10^4 \mu\text{m}^2$  (4 experiments, 857 cells). This highly localised response of the RGCs suggests the direct optogenetic activation of the cells. Using the array of electrodes as a reference, it was possible to retrieve the OptoSTAs location with respect to the cells by imaging the retinas and registering the projected  $\mu$ LED position with respect to the electrodes.

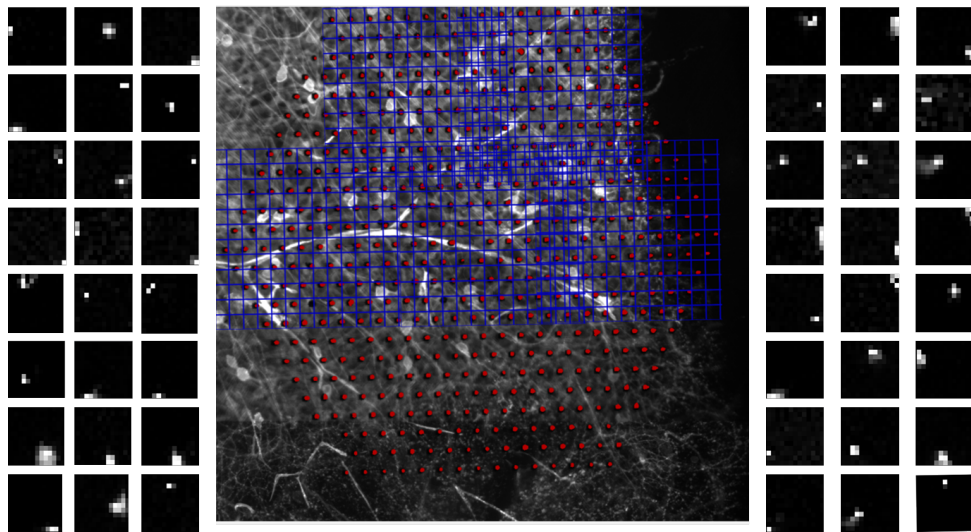


Figure 4.10: The figure shows an example of the many OptoSTAs generated in a single Grik4Cre retina preparation. The central panel displays the retina mounted on the MEA with electrodes outlined in red. The blue grids overlaid on the retina indicate the five areas stimulated with the  $\mu$ LED array. The OptoSTAs generated during the experiment are arranged around the central panel in no particular order.

#### 4.4.2 Optogenetic identification of RGCs

The highly-localised optogenetically-induced spatial receptive fields can serve as an unambiguous indicator for localising the soma of a cell recorded on the array. In order to test whether an

unequivocal spatial correlation between OptoSTAs and anatomical somas could be established, the described method has been applied on retinas sparsely expressing ChR2-tdTomato in the ganglion layer (5 preparations: 1 CRH-ires-Cre, 4 Grik4-Cre). As shown in figure 4.11, the spatial positions of OptoSTAs are highly correlated with the spatial locations of ChR2-expressing RGC somas and so allow anatomical identification of electrophysiologically recorded RGCs.

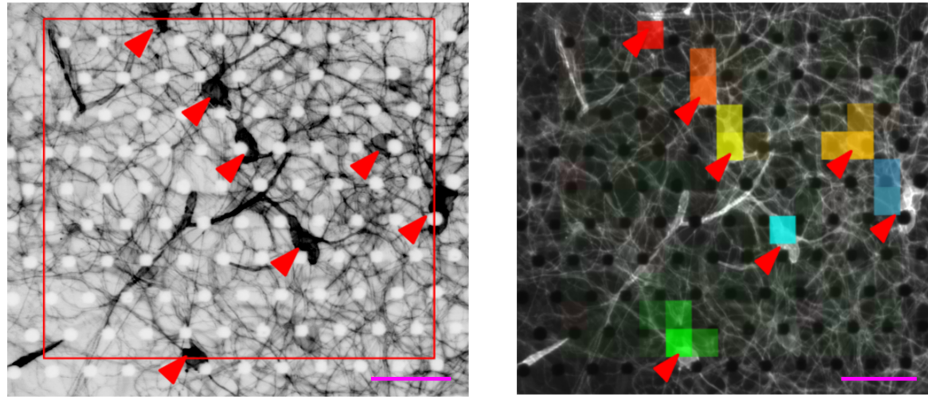


Figure 4.11: *Left*, fluorescence image of RGCs from Grik4-Cre (grey look up table); stimulated area is outlined in red ( $\sim 280 \times 300 \mu\text{m}^2$ ), cells are indicated by red arrowheads. *Right*, coloured OptoSTAs are overlaid on the somas shown in left panel: each OptoSTA identifies a cell by associating its location with the electrophysiological recordings; scale bars are  $60 \mu\text{m}$ .

The correlation between OptoSTAs and RGC's soma positions can be quantified by calculating the distribution of the distances from the OptoSTA location for each recorded cell to the cell body of the nearest fluorescent cell.

Over 5 preparations and a total of 11 optogenetic stimulation runs,  $\sim 120$  ChR2-expressing cells were illuminated leading to 85 electrophysiologically identified neurons (post-spike sorting) with an OptoSTA.

As shown in figure 4.12, nearly half of the fluorescent cells ( $45 \pm 5\%$  standard error on the mean) fall within 1  $\mu\text{LED}$  pixel distance from an OptoSTA. The location of the OptoSTAs were defined by computing a centre of gravity fit; cell position was estimated by the centroid of an ellipse encircling the cell body. An example is shown in figure 4.13. Any cell whose soma fell mostly outside the stimulation area was dismissed from the analysis *a priori*. To corroborate the evidence of the match between labelled and recorded cells, the fluorescent cells for which the axon could be traced were found. As a sanity check, the axon trajectory was then matched to the electrical signature of the axonal trajectory of the recorded cell: an example is shown in figure 4.14.

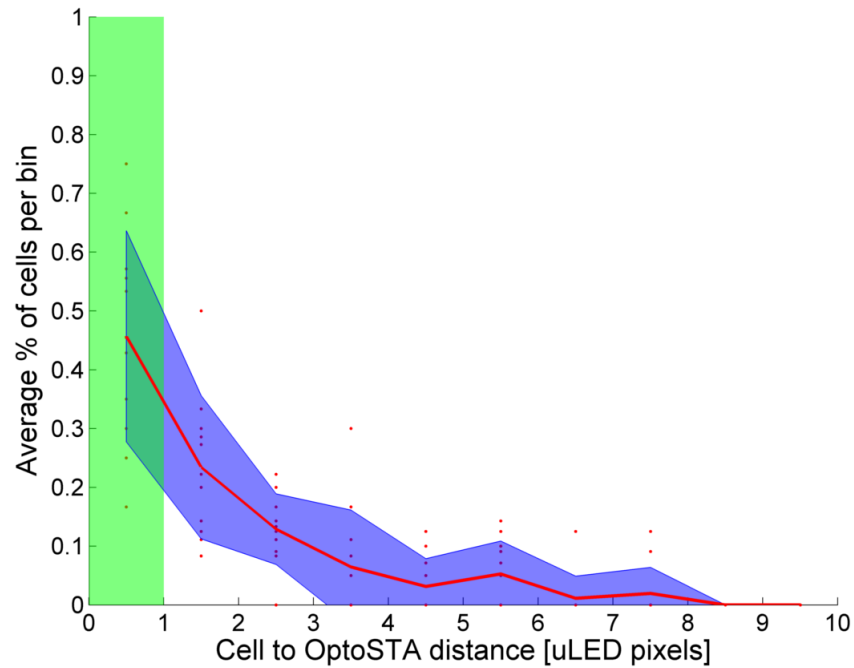


Figure 4.12: Histogram of the distances from the OptoSTA location of each recorded cell to the cell body of the nearest fluorescent cell. Cells within 1  $\mu\text{LED}$  pixel from an OptoSTA fall in the green shaded area; single experiments are represented as red dots while standard deviation across datasets (11 across 5 experiments) is outlined in blue.

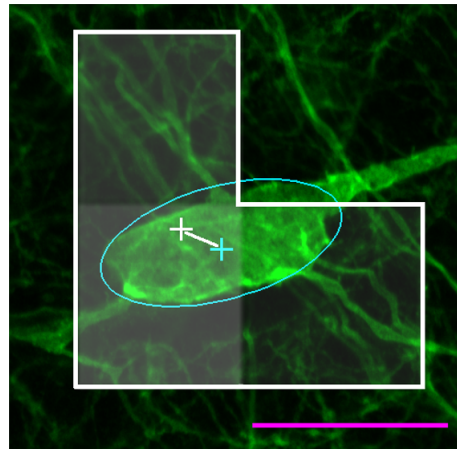


Figure 4.13: An example of a good match of OptoSTA and anatomical soma. The OptoSTA outline is shown in white, while its centre of gravity is indicated by the white cross. The manually defined ellipse encircling the cell is shown in cyan as is the centroid of the ellipse. The distance from the OptoSTA centre of gravity to the centroid of the ellipse is closer than the projected LED pixel side. Scale bar is 25  $\mu\text{m}$ .

Only a few cells (5-10) were found where axons were clearly attributable to a soma in the fluorescence images. This gives further motivation to the development of the OptoSTA technique, which does not rely on axon tracing. While the described approach ensures that OptoSTAs are only generated for Chr2-tdTomato positive cell, the finite projected  $\mu\text{LED}$  pixel size (23  $\mu\text{m}$  side) leads to

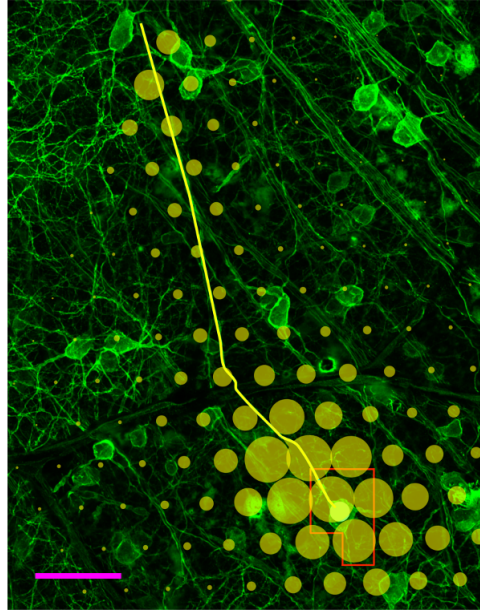


Figure 4.14: An example of electrical image matching the associated cell's axon trajectory. The electrical image is indicated in shaded yellow and overlaid to a confocal image of the retina. The anatomical axon trace is drawn in solid yellow and follows the the axonal part of the electrical measurement. The outline of the OptoSTAs is indicated in orange. Scale bar is 60  $\mu\text{m}$ .

ambiguity in the match between OptoSTAs and fluorescent cell bodies when two or more labelled cells fall under the same pixel. Examples of this ambiguity are displayed in figure 4.15.

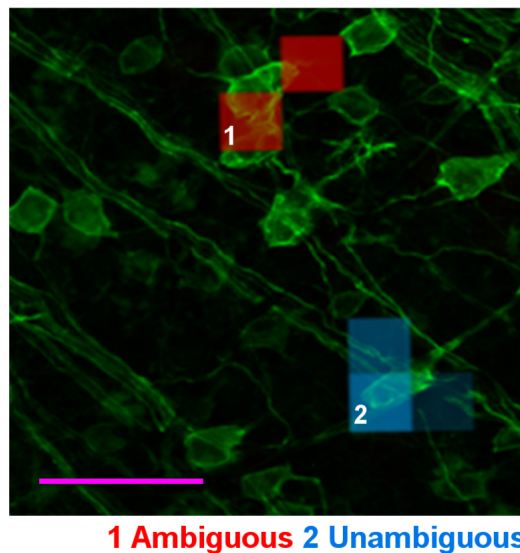


Figure 4.15: An example of accepted and discarded optogenetic identification. It is not possible to understand to which cell the red OptoSTA should be attributed. This match, therefore, was discarded. Conversely, the blue OptoSTAs is unambiguously matched to a unique cell. Scale bar is 60  $\mu\text{m}$ .

This could be sorted by manually monitoring OptoSTAs to check if they generate a satisfying match with the Chr2-expressing cell. However, applying such an approach over tens or hundreds of cells is time consuming and might suffer subjective biasing. A cuts based analysis, instead, is a convenient approach to objectively discriminate whether a match between an OptoSTA and a Chr2-expressing cell could be unambiguously established with an automated approach. In order to objectively validate unambiguous matches between OptoSTAs and Chr2-expressing cells, the distances between each OptoSTA and the neighbouring cells were considered. All the OptoSTAs with more than 4 active pixels were dismissed, as these are difficult to assign to a fluorescent soma. For each OptoSTA, the distances to the nearest and second-nearest labelled cell body were plotted against each other as shown in figure 4.16. Then an additional cut was introduced.

Given an OptoSTA, let  $D1$  be the distance to the closest cell,  $D2$  be the distance to the second closest cell and  $L$  be the lateral dimension of a projected  $\mu$ LED pixel ( $23 \mu\text{m}$ ). Any OptoSTAs-cell pair with  $0 < D1 < L$  and  $D2 > D1 + L$  was considered an “unambiguous match”. This acceptance area is coloured green in figure 4.16. No match could be established for pairs lying in the region next to the origin,  $0 < D1 < L$  and  $0 < D2 < L$ , which was defined as a rejection area. A transition region,  $0 < D1 < L$  and  $L < D2 < D1 + L$ , exists between the areas of acceptance and rejection where ambiguous and unambiguous matches are contiguous, as we could observe with a case-by-case analysis. In order to avoid any weak match, all pairs lying in this area were discarded.

Starting from 70 recorded RGCs with good OptoSTAs (over 5 experiments), 30 of them could be linked to Cre-targeted anatomical RGCs. It should be noted that a higher density of Chr2-expressing neurons resulted in a higher rejection rate. Comparing two experiments performed on different genetic lines, it was found that stimulation runs over 5 areas of a Grik4-Cre retina, targeted an average of 14 cells per stimulation area (70 cells in total) and resulted in 12 rejections. At the same time, stimulation runs over 3 areas in a CRH-Cre retina, targeted an average of 9 cells per stimulation area (27 in total) and resulted in 3 rejections.

Visually and optogenetically induced electrical images were compared for the subset of the cells with good OptoSTAs. As reported in the next section, this technique allowed the establishment of a link between genetic identity and visual function. In conclusion, this section demonstrated that a sparse-white-noise optogenetic stimulation approach allows linking electrophysiologically identified cells with their anatomical soma.

## 4.5 Matching morphology, function and genetic identity

The electrical images can be exploited to find the visual response properties of the Chr2 positive cells identified in the previous section. The EI of a cell is the unique electrical footprint of the RGC’s spiking activity recorded on the MEA, a measurement that is independent of the method of stimulation. Therefore, genetic identity, soma location and the visual response properties of the

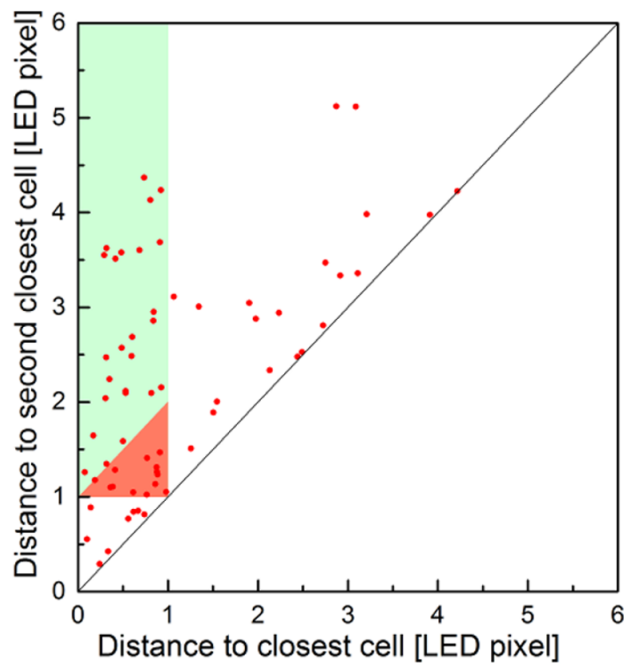


Figure 4.16: Scatter plot (5 experiments) of OptoSTAs' centres of gravity distance from the closest (x axis) and second-closest (y axis) ChR2-expressing cells. Distances are indicated in LED pixel size. Data points falling in the green-coloured area ( $x < 1$ ,  $y > x + 1$ ) represent unambiguous optogenetic identification. Data points falling in the orange and white areas have not been considered successful matches for optogenetic identification.

RGCs can be connected by matching optogenetically-elicited and visually-elicited EIs in the same preparation.

### 4.5.1 Matching morphology and function

This was achieved by cross-correlating the optogenetically-elicited EIs with their visual counterparts. In particular, optogenetically-elicited EIs of the RGCs that had good OptoSTAs were compared with visually-elicited EIs of the RGC's recorded prior to the application of neurotransmitter blockers. All possible pairs of the EIs were considered and for each pair the degree of similarity was calculated as the normalised inner product between the two EIs. The inner product was calculated as

$$\text{IP}(\text{EI}_1, \text{EI}_2) = \frac{\sum_e O_e \cdot V_e}{\sqrt{\sum_e O_e^2 + \sum_e V_e^2}}, \quad (4.2)$$

where  $O_e$  and  $V_e$  are optogenetically and visually evoked average spike amplitudes, recorded on each electrode  $e$  with  $\text{SNR} > 10$ , normalised to the maximum amplitude detected in the EI. This normalisation was done to make the comparison depend more on the shape of the EI and less on the overall amplitude. Similar EIs with the inner product value close to 1 corresponded to the same RGC recorded across the two datasets (optogenetically-induced and visually-induced). An inner product closer to 0 pointed to a pair of dissimilar EIs corresponding to two different RGCs. The correlation between a pair of EIs was used as the criteria for acceptance. More precisely, let  $C_{1,2}$  denote the correlation between  $\text{EI}_1$  and  $\text{EI}_2$ ; then let  $C_{1,n}$ ,  $C_{2,m}$  be the correlation between each of the paired EIs and their respective second closest EI. Then, the original pair of EIs was accepted as a match if  $C_{1,2} > 0.95$  and  $C_{1,n} < C_{1,2} - 0.05$ ,  $C_{2,m} < C_{1,2} - 0.05$ .

Examples of successful EI correlation and consequent matching of anatomy and function are shown in figure 4.17. As shown in figure 4.17, the validity of the EI matching process was demonstrated by comparing the full voltage waveforms on select electrodes. It is important to note how this method, by exploiting the spatial information encoded in the OptoSTA, allows an unambiguous match between electrical images and anatomical somas without the laborious procedure of quantitative morphological validation.

### 4.5.2 Matching genetic identity and function

The retinas were then imaged on a confocal microscope at  $\times 60$  magnification. Figure 4.17 shows examples of the spatial correlation between the somas of the labelled RGCs and the OptoSTAs of the matched RGCs recorded on the MEA. It was not possible to reconstruct the dendritic tree of individual RGCs due to the density of the labelled cells in both CRH-Cre and Grik4-Cre retinas. and

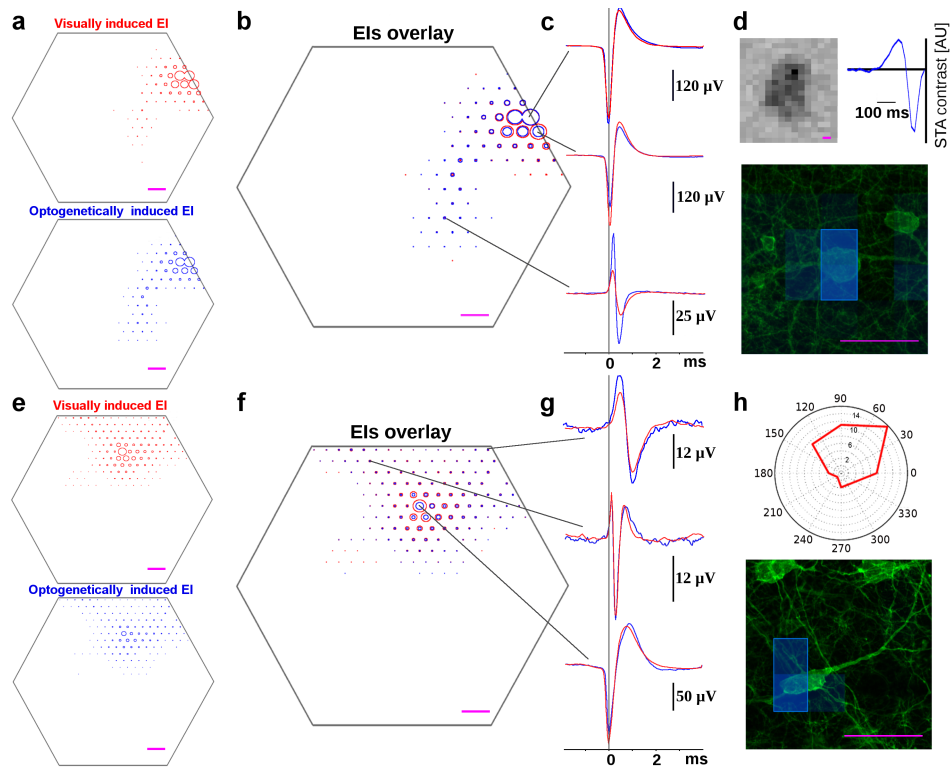


Figure 4.17: Matching morphology and function. (a) Visually induced EI, top, and optogenetically induced EI, bottom, for a CRH-Cre-ires RGC; the MEA is outlined in grey (b) Overlay of EIs: optogenetically induced EI in blue and visually induced EI in red. (c) Comparison of spike waveforms recorded across the MEA: optogenetically induced trace in blue and visually induced trace in red. (d) *Top*, visual response: OFF receptive field and temporal filter; *bottom*, confocal image with outlined OptoSTA. (e) Visually induced EI, top, and optogenetically induced EI, bottom, for a Grik4 RGC; the MEA is outlined in grey. (f) Overlay of electrical images: optogenetically induced EI in blue and visually induced EI in red. (g) Comparison of spike waveforms recorded across the MEA: optogenetically induced trace in blue and visually induced trace in red (h) *Top*, visual Direction Selective response; *bottom*, confocal image with outlined OptoSTA, bottom. All scale bars are 50  $\mu$ m.

In order to measure the functional properties of the Grik4-positive RGCs, the analysis was focused on the single best Grik4-Cre recording in order to analyse DS response following a previously described approach [122]. In this experiment, 70 fluorescent cells were within the field of view of the  $\mu$ LED array, and 40 OptoSTAs were generated. EI-correlates for 13 of these cells were found in the data run where retinal responses to moving gratings were recorded. Almost all of these cells (12/13) had  $DSI > 0.5$ . This means that the majority of Grik4-Cre expressing cells was direction selective. In contrast to this, only 20 % (64/314) of all visually responsive RGCs identified in the same recording had a direction preference. Figure 4.18 shows the distributions of DSIs for visually and optogenetically active cells in the first two panels. Furthermore, while DS RGCs sensitive to all four cardinal directions were present in the recording, Grik4-positive RGCs were mostly selective for the motion towards the nasal part of the retina. In other words, visual stimulation elicited direction selective responses in all the cardinal directions (25 dorsal, 20 nasal, 14 ventral and 5 temporal); conversely, optogenetic stimulation generated responses mainly from the nasal direction (1 dorsal, 9 nasal, 1 ventral and 0 temporal). This was measured by calculating a DS vector for each DS cell as defined by Elstrott et al.[122]. Briefly, on a given presentation of the stimulus the response to motion in each direction was normalized to the total number of spikes elicited during that repetition across all directions. The normalized vectors from all directions were then summed in a vector sum for each repetition. The average of the vector sums across repetitions generated the preferred direction vector. These vectors are displayed in figure 4.18 for visually and optogenetically activated cells. The statistical significance for the observed preferred nasal response in Grik4-positive DS cells shown in figure 4.18 was tested with Student statistic against the null hypothesis of no preferred direction. If Grik4-positive DS cells were expressed homogeneously in the four directions, the differences in cell counts should be accounted on a limited optogenetic stimulation efficiency. This efficiency was estimated from the counts in the nasal direction as  $\varepsilon = 9/20$ . If the null hypothesis were true, when taking into account the optogenetic efficiency scaling, the average difference of cell counts between visually stimulated and optogenetically stimulated DS cells should be compatible with 0. Differences in dorsal (ventral or temporal) directions were calculated as

$$\Delta = D_v \cdot \varepsilon - D_o, \quad (4.3)$$

where  $D_v$  is the number of visually elicited dorsal (ventral or temporal) DS RGCs,  $\varepsilon$  is the assumed optogenetic stimulation efficiency and  $D_o$  is the number of optogenetically elicited dorsal (ventral or temporal) DS RGCs. A Student test was calculated as follows

$$t = \frac{\Delta - 0}{\sigma / \sqrt{n}} = 2.16, \quad (4.4)$$

where  $\Delta$  is the average difference over dorsal, temporal and ventral direction,  $\sigma$  is the estimated standard deviation and  $n=3$  is the number of samples. The null hypothesis can therefore be rejected with  $t > 2.1$  at  $\alpha = 0.05$  significance with 4 degrees of freedom. It must be noted that these results

were obtained without imposing the strict cuts on the spatial match between OptoSTAs and the labelled RGC soma locations. These cuts would have decreased the initial pool of 40 RGCs with good OptoSTAs to 14. Therefore, the requirement of spatially identifying the exact labelled cell reduces the efficiency of the described approach. However, if the aim is simply to attribute function to a genetic sub-class of neurons, then the previous set of statistics stand.

This technique was tested in a different genetic line, CRH-ires-Cre. A region covering 26 fluorescence cells was illuminated and 11 OptoSTAs were obtained. From these OptoSTAs, 11 optogenetically-induced EIs were produced that matched to 8 visual EIs (3 OFF cells, 4 ON cells and one with no defined visual response). 3 of these cells were matched to a visual OFF response. No match of CRH cells with DS response was found.

## 4.6 Discussion and conclusions

The chapter described a method to associate functional data from large-scale electrophysiological recordings with genetically labelled RGCs in mice. Besides, it shows how spatio-temporal optogenetic stimulation can be employed to generate highly-localised receptive fields that unambiguously identify individual cells. Such an experimental protocol can be combined with a functional characterisation procedure based on the presentation of spatio-temporal visual stimuli. Furthermore, visual characterisation and optogenetic identification do converge, in a single analytic framework, allowing a correlation of morphology and function in the recorded neural population.

Optogenetically-induced receptive fields have been generated by showing a random sequence of single  $\mu$ LED pixels in the retinal ganglion layer. These receptive fields corresponded to the spatial locations of the Chr2-expressing cells visualised by fluorescent microscopy. This correspondence allowed to link the individual electrophysiologically recorded RGCs to the single cells within a genetically targeted sub-population. The described technique is accessible and versatile being based on a simple optical architecture.

However, as shown, not all the Chr2-expressing cells have an associated OptoSTA. This can, perhaps, be attributed to three factors. Firstly, the limited photosensitivity of Chr2-expressing neurons in the Ai27 line might have affected the stimulation efficiency [123]. Further investigations with Ai32 mice are expected to give better results. Secondly, it is not unreasonable to assume that a small portion of the Chr2-expressing cells may have gone undetected despite the high-density MEA. Thirdly, the well-recognised limitations of current spike-sorting algorithms [110] removes a number of cells, due to classification effects such as cross-contamination between single units. For example,  $\sim 40$  neurons with good OptoSTAs were rejected out of the  $\sim 130$  identified across 5 experiments due to this type of contamination. Advances in spike sorting will undoubtedly help improve the statistics. The rigorous significance cuts applied during optogenetic identification explain why

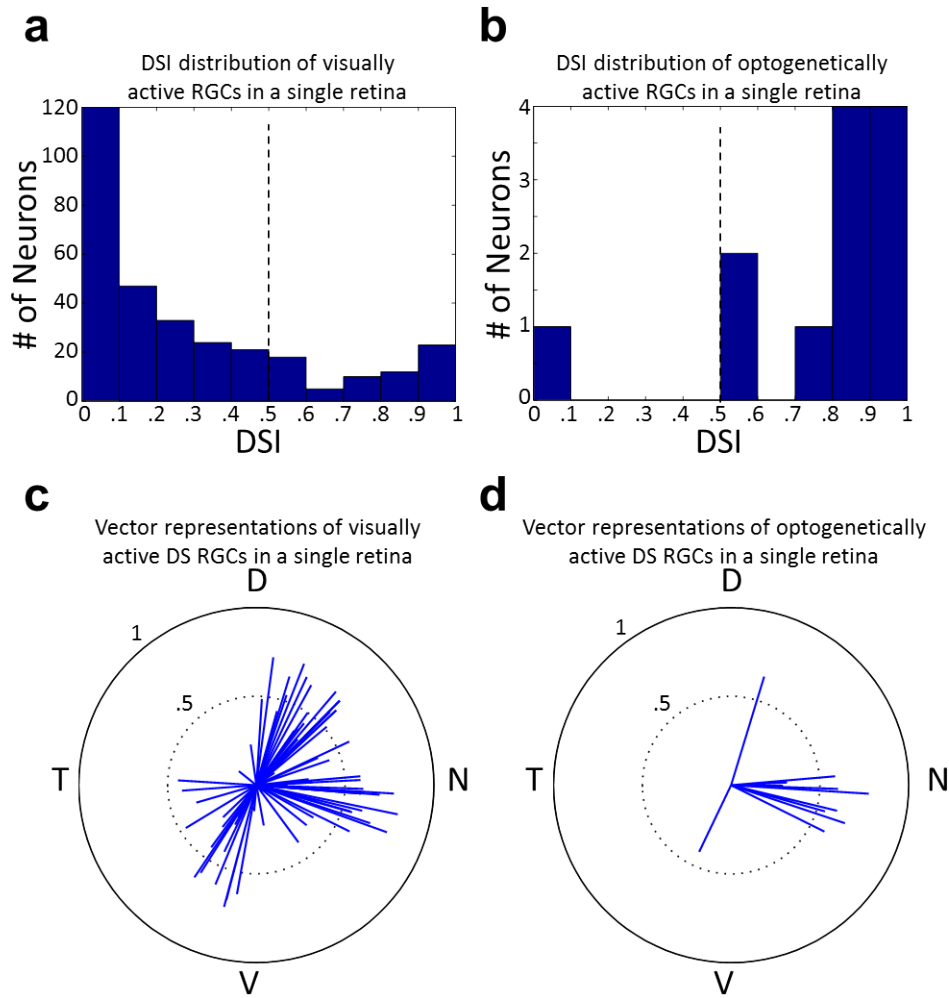


Figure 4.18: The figure summarises the analysis on functional properties of Grik4 RGCs. Optogenetically active cells represent a biased subset of the visually active cells in the Grik4-Cre mouse line. Panel (a) shows the distribution of DSIs for all visually active cells in a single retina (314 visually active RGCs). Panel (b) shows the distribution of DSIs for optogenetically active cells in the same retina (12 optogenetically active RGCs). Panel (c) displays DS vectors for all visually active cells with DSI > 0.5 in a single retina (64 DS RGCs). Panel (d) shows DS vectors for all optogenetically active cells with DSI > 0.5 in the same retina (11 DS RGCs).

only around a third of the cells with an overlaying OptoSTA have been accepted as unambiguously identified. The optogenetic identification might be enhanced by increasing the statistics of detected spikes with a higher number of stimulation cycles (300-500) in the same timeframe.

Large-scale matching of anatomy and function has been demonstrated by correlating the unique signatures of spiking activity induced on the MEA. This spiking signature are stimulus-independent. As shown in figure 4.9 and previously observed [124], spike amplitude tends to diminish during an optogenetically excited burst, potentially leading to smaller average amplitudes in the electrical image. We therefore chose a loosely scale-dependent parameter (inner product) to correlate EIs. However, while the amplitude of optogenetically and visually induced spikes might differ, the high temporal correlation of spike waveforms (figure 4.17) gives further reassurance of exact matching. As reported in the result section, strict significance cuts were applied to guarantee for a unique match. Relaxing these statistical constraints as well as using alternative methods for finding spikes associated with unique neurons across varying stimulation conditions could be investigated in order to optimise the method.

The anatomical identification of extra-cellularly recorded RGCs in primate has been recently reported in a study by Li et al. [118], who demonstrated a different approach, which relied on the information contained in the electrical image alone. The present method adds to this work without involving experimentally challenging procedures like axon tracing, complex immuno-histochemical staining or morphological identification of recorded cell types, a task which requires extensive expertise. Moreover, the present method has a second advantage. If the OptoSTA receptive field overlaps with the single labelled cell soma and no additional labelled cells are nearby, then the match between the electrophysiologically identified cell and the anatomical cell soma is unambiguous. This happens because all nearby RGCs lack ChR2 and would not respond to the optogenetic stimulation. Conversely, there is no such certainty when matching electrophysiology to labelled RGCs using only electrical images. In this case, one has to rely between the EI axonal trajectory and the labelled cell's axon. Unfortunately, axonal trajectories are often elusive. The present methods, therefore, is advantaged as it avoids these limitations. Nonetheless, the two experimental paradigms are not mutually exclusive and can be combined. For example, even if a few ChR2-expressing cells are located next to each other, but their individual axons can be traced, the correlation of the axons with the axonal trajectory of the EI of the candidate optogenetically activated RGC can be used to resolve the ambiguity.

The described technique is a promising tool for a comprehensive functional characterisation of already described and newly discovered anatomical and molecular RGC types. In fact, the method can be employed across a wide range of expression patterns of ChR2 in RGCs. For example, the reporter employed in this study (a Cre-dependent ChR2-tdTomato fusion protein at the Rosa26 locus) could be combined with virally expressed Cre-recombinase for random and sparse labelling [119]. A diverse and valuable approach would focus on a sparse labelling technique obtained with

a viral reporter [125].

The density of expression of ChR2 is a key parameter that must be considered while designing an experiment that applies the reported technique in the characterisation of a particular genetic model. The closest distance at which two ChR2-expressing cells can be resolved by their OptoSTAs is dictated by the size of the projected pixels, as shown in figure 4.15. Adjustments in this direction can be readily made by using smaller light sources [126] or by optically reducing the size of the projected  $\mu$ LEDs. Currently this results in a trade-off between resolution and the size of the stimulated area. However, on-going developments of larger format  $\mu$ LED arrays promises larger area stimulation at higher resolution with the potential to address this issue.

Finally, the generation of cellular specific optogenetically induced spatial receptive fields might serve as a valuable tool while investigating connections between anatomy and function in neural circuits other than the retina.

### **Acknowledgements**

This chapter reports on research performed in collaboration with N. McAlinden and K. Mathieson from the Institute of Photonics, University of Strathclyde, and E. Zampaglione, J. Roebber and A. Sher from Santa Cruz Institute of Particle Physics, University of California Santa Cruz.

## Chapter 5

# Discussion and conclusions

This thesis reported on the development of an experimental tool to interface with intact neural populations in the mammalian retina. This tool was designed to record, image and stimulate genetically targeted neurons with single-cell precision and ms temporal resolution. This was done starting from an existing electrophysiology system based on a MEA fabricated in ITO. The MEA system was integrated with a custom two-photon microscope and an optogenetic stimulation setup based on a  $\mu$ LED array. This work led to:

- the construction and validation of a setup combining large scale electrophysiology, two-photon microscopy and spatio-temporal optogenetic stimulation
- the demonstration of a novel, large-scale method to link anatomy, function and genetic identity in RGCs populations that exploits MEA recordings and spatio-temporal optogenetic stimulation with  $\mu$ LEDs.

The integration of MEA recordings with two-photon excitation presented significant challenges connected with the interaction of high-intensity laser pulses and the MEA. These difficulties constitute a drawback of two-photon excitation when compared with a single-photon approach. As shown, standard bright field imaging and visible optogenetic stimulation lead to a novel method for RGCs characterisation. However, single photon techniques are limited to the ganglion cell layer and have to be coupled with pharmacological inhibition of photoreceptors when targeting RGCs for optogenetic stimulation. Two-photon excitation, on the other hand, can overcome these limitations and this work demonstrated its combination with MEA recordings.

The described setup, which allows for both illumination techniques, is a flexible tool that can potentially be employed in diverse investigations of neural circuits.

The following sections will summarise and discuss in greater detail the construction of the microscope, its integration with the MEA system and the optogenetic stimulation experiments with  $\mu$ LEDs.

## 5.1 Two-photon microscope

A custom two-photon microscope, described in Chapter 2, was built from a femtosecond pulsed laser oscillator (Mai-Tai, Spectra Physics) using a raster scanning system implemented with galvanometric mirrors. A custom software platform was developed in LabView to control laser scanning, data acquisition and image acquisition. As previously detailed, a custom written software was preferred over existing open-source platforms (e.g. [94]) to guarantee for flexibility in the integration of imaging protocols with electrophysiological recordings.

In order to reach the retinal tissue while imaging through the MEA, the microscope was equipped with a  $\times 20$ , 0.5 NA objective lens with a 2.1 mm working distance. This choice is a trade-off between working distance, NA and cost. The microscope was also equipped with a  $\times 100$ , 1.3 NA oil-immersion objective which can be used for standard coverslip mountings.

The microscope system was characterised and validated by imaging reference samples (e.g. fluorescent micro- and nano-spheres) and sections of neural tissue. The microscope can successfully acquire images from retinal sections and brain slices expressing genetically targeted molecular markers, with both objectives and no staining enhancement. Optical resolution was estimated by measuring the intensity PSF for the two different objective lenses. While the  $\times 20$ , 0.5 NA objective showed less than ideal performances ( $r_{x-y} = 2.0 \pm 0.5 \mu\text{m}$  and  $r_z = 13 \pm 2 \mu\text{m}$ ), the  $\times 100$  1.3 NA objective produced optical resolution in agreement with expectations ( $r_{x-y} = 0.48 \pm 0.15 \mu\text{m}$  and  $r_z = 1.0 \pm 0.1 \mu\text{m}$ ). The low performances of the  $\times 20$  lens can perhaps be explained with an insufficiently expanded beam profile that might fail to evenly fill the objective back aperture. The beam expander should therefore be improved, possibly using lenses with shorter focal lengths to avoid clipping effects without reducing the scanning field of view.

In light of the integration of imaging with electrophysiological recordings, a planar scan protocol was developed and validated. Instead of scanning across the whole extend of the available field of view (FOV) ( $\sim 560 \times 560 \mu\text{m}^2$  for the  $\times 20$  objective), the adopted protocol generates an image by collecting several, adjacent tiles acquired at the centre of the FOV ( $60 \times 60 \mu\text{m}^2$ ). This method was implemented to reduce the effect that large, correlated artefacts induced across the whole MEA on a short time window might have on spike sorting.

## 5.2 Integration of the two-photon microscope with the electrophysiology system

The microscope was integrated with the MEA system to combine recordings with two-photon imaging and two-photon optogenetic stimulation. Recordings were performed on retinas from wild-type or PV-Cre;Ai32 mice. The author mastered retinal dissection procedures, obtained a personal licence for the handling of small animals and performed the electrophysiology experiments.

Optical characterisation of the microscope performance while imaging through the MEA with the  $\times 20$ , 0.5 NA objective revealed an effective NA of  $\sim 0.3$ . This loss in optical resolution might be due to optical aberrations and to an insufficiently expanded excitation beam.

Retinas expressing a genetically targeted fluorescent marker in the RGCs were successfully imaged through the MEA in two-photon regime. This was done using a relatively high average power ( $\sim 100$  mW) and long pixel dwell times (up to 0.5 ms). This can be explained not only with the low effective NA employed, but also with the poor expression of fluorescence in the imaged retinas. Besides exposing the retinal tissue to potentially toxic doses of radiation, high average powers can also damage the MEA's ITO tracks. Previous work reported how ITO thin films deposited on glass can be ablated by ultra-short laser pulses [107]. Opacification of ITO tracks was observed while illuminating with NIR wavelengths (920 nm) above 40 mW. This means that imaging protocols must use lower laser power and shorter pixel dwell times to preserve MEA integrity. Looking back at equation 1.2, it is interesting to note that recovering the full NA of the objective (0.5) will allow to reduce the average excitation power by a factor  $(0.5/0.3)^2 \sim 3$ , without losing on excitation efficiency.

A possible option to improve the generation of fluorescent signals is to use high-NA objectives with a long working distance. However, besides being expensive, these lenses are more prone to suffer from aberrations while working with an extra thickness of glass. An alternative solution would use excitation from the top of the MEA. In this case, water immersion objectives with large NA (e.g. Nikon  $\times 60$ , NA 1) would be the ideal choice. Nonetheless, projecting light from the top of the MEA is challenging as the chamber system that circulates the physiological solution and holds the tissue into place is not designed for the insertion of an objective tip. The retinas employed in the experiments exhibited poor expression of fluorescent markers; a sample with a better expression of fluorescent markers is therefore necessary to perform two-photon imaging at lower powers.

Besides interacting with ITO tracks, the laser beam also generates recording artifacts. These artifacts contaminate the spike clusters used for neuron identification. However, neuron identification in presence of laser scanning was demonstrated. This was achieved with a lower efficiency when compared with artifact free recordings in the same retina. The limited efficiency of neuron identification in artifact affected recording is a central problem to be tackled in the optimisation of the system. A radical approach would blank out the time window surrounding the artifact in the electrode traces. However, this comes at a cost of reduced spike statistics, a parameter that is also crucial for neuron identification. An alternative solution would seek to avoid the electrodes while scanning the beam on the array. This approach, which requires a registration of the electrodes position and a tight control on the laser beam position, might be useful in avoiding the larger artefacts but, perhaps, would not prevent artefact generation on the beam tails.

Two-photon optogenetic stimulation was attempted by scanning over RGCs soma in PV-Cre;Ai32 mouse with spiral scanning patterns, following the approach demonstrated by [38]. Spiral scans

did not prevent neuron identification but resulted in pervasive contamination. No signature of successful optogenetic stimulation was observed. This can possibly be explained by the poor expression of ChR2 in the recorded retinas as testified by low fluorescence. A moderate NA is not expected to be detrimental for two-photon optogenetic stimulation as a larger spot size recruits more ChR2 molecules, provided enough average power is delivered [38]. Future experiments for two-photon optogenetic stimulation in RGCs should employ alternative genetic lines characterised by a stronger expression of opsin proteins. Promising options arise from the recently developed red-shifted opsin proteins optimised for two-photon stimulation [82].

### 5.3 Optogenetic stimulation with the $\mu$ LED system

An optogenetic stimulation system based on a  $\mu$ LED array was integrated with the MEA-two-photon setup. The  $\mu$ LED projection system was also integrated with an existing, high-density 519 MEA in collaboration with Sher Lab at the University of California Santa Cruz. This system was employed in the characterisation of genetically targeted RGC sub-populations in the mouse. This led to the proof of principle of a novel method to match anatomical information to functional and genetic identity in RGCs with a large scale approach.

This method, described in chapter 4, combines visual and optogenetic stimulation to address retinal sections where a fusion protein ChR2-TdTomato was targeted to a molecular subset of RGCs. After obtaining a functional characterisation of RGCs by recording their responses to a spatio-temporal visual stimulus, the unique spiking signatures induced on the MEA were linked to anatomical ChR2-expressing fluorescent cell somas by calculating optogenetically-induced receptive fields. This receptive field yields information not only on the cell body location but also on its genetic identity (as the ChR2 is targeted to molecular sub-types, e.g. Grik4). Considering the many molecular options available for optogenetic gene expression, this method is a versatile tool that can be used to match function to anatomical and genetic classifications.

Genetic lines where ChR2 was sparsely expressed in the RGCs (Grik4-Cre or CRH-ires-Cre) were instrumental. In fact, the current system operates a  $\times 5$  optical de-magnification that produces projected pixels of  $\sim 20 \mu\text{m}$  side. The area covered by these pixels approximately corresponds to the area of an RGC soma: if two cells fall under the same pixel, it is not possible to unambiguously link them to an electrophysiologically identified cell. This drawback prevents the method to be applied in genetic lines with a dense expression of ChR2. This limitation might be circumvented using a smaller pixel size that might also uncover underlying structure in the optogenetically induced receptive fields. Higher resolution in the optogenetic stimulation can be obtained in two ways: using smaller  $\mu$ LED pixels [42] or using an illuminating objective with higher magnification. The latter option, however, implies a reduction in stimulated area and, perhaps, in the collection efficiency.

An alternative approach can be implemented exploiting the existing setup and an x-y stage controller. Optogenetic receptive fields at higher resolution can be generated by combining subsequent stimulation runs where each stimulation area is progressively displaced by a fraction of a pixel. After generating spike triggered averages in different, partially overlapping positions, the resulting averaged frames can be summed in a single grid taking account of the relative displacements. This will produce fine grained optogenetically induced receptive field. This approach does not involve any modification of the existing setup but requires additional experimental time to generate the optogenetically induced receptive field. In fact, a  $\times 2$  reduction in pixel side size will require 4 stimulation runs. Nonetheless, either using smaller  $\mu$ LED or higher de-magnification, longer run time will be required to cover the same area.

Overall, optogenetic stimulation with  $\mu$ LED arrays offers an elegant, inexpensive and miniature solution compared to other methods for visible optogenetic stimulation with patterned single photon illumination. Previous works demonstrated optogenetic stimulation in the retina using digital light projectors (DLP) [127] or computer generated holograms realised with spatial light modulators (SLMs)[37]. These optical techniques are valid options because they allow for a greater control on the illumination patterns. In fact, advanced optical systems that capitalise on these methods have produced remarkable results [128]. However, these optical architectures often require expensive equipment and extensive expertise and this can limit their impact in the neuroscientific community. Conversely,  $\mu$ LED arrays offer a practical solution for research laboratories that do not focus on the development of optical technologies.

## 5.4 Future experiments

The previous sections summarised the achievements and discussed the challenges encountered in this work. This last section, instead, suggests future experiments that might be performed with the described setup.

### Optogenetic stimulation experiments with $\mu$ LED arrays

As earlier discussed, stimulation patterns with higher resolution can be used in experiments involving genetic lines with dense Chr2 expression or to investigate the presence of structure in the optogenetic receptive fields. In this direction, advances in the control of  $\mu$ LED array sources [129] can be exploited to generate rapid sequences of structured stimulating patterns which can lead to efficient and, perhaps, self-learning stimulation protocols which can autonomously identify Chr2 transfected RGCs [130].  $\mu$ LED sources might be used for multi-modal control of neural activity in retinal preparations expressing stimulating and inhibiting opsins [131] by simultaneously projecting spatio-temporal patterns produced with emitters of different colour [132]. Furthermore, it is perhaps possible to conceive an experiment where  $\mu$ LED illumination is exploited to enhance

spike sorting and the spatial resolution of MEAs. RGCs expressing step-function opsins might be manipulated with spatio-temporal illumination patterns to limit the release of action potentials in a spatio-temporally confined volume. For example,  $\mu$ LED can be arranged in patterns resembling the beam profiles used for STED microscopy, where the emission of fluorescence is limited to a spatially confined area.

### **Two-photon imaging and optogenetic stimulation experiments**

The application of two-photon imaging to retinal electrophysiology experiments has allowed the monitoring of neural activity in hard to reach layers containing amacrine and bipolar cells [133] and to integrate these observations with simultaneous MEA recordings of the RGCs activity [134]. Moreover, following the development of red-shifted opsin probes with optimised kinetics [82], two-photon optogenetic stimulation revealed itself a promising technique [46] that recently generated remarkable results, often in combination with two-photon functional imaging [83, 84, 85].

In this direction, an interesting experiment might target the amacrine cells. These cells might be located with two-photon imaging and then optogenetically stimulated while recording RGCs responses to a visual stimulus of photoreceptors. For example, it would be interesting to target starburst amacrine cells, the only cholinergic neurons in the retina [4], which are labelled with a fusion protein eYFP-ChR2 in a commercially available Chat-Cre line [116]. This experiment will allow to gain insight into the role of starburst amacrine cells in the retinal circuitry. A similar approach can be also employed to optogenetically manipulate bipolar cells while recordings from RGCs.

# Acknowledgements and contributions

## Acknowledgements

I acknowledge and thank Dr. Keith Mathieson, who has supervised this work, Dr. Niall McAlinden and Dr. Debbie Gunning.

I also acknowledge and thank fellow PhD students in the Neuro-Photonics group: Dr. Abigail Jeorret, Robert Scharf, Douglas Young, Antoine Boudet, Gabor Varkonyi, Yunzhou Cheng.

With them, I thank all members of the Institute of Photonics and Paul Hynd.

I acknowledge Dr. Erin Zampaglione, Jen Roebber and Prof. Alexander Sher for the experiments conducted at the University of California Santa Cruz.

I thank Dr. Josue Yague, Dr. Daniel Lyngholm and Dr. Shuzo Sakata for their help with the animals used in the electrophysiological experiments.

I acknowledge funding from EPSRC and SUPA, that supported my visit to Santa Cruz.

## Contributions to conferences

“Large-scale matching of anatomy and function in genetically targeted retinal ganglion cells ”

ARVO 2016, Arvo Annual Meeting, Seattle, Washington, US, 1-5 May 2016.

Poster presentation

## Publications

“Large-scale matching of anatomy and function in genetically targeted retinal ganglion cells ”

F.Pisano\*, E.Zampaglione\*, N.McAlinden, J.Roebber, M.D.Dawson & A.Sher<sup>†</sup>& K.Mathieson<sup>†</sup>

Submitted

\*These authors are joint first authors

<sup>†</sup>These authors jointly supervised this work



# Bibliography

- [1] A. Paul Alivisatos, Miyoung Chun, George M. Church, Ralph J. Greenspan, Michael L. Roukes, and Rafael Yuste. The Brain Activity Map Project and the Challenge of Functional Connectomics. *Neuron*, 74(6):970–974, June 2012.
- [2] A. M. Litke, N. Bezayiff, E. J. Chichilnisky, W. Cunningham, W. Dabrowski, A. A. Grillo, M. Grivich, P. Grybos, P. Hottowy, S. Kachiguine, R. S. Kalmar, K. Mathieson, D. Petrusca, M. Rahman, and A. Sher. What does the eye tell the brain?: Development of a system for the large-scale recording of retinal output activity. *IEEE Transactions on Nuclear Science*, 51(4):1434–1440, August 2004.
- [3] Greg D. Field, Jeffrey L. Gauthier, Alexander Sher, Martin Greschner, Timothy Machado, Lauren H. Jepson, Jonathon Shlens, Deborah E. Gunning, Keith Mathieson, Wladyslaw Dabrowski, Liam Paninski, Alan M. Litke, and E.J. Chichilnisky. Functional connectivity in the retina at the resolution of photoreceptors. *Nature*, 467(7316):673–677, October 2010.
- [4] Richard H. Masland. The Neuronal Organization of the Retina. *Neuron*, 76(2):266–280, October 2012.
- [5] A. Paul Alivisatos, Miyoung Chun, George M. Church, Ralph J. Greenspan, Michael L. Roukes, and Rafael Yuste. A National Network of Neurotechnology Centers for the BRAIN Initiative. *Neuron*, 88(3):445–448, November 2015.
- [6] Fritjof Helmchen and Winfried Denk. Deep tissue two-photon microscopy. *Nat. Methods*, 2(12):932–940, December 2005.
- [7] Ofer Yizhar, Lief E. Fenno, Thomas J. Davidson, Murtaza Mogri, and Karl Deisseroth. Optogenetics in neural systems. *Neuron*, 71(1):9–34, July 2011.
- [8] Helga Kolb. How the retina works. *American scientist*, 91(1):28–35, 2003.
- [9] Eric R Kandel, James H Schwartz, and Thomas M Jessell. *Principles of Neural Science*. McGraw-Hill, Health Professions Division, New York, 2000. OCLC: 42073108.

- [10] Robert W Rodieck. *The First Steps in Seeing*, volume 11. Sinauer Associates Sunderland, MA, 1998.
- [11] Simple Anatomy of the Retina by Helga Kolb –Webvision.
- [12] Niklaus Holbro, Åsa Grunditz, and Thomas G. Oertner. Differential distribution of endoplasmic reticulum controls metabotropic signaling and plasticity at hippocampal synapses. *PNAS*, 106(35):15055–15060, January 2009.
- [13] A. L. Hodgkin and A. F. Huxley. A quantitative description of membrane current and its application to conduction and excitation in nerve. *J Physiol*, 117(4):500–544, August 1952.
- [14] W. Cunningham, K. Mathieson, F. A. McEwan, A. Blue, R. McGeachy, J. A. McLeod, C. Morris-Ellis, V. O’Shea, K. M. Smith, A Litke, and M. Rahman. Fabrication of microelectrode arrays for neural measurements from retinal tissue. *J. Phys. D: Appl. Phys.*, 34(18):2804, 2001.
- [15] K Mathieson, W Cunningham, J Marchal, J Melone, M Horn, D Gunning, R Tang, C Wilkinson, V O’Shea, K. M Smith, A Litke, E. J Chichilnisky, and M Rahman. Detection of retinal signals using position sensitive microelectrode arrays. *Nuclear Instruments and Methods in Physics Research Section A: Accelerators, Spectrometers, Detectors and Associated Equipment*, 513(1–2):51–56, November 2003.
- [16] D. E. Gunning, E. J. Chichilnisky, A. M. Litke, V. O’Shea, K. M. Smith, and K. Mathieson. Performance of ultra-high-density microelectrode arrays. *Nuclear Instruments and Methods in Physics Research Section A: Accelerators, Spectrometers, Detectors and Associated Equipment*, 576(1):215–219, June 2007.
- [17] Richard H. Masland. The fundamental plan of the retina. *Nat Neurosci*, 4(9):877–886, September 2001.
- [18] Heinz Wässle, Christian Puller, Frank Müller, and Silke Haverkamp. Cone Contacts, Mosaics, and Territories of Bipolar Cells in the Mouse Retina. *J. Neurosci.*, 29(1):106–117, July 2009.
- [19] Tobias Breuninger, Christian Puller, Silke Haverkamp, and Thomas Euler. Chromatic Bipolar Cell Pathways in the Mouse Retina. *J. Neurosci.*, 31(17):6504–6517, April 2011.
- [20] Béla Völgyi, Samir Chheda, and Stewart A. Bloomfield. Tracer coupling patterns of the ganglion cell subtypes in the mouse retina. *J. Comp. Neurol.*, 512(5):664–687, February 2009.
- [21] Tom Baden, Philipp Berens, Katrin Franke, Miroslav Román Rosón, Matthias Bethge, and Thomas Euler. The functional diversity of retinal ganglion cells in the mouse. *Nature*, 529(7586):345–350, January 2016.

- [22] Wei Wei and Marla B. Feller. Organization and development of direction-selective circuits in the retina. *Trends in Neurosciences*, 34(12):638–645, December 2011.
- [23] Karl Deisseroth. Optogenetics: 10 years of microbial opsins in neuroscience. *Nat Neurosci*, 18(9):1213–1225, September 2015.
- [24] Edward S. Boyden, Feng Zhang, Ernst Bamberg, Georg Nagel, and Karl Deisseroth. Millisecond-timescale, genetically targeted optical control of neural activity. *Nat. Neurosci.*, 8(9):1263–1268, September 2005.
- [25] Dieter Oesterhelt and Walther Stoeckenius. Functions of a New Photoreceptor Membrane. *PNAS*, 70(10):2853–2857, January 1973.
- [26] Akemi Matsuno-Yagi and Yasuo Mukohata. Two possible roles of bacteriorhodopsin; a comparative study of strains of *Halobacterium halobium* differing in pigmentation. *Biochemical and Biophysical Research Communications*, 78(1):237–243, September 1977.
- [27] Lars-Oliver Essen. Halorhodopsin: Light-driven ion pumping made simple? *Current Opinion in Structural Biology*, 12(4):516–522, August 2002.
- [28] Georg Nagel, Doris Ollig, Markus Fuhrmann, Suneel Kateriya, Anna Maria Musti, Ernst Bamberg, and Peter Hegemann. Channelrhodopsin-1: A light-gated proton channel in green algae. *Science*, 296(5577):2395–2398, June 2002.
- [29] Georg Nagel, Tanjef Szellas, Wolfram Huhn, Suneel Kateriya, Nona Adeishvili, Peter Berthold, Doris Ollig, Peter Hegemann, and Ernst Bamberg. Channelrhodopsin-2, a directly light-gated cation-selective membrane channel. *PNAS*, 100(24):13940–13945, November 2003.
- [30] Katrin Feldbauer, Dirk Zimmermann, Verena Pintschovius, Julia Spitz, Christian Bamann, and Ernst Bamberg. Channelrhodopsin-2 is a leaky proton pump. *Proceedings of the National Academy of Sciences*, 106(30):12317–12322, 2009.
- [31] Feng Zhang, Li-Ping Wang, Edward S. Boyden, and Karl Deisseroth. Channelrhodopsin-2 and optical control of excitable cells. *Nat Meth*, 3(10):785–792, October 2006.
- [32] Georg Nagel, Martin Brauner, Jana F. Liewald, Nona Adeishvili, Ernst Bamberg, and Alexander Gottschalk. Light Activation of Channelrhodopsin-2 in Excitable Cells of *Caenorhabditis elegans* Triggers Rapid Behavioral Responses. *Current Biology*, 15(24):2279–2284, December 2005.
- [33] Xue Han, Xiaofeng Qian, Patrick Stern, Amy Chuong, Edward S. Boyden, Xue Han, Xiaofeng Qian, Patrick Stern, Amy S. Chuong, and Edward S. Boyden. Informational lesions: Optical perturbation of spike timing and neural synchrony via microbial opsin gene fusions. *Front. Mol. Neurosci.*, 2:12, 2009.

- [34] Adam M. Packer, Botond Roska, and Michael Häusser. Targeting neurons and photons for optogenetics. *Nat Neurosci*, 16(7):805–815, July 2013.
- [35] Benjamin R. Arenkiel, Joao Peca, Ian G. Davison, Catia Feliciano, Karl Deisseroth, George J. Augustine, Michael D. Ehlers, and Guoping Feng. In Vivo Light-Induced Activation of Neural Circuitry in Transgenic Mice Expressing Channelrhodopsin-2. *Neuron*, 54(2):205–218, April 2007.
- [36] Huntington Potter and Huntington Potter. Transfection by Electroporation, Transfection by Electroporation. In *Current Protocols in Molecular Biology, Current Protocols in Molecular Biology*, pages 9.3.1–9.3.6. John Wiley & Sons, Inc., John Wiley & Sons, Inc., May 2003.
- [37] Inna Reutsky-Gefen, Lior Golan, Nairouz Farah, Adi Schejter, Limor Tsur, Inbar Brosh, and Shy Shoham. Holographic optogenetic stimulation of patterned neuronal activity for vision restoration. *Nat Commun*, 4:1509, February 2013.
- [38] John Peter Rickgauer and David W. Tank. Two-photon excitation of channelrhodopsin-2 at saturation. *PNAS*, 106(35):15025–15030, January 2009.
- [39] Valentina Emiliani, Adam E. Cohen, Karl Deisseroth, and Michael Häusser. All-Optical Interrogation of Neural Circuits. *J. Neurosci.*, 35(41):13917–13926, October 2015.
- [40] Viviana Gradinaru, Kimberly R. Thompson, Feng Zhang, Murat Mogri, Kenneth Kay, M. Bret Schneider, and Karl Deisseroth. Targeting and Readout Strategies for Fast Optical Neural Control In Vitro and In Vivo. *J. Neurosci.*, 27(52):14231–14238, December 2007.
- [41] Niall McAlinden, Erdan Gu, Martin D. Dawson, Shuzo Sakata, and Keith Mathieson. Optogenetic activation of neocortical neurons in vivo with a sapphire-based micro-scale LED probe. *in vivo*, page 25, 2015.
- [42] Nir Grossman, Vincent Poher, Matthew S. Grubb, Gordon T. Kennedy, Konstantin Nikolic, Brian McGovern, Rolando Berlinguer Palmieri, Zheng Gong, Emmanuel M. Drakakis, Mark A. A. Neil, Martin D. Dawson, Juan Burrone, and Patrick Degenaar. Multi-site optical excitation using ChR2 and micro-LED array. *J. Neural Eng.*, 7(1):016004, 2010.
- [43] Jonathan J. D. McKendry, David Massoubre, Shuailong Zhang, Bruce R. Rae, Richard P. Green, Erdan Gu, Robert K. Henderson, A. E. Kelly, and Martin D. Dawson. Visible-Light Communications Using a CMOS-Controlled Micro-Light-Emitting-Diode Array. *J. Lightwave Technol., JLT*, 30(1):61–67, January 2012.
- [44] W. Denk, J. H. Strickler, and W. W. Webb. Two-photon laser scanning fluorescence microscopy. *Science*, 248(4951):73–76, April 1990.

- [45] Erich E. Hoover and Jeff A. Squier. Advances in multiphoton microscopy technology. *Nat Photon*, 7(2):93–101, February 2013.
- [46] Dan Oron, Eirini Papagiakoumou, F. Anselmi, and Valentina Emiliani. Chapter 7 - Two-photon optogenetics. In Thomas Knöpfel Boyden and Edward S., editors, *Progress in Brain Research*, volume 196 of *Optogenetics: Tools for Controlling and Monitoring Neuronal Activity*, pages 119–143. Elsevier, 2012.
- [47] Osamu Nakamura. Fundamental of two-photon microscopy. *Microsc. Res. Tech.*, 47(3):165–171, November 1999.
- [48] Maria Göppert-Mayer. Über Elementarakte mit zwei Quantensprüngen. *Ann. Phys.*, 401(3):273–294, January 1931.
- [49] Peter TC So. Two-photon Fluorescence Light Microscopy. In *eLS*. John Wiley & Sons, Ltd, 2001.
- [50] Fritjof Helmchen and Winfried Denk. Deep tissue two-photon microscopy. *Nat Meth*, 2(12):932–940, December 2005.
- [51] Watt W. Webb Chris Xu. Xu, C. ; Webb, W. W. Measurement of two-photon excitation cross sections of molecular fluorophores with data from 690 to 1050 nm. *J. Opt. Soc. Am. B* 13, 481-491. *J. Opt. Soc. Am. B*, 13(3):481–491, 1996.
- [52] W. Kaiser and C. G. B. Garrett. Two-Photon Excitation in  $\text{CaF}_2: \text{Eu}^{2+}$ . *Phys. Rev. Lett.*, 7(6):229–231, September 1961.
- [53] E. Spiess, F. Bestvater, A. Heckel-Pompey, K. Toth, M. Hacker, G. Stobrawa, T. Feurer, C. Wotzlaw, U. Berchner-Pfannschmidt, T. Porwol, and H. Acker. Two-photon excitation and emission spectra of the green fluorescent protein variants ECFP, EGFP and EYFP. *Journal of Microscopy*, 217(3):200–204, March 2005.
- [54] Robert R. Birge. Two-photon spectroscopy of protein-bound chromophores. *Acc. Chem. Res.*, 19(5):138–146, May 1986.
- [55] Winfried Denk, David W. Piston, and Watt W. Webb. Two-Photon Molecular Excitation in Laser-Scanning Microscopy. In James B. Pawley, editor, *Handbook of Biological Confocal Microscopy*, pages 445–458. Springer US, 1995.
- [56] Winfried Denk and Karel Svoboda. Photon Upmanship: Why Multiphoton Imaging Is More than a Gimmick. *Neuron*, 18(3):351–357, March 1997.
- [57] Demirhan Kobat, Michael E. Durst, Nozomi Nishimura, Angela W. Wong, Chris B. Schaffer, and Chris Xu. Deep tissue multiphoton microscopy using longer wavelength excitation. *Optics Express*, 17(16):13354, August 2009.

- [58] A N Yaroslavsky, P C Schulze, I V Yaroslavsky, R Schober, F Ulrich, and H-J Schwarzmaier. Optical properties of selected native and coagulated human brain tissues in vitro in the visible and near infrared spectral range. *Physics in Medicine and Biology*, 47(12):2059–2073, June 2002.
- [59] K. König. Multiphoton microscopy in life sciences. *Journal of Microscopy*, 200(2):83–104, November 2000.
- [60] J. M. Girkin. Optical physics enables advances in multiphoton imaging. *J. Phys. D: Appl. Phys.*, 36(14):R250, 2003.
- [61] C. J. R. Sheppard Alberto Diaspro. Two-Photon Excitation Fluorescence Microscopy. pages 39–73, 2002.
- [62] John Girkin. Practical multiphoton microscopy. In *In Confocal and Two-Photon Microscopy : Foundations, Applications and Advances*, pages 207–236. Wiley-Liss, Inc, 2001.
- [63] Fritjof Helmchen and Winfried Denk. Deep tissue two-photon microscopy. *Nat Meth*, 2(12):932–940, December 2005.
- [64] Karel Svoboda and Ryohei Yasuda. Principles of Two-Photon Excitation Microscopy and Its Applications to Neuroscience. *Neuron*, 50(6):823–839, June 2006.
- [65] Peter T. C. So, Ki H. Kim, Christof Buehler, Barry R. Masters, Lily Hsu, and Chen-Yuan Dong. Basic Principles of Multiphoton Excitation Microscopy. In Ammasi Periasamy, editor, *Methods in Cellular Imaging*, Methods in Physiology, pages 147–161. Springer New York, 2001.
- [66] Jeffrey B. Guild, Chris Xu, and Watt W. Webb. Measurement of group delay dispersion of high numerical aperture objective lenses using two-photon excited fluorescence. *Appl. Opt.*, *AO*, 36(1):397–401, January 1997.
- [67] R. L. Fork, O. E. Martinez, and J. P. Gordon. Negative dispersion using pairs of prisms. *Opt. Lett.*, *OL*, 9(5):150–152, May 1984.
- [68] Michael D. Young, Jeffrey J. Field, Kraig E. Sheetz, Randy A. Bartels, and Jeff Squier. A pragmatic guide to multiphoton microscope design. *Adv. Opt. Photon.*, *AOP*, 7(2):276–378, June 2015.
- [69] Aurélie Facomprez, Emmanuel Beaupaire, and Delphine Débarre. Accuracy of correction in modal sensorless adaptive optics. *Opt. Express*, *OE*, 20(3):2598–2612, January 2012.
- [70] G. Y. Fan, H. Fujisaki, A. Miyawaki, R. K. Tsay, Roger Y. Tsien, and Mark H. Ellisman. Video-Rate Scanning Two-Photon Excitation Fluorescence Microscopy and Ratio Imaging with Cameleons. *Biophysical Journal*, 76(5):2412–2420, May 1999.

- [71] Jörg Bewersdorf, Alexander Egner, and Stefan W. Hell. Multifocal Multi-Photon Microscopy. In James B. Pawley, editor, *Handbook Of Biological Confocal Microscopy*, pages 550–560. Springer US, 2006.
- [72] Yonghong Shao, Wan Qin, Honghai Liu, Junle Qu, Xiang Peng, Hanben Niu, and Bruce Z. Gao. Ultrafast, large-field multiphoton microscopy based on an acousto-optic deflector and a spatial light modulator. *Opt. Lett.*, *OL*, 37(13):2532–2534, July 2012.
- [73] James E Jonkman and Ernst HK Stelzer. Resolution and contrast in confocal and two-photon microscopy. In *Confocal and Two-Photon Microscopy: Foundations, Applications, and Advances*, pages 101–125. Wiley-Liss, New York, 2002.
- [74] Laurent Porres, Olivier Mongin, Claudine Katan, Marina Charlot, Thomas Pons, Jerome Mertz, and Mireille Blanchard-Desce. Enhanced Two-Photon Absorption with Novel Octupolar Propeller-Shaped Fluorophores Derived from Triphenylamine. *Org. Lett.*, 6(1):47–50, January 2004.
- [75] Zhixing Chen, Lu Wei, Xinxin Zhu, and Wei Min. Extending the fundamental imaging-depth limit of multi-photon microscopy by imaging with photo-activatable fluorophores. *Optics Express*, 20(17):18525, August 2012.
- [76] Patrick Theer and Winfried Denk. On the fundamental imaging-depth limit in two-photon microscopy. *J. Opt. Soc. Am. A*, *JOSAA*, 23(12):3139–3149, December 2006.
- [77] Demirhan Kobat, Nicholas G. Horton, and Chris Xu. In vivo two-photon microscopy to 1.6-mm depth in mouse cortex. *J. Biomed. Opt.*, 16(10):106014–106014–4, 2011.
- [78] Nicholas G. Horton, Ke Wang, Demirhan Kobat, Catharine G. Clark, Frank W. Wise, Chris B. Schaffer, and Chris Xu. In vivo three-photon microscopy of subcortical structures within an intact mouse brain. *Nat Photon*, 7(3):205–209, March 2013.
- [79] Karl Svoboda and Ryohei Yasuda. Principles of two-photon excitation microscopy and its applications to neuroscience. *Neuron*, 50(6):823–839, 2006.
- [80] Bertalan K. Andrasfalvy, Boris V. Zemelman, Jianyong Tang, and Alipasha Vaziri. Two-photon single-cell optogenetic control of neuronal activity by sculpted light. *Proc Natl Acad Sci U S A*, 107(26):11981–11986, June 2010.
- [81] Eirini Papagiakoumou, Francesca Anselmi, Aurélien Bègue, Vincent de Sars, Jesper Glückstad, Ehud Y. Isacoff, and Valentina Emiliani. Scanless two-photon excitation of channelrhodopsin-2. *Nat Meth*, 7(10):848–854, October 2010.
- [82] Roit Prakash. Two-photon optogenetic toolbox for fast inhibition, excitation and bistable modulation. *Nature methods*, 9(12):1171–1179, 2012.

- [83] Adam M. Packer, Darcy S. Peterka, Jan J. Hirtz, Rohit Prakash, Karl Deisseroth, and Rafael Yuste. Two-photon optogenetics of dendritic spines and neural circuits. *Nat Meth*, 9(12):1202–1205, December 2012.
- [84] Adam M. Packer, Lloyd E. Russell, Henry W. P. Dagleish, and Michael Häusser. Simultaneous all-optical manipulation and recording of neural circuit activity with cellular resolution in vivo. *Nat Meth*, 12(2):140–146, February 2015.
- [85] John Peter Rickgauer, Karl Deisseroth, and David W. Tank. Simultaneous cellular-resolution optical perturbation and imaging of place cell firing fields. *Nat Neurosci*, 17(12):1816–1824, December 2014.
- [86] Niall McAlinden and Filippo Pisano. Custom control of LED.
- [87] Alberto Diaspro and C. J. R. Sheppard. *Two-Photon Excitation Fluorescence Microscopy*. January 2002.
- [88] Spectra Physics. *MAI-TAI HP Users's Manual*. 2006.
- [89] Marcos A. de Araújo, Rubens Silva, Emerson de Lima, Daniel P. Pereira, and Paulo C. de Oliveira. Measurement of Gaussian laser beam radius using the knife-edge technique: Improvement on data analysis. *Applied Optics*, 48(2):393, January 2009.
- [90] Cambridge Technology. *PositioPro2 Hardware Manual*. 2007.
- [91] Michael D. Young, Jeffrey J. Field, Kraig E. Sheetz, Randy A. Bartels, and Jeff Squier. A pragmatic guide to multiphoton microscope design. *Adv. Opt. Photon., AOP*, 7(2):276–378, June 2015.
- [92] Stephan Preibisch, Stephan Saalfeld, and Pavel Tomancak. Globally optimal stitching of tiled 3D microscopic image acquisitions. *Bioinformatics*, 25(11):1463–1465, June 2009.
- [93] Quoc-Thang Nguyen, Philbert S. Tsai, and David Kleinfeld. MPScope: A versatile software suite for multiphoton microscopy. *Journal of Neuroscience Methods*, 156(1-2):351–359, September 2006.
- [94] Thomas A. Polgruto, Bernardo L. Sabatini, and Karel Svoboda. ScanImage: Flexible software for operating laser scanning microscopes. *BioMedical Engineering OnLine*, 2(1):1, May 2003.
- [95] Stephan Preibisch, Stephan Saalfeld, and Pavel Tomancak. Globally Optimal Stitching of Tiled 3D Microscopic Image Acquisitions. *Bioinformatics*, 25(11):1463–5, May 2009.
- [96] Kurt Thorn. Shading correction of fluorescence images | Kurt's Microscopy Blog.

- [97] D E Gunning, J M Beggs, W Dabrowski, P Hottowy, C J Kenney, A Sher, A M Litke, and K Mathieson. Dense arrays of micro-needles for recording and electrical stimulation of neural activity in acute brain slices. *Journal of Neural Engineering*, 10(1):016007, February 2013.
- [98] Alberto Diaspro. Building a Two-Photon Microscope Using a Laser Scanning Confocal Architecture. In Ammasi Periasamy, editor, *Methods in Cellular Imaging*, Methods in Physiology, pages 162–179. Springer New York, 2001.
- [99] Ludovico Silvestri, Anna Letizia Allegra Mascaro, Irene Costantini, Leonardo Sacconi, and Francesco Saverio Pavone. Correlative two-photon and light sheet microscopy. *Methods*, 66(2):268–272, March 2014.
- [100] R. A Synowicki. Spectroscopic ellipsometry characterization of indium tin oxide film microstructure and optical constants. 313–314:394–397.
- [101] Tobias A. F. König, Petr A. Ledin, Justin Kerszulis, Mahmoud. A. Mahmoud, Mostafa A. El-Sayed, John R. Reynolds, and Vladimir V. Tsukruk. Electrically Tunable Plasmonic Behavior of Nanocube–Polymer Nanomaterials Induced by a Redox-Active Electrochromic Polymer. *ACS Nano*, 8(6):6182–6192, June 2014.
- [102] Herbert R. Philipp. Optical Properties of Silicon Nitride. *J. Electrochem. Soc.*, 120(2):295–300, January 1973.
- [103] Mikhail Polyanski. Refractiveindex.info website. *RefractiveIndex.INFO*, 2016.
- [104] Shubham Duttgupta, Fajun Ma, Bram Hoex, Thomas Mueller, and Armin G. Aberle. Optimised Antireflection Coatings using Silicon Nitride on Textured Silicon Surfaces based on Measurements and Multidimensional Modelling. 15:78–83.
- [105] Min Gu and C. J. R. Sheppard. Comparison of three-dimensional imaging properties between two-photon and single-photon fluorescence microscopy. *Journal of Microscopy*, 177(2):128–137, February 1995.
- [106] Martin J. Booth and Tony Wilson. Refractive-index-mismatch induced aberrations in single-photon and two-photon microscopy and the use of aberration correction. *Journal of biomedical optics*, 6(3):266–272, 2001.
- [107] Mira Park, Byong Hyok Chon, Hyun Sun Kim, Sae Chae Jeoung, Dongho Kim, Jeoung-Ik Lee, Hye Yong Chu, and Hyeong Rae Kim. Ultrafast laser ablation of indium tin oxide thin films for organic light-emitting diode application. *Optics and Lasers in Engineering*, 44(2):138–146, February 2006.

- [108] David Ashkenasi, Arkadi Rosenfeld, Razvan Stoian, Nadezhda M. Bulgakova, Eleanor E. B. Campbell, and Ingolf V. Hertel. Fundamentals and advantages in ultrafast microstructuring of transparent materials. volume 4760, pages 56–62, 2002.
- [109] Zachary C. Holman, Miha Filipič, Antoine Descoeurdes, Stefaan De Wolf, Franc Smole, Marko Topič, and Christophe Ballif. Infrared light management in high-efficiency silicon heterojunction and rear-passivated solar cells. *Journal of Applied Physics*, 113(1):013107, January 2013.
- [110] Michael S Lewicki. A review of methods for spike sorting: The detection and classification of neural action potentials. *Network: Computation in Neural Systems*, 9(4):R53–R78, January 1998.
- [111] Adam H. Marblestone, Bradley M. Zamft, Yael G. Maguire, Mikhail G. Shapiro, Thaddeus R. Cybulski, Joshua I. Glaser, Dario Amodei, P. Benjamin Stranges, Reza Kalhor, David A. Dalrymple, Dongjin Seo, Elad Alon, Michel M. Maharbiz, Jose M. Carmena, Jan M. Rabaey, Edward S. Boyden, George M. Church, and Konrad P. Kording. Physical Principles for Scalable Neural Recording. June 2013.
- [112] Eun-Shil Lee, Tae-Jin Kim, and Chang-Jin Jeon. Identification of parvalbumin-containing retinal ganglion cells in rabbit. *Experimental Eye Research*, 110:113–124, May 2013.
- [113] Tae-Jin Kim and Chang-Jin Jeon. Morphological Classification of Parvalbumin-Containing Retinal Ganglion Cells in Mouse: Single-Cell Injection after Immunocytochemistry. *Invest. Ophthalmol. Vis. Sci.*, 47(7):2757–2764, July 2006.
- [114] Robert Gábel, Ferenc Erdélyi, Gábor Szabó, J. Josh Lawrence, and Márta Wilhelm. Ectopic transgene expression in the retina of four transgenic mouse lines. *Brain Struct Funct*, pages 1–13, November 2015.
- [115] Coverslip Correction-Nikon MicroscopyU website.
- [116] E. Ivanova, G.-S. Hwang, and Z.-H. Pan. Characterization of transgenic mouse lines expressing Cre recombinase in the retina. *Neuroscience*, 165(1):233–243, January 2010.
- [117] Tiffany M Schmidt and Paulo Kofuji. An Isolated Retinal Preparation to Record Light Response from Genetically Labeled Retinal Ganglion Cells. *J Vis Exp*, (47), January 2011.
- [118] Peter H. Li, Jeffrey L. Gauthier, Max Schiff, Alexander Sher, Daniel Ahn, Greg D. Field, Martin Greschner, Edward M. Callaway, Alan M. Litke, and E. J. Chichilnisky. Anatomical Identification of Extracellularly Recorded Cells in Large-Scale Multielectrode Recordings. *J. Neurosci.*, 35(11):4663–4675, March 2015.

- [119] Bushra Y. Ahmed, Sridhara Chakravarthy, Ruben Eggers, Wim TJMC Hermens, Jing Ying Zhang, Simone P. Niclou, Christiaan Levelt, Fred Sablitzky, Patrick N. Anderson, A. R. Lieberman, and Joost Verhaagen. Efficient delivery of Cre-recombinase to neurons in vivo and stable transduction of neurons using adeno-associated and lentiviral vectors. *BMC Neuroscience*, 5(1):1, January 2004.
- [120] Bruce R. Rae Jonathan J. D. McKendry. Individually addressable AlInGaN micro-LED arrays with CMOS control and subnanosecond output pulses. *Photonics Technology Letters, IEEE*, 21(12):811 – 813, 2009.
- [121] E. J. Chichilnisky. Chichilnisky, E. J. A simple white noise analysis of neuronal light responses. Network 12, 199-213. *Network Computation in Neural Systems*, 12(2):199–213, June 2001.
- [122] Justin Elstrott, Anastasia Anishchenko, Martin Greschner, Alexander Sher, Alan M. Litke, E.J. Chichilnisky, and Marla B. Feller. Direction Selectivity in the Retina Is Established Independent of Visual Experience and Cholinergic Retinal Waves. *Neuron*, 58(4):499–506, May 2008.
- [123] Linda Madisen, Tianyi Mao, Henner Koch, Jia-min Zhuo, Antal Berenyi, Shigeyoshi Fujisawa, Yun-Wei A Hsu, Alfredo J Garcia, Xuan Gu, Sebastien Zanella, Jolene Kidney, Hong Gu, Yimei Mao, Bryan M Hooks, Edward S Boyden, György Buzsáki, Jan Marino Ramirez, Allan R Jones, Karel Svoboda, Xue Han, Eric E Turner, and Hongkui Zeng. A toolbox of Cre-dependent optogenetic transgenic mice for light-induced activation and silencing. *Nature Neuroscience*, 15(5):793–802, March 2012.
- [124] Xiang Li, Davina V. Gutierrez, M. Gartz Hanson, Jing Han, Melanie D. Mark, Hillel Chiel, Peter Hegemann, Lynn T. Landmesser, and Stefan Herlitze. Fast noninvasive activation and inhibition of neural and network activity by vertebrate rhodopsin and green algae channelrhodopsin. *PNAS*, 102(49):17816–17821, June 2005.
- [125] Yongling Zhu, Jian Xu, William W. Hauswirth, and Steven H. DeVries. Genetically Targeted Binary Labeling of Retinal Neurons. *J. Neurosci.*, 34(23):7845–7861, April 2014.
- [126] H. X. Zhang, D. Massoubre, J. McKendry, Z. Gong, B. Guilhabert, C. Griffin, E. Gu, P. E. Jessop, J. M. Girkin, and M. D. Dawson. Individually-addressable flip-chip AlInGaN micropixelated light emitting diode arrays with high continuous and nanosecond output power. *Opt. Express, OE*, 16(13):9918–9926, June 2008.
- [127] Kenneth P. Greenberg, Aaron Pham, and Frank S. Werblin. Differential Targeting of Optical Neuromodulators to Ganglion Cell Soma and Dendrites Allows Dynamic Control of Center-Surround Antagonism. 69(4):713–720.

- [128] Alipasha Vaziri and Valentina Emiliani. Reshaping the optical dimension in optogenetics. 22(1):128–137.
- [129] Johannes Herrnsdorf, Jonathan McKendry, Enyuan Xie, Michael Strain, Ian Watson, Erdan Gu, and Martin Dawson. High speed spatial encoding enabled by CMOS-controlled micro-LED arrays. July 2016.
- [130] Johannes Herrnsdorf, Michael Strain, and Martin Dawson. Control of automated systems with a structured light illumination source. August 2016.
- [131] Feng Zhang, Li-Ping Wang, Martin Brauner, Jana F. Liewald, Kenneth Kay, Natalie Watzke, Phillip G. Wood, Ernst Bamberg, Georg Nagel, Alexander Gottschalk, and Karl Deisseroth. Multimodal fast optical interrogation of neural circuitry. *Nature*, 446(7136):633–639, April 2007.
- [132] Shuailong Zhang, Zheng Gong, Jonathan J. D. McKendry, Scott Watson, Andrew Cogman, Enyuan Xie, Pengfei Tian, Erdan Gu, Zhizhong Chen, Guoyi Zhang, Anthony E. Kelly, Robert K. Henderson, and Martin D. Dawson. CMOS-Controlled Color-Tunable Smart Display. *IEEE Photonics Journal*, 4(5):1639–1646, October 2012.
- [133] Thomas A Münch, Rava Azeredo da Silveira, Sandra Siegert, Tim James Viney, Gautam B Awatramani, and Botond Roska. Approach sensitivity in the retina processed by a multi-functional neural circuit. *Nature Neuroscience*, 12(10):1308–1316, October 2009.
- [134] Baccus Stephen. Simultaneous multielectrode recording and multi-photon imaging of retinal visual responses. *Frontiers in Systems Neuroscience*, 3, 2009.

## Appendix A

# Plug system for MEA retinal recordings

Micro Electrode Array recordings of retinal sections were performed using transparent arrays fabricated in ITO as described in chapter 1, 3 and 4. This appendix describes the plug system that was employed to position and maintain the retina in contact with the electrodes.

During the recordings, the retina was immersed in a bath of constantly renovated physiological solution (Ames' medium), oxygenated with a mixture of 95 % O<sub>2</sub> and 5 % CO<sub>2</sub>. This solution was circulated at a tightly controlled temperature (37 °C). This was accomplished with a perfusion system that circulated the solution by means of two metal pipes. The perfusion was contained in a plastic chamber glued on the top surface of the array. As shown in figure A.1, the supply and drain pipes were mounted on an external clamp system that secured the array to the read out electronics.

The plastic chamber was fitted with a platinum ground wire, wrapped around the chamber circumference.

Retinal sections were placed flat on the electrodes with the retinal ganglion cells side down. Retinas were kept in contact with the electrodes with a plug that was inserted in the chamber. The plug prevented the retina from floating away from the electrodes. Once pressed in the chamber, the plug was locked in position by a resistance ring fitted around its diameter. The plug allowed for the flow of solution by means of a dialysis membrane. Figure A.2 shows a diagram of the plug system.

Inserting the plug and pressing it at the appropriate position was a delicate task. In fact, underpressing the plug would fail to keep the retina in contact with the electrodes. Conversely, overpressing the plug would likely result in retinal damage. An excellent method for monitoring this difficult task was provided by imaging the retina on the array with OCT in real-time. Figure A.3 shows an example of an OCT image of the retina mounted on the MEA.

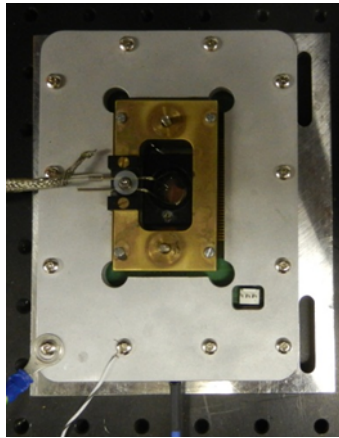


Figure A.1: The electrophysiology system as seen from above. The read out electronics is shielded in an aluminium box. The MEA is clamped to the shielding box to secure the connection between the array bond-pads and the read-out PCB. The clamp also served as a support for the perfusion pipes that continuously renovated the physiological solution. In the figure, the plug is not inserted in the plastic chamber.

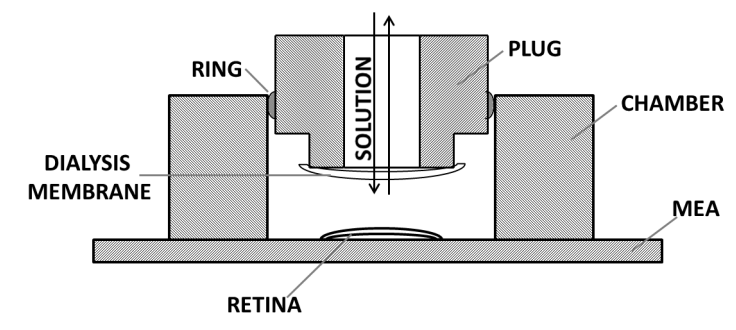


Figure A.2: The figure shows the cross section of the MEA system. The retina is placed flat on the MEA. The plug is inserted in the chamber. The diagram shows the plug inserted in the chamber before being pressed on the retina. The solution is perfused and renovated through the dialysis membrane.

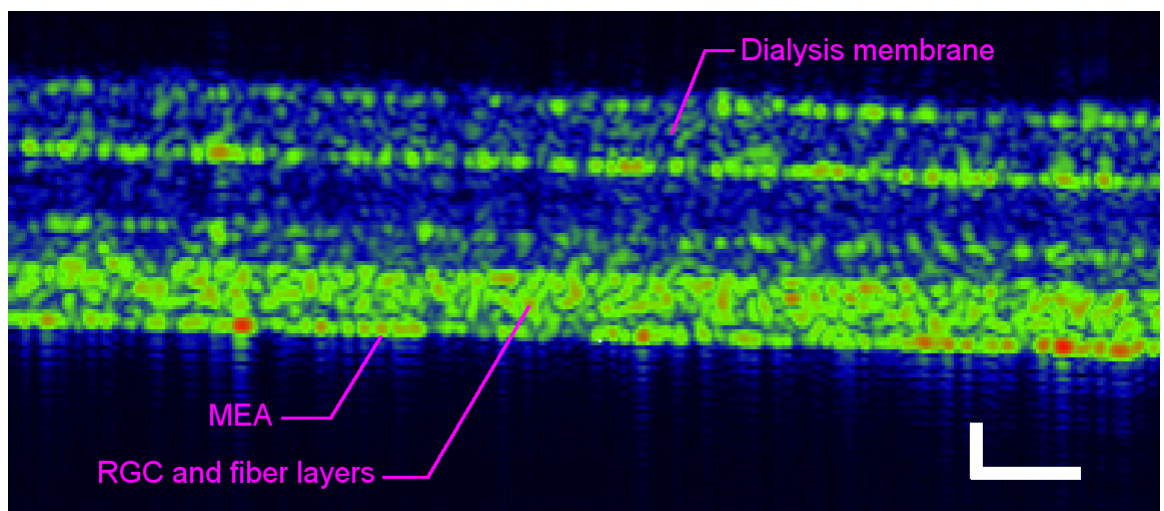


Figure A.3: OCT image of a portion of retina mounted on the MEA. Scale bar is 50  $\mu\text{m}$ . Colour represents the optical density the scanning beam encounters on a pixel. Colour is linked to the scattering intensity on a logarithmic scale. Image courtesy of Dr. N.McAlinden.

